RUPRECHT-KARLS-UNIVERSITÄT HEIDELBERG



Anke Ackermann

Collisions to Conclusions — A Triple-Gauge-Boson Journey

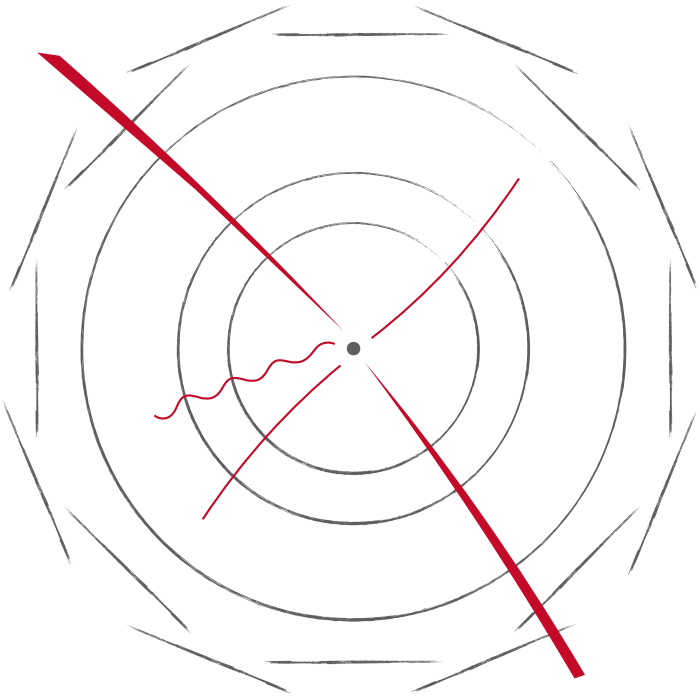
Dissertation

HD-KIP-26-36

KIRCHHOFF-INSTITUT FÜR PHYSIK

Collisions to Conclusions — A Triple-Gauge-Boson Journey

Anke Ackermann



Dissertation

submitted to the

Combined Faculty of Mathematics, Engineering and Natural Sciences

of Heidelberg University, Germany

for the degree of

Doctor of Natural Sciences

Put forward by

Anke Ackermann

born in Trier, Germany

Oral examination: May 13, 2026

Collisions to Conclusions —
A Triple-Gauge-Boson Journey

Referees: Prof. Dr. Hans-Christian Schultz-Coulon
Prof. Dr. Ulrich Uwer

Abstract

The Standard Model of particle physics predicts triple-gauge boson production that test the non-abelian electroweak gauge structure. This thesis reports the first measurement of $ZZ\gamma$ production with the ATLAS detector at the Large Hadron Collider. The analysis uses the full Run 2 dataset (2015–2018), corresponding to an integrated luminosity of 140 fb^{-1} of proton-proton collisions at $\sqrt{s} = 13$ TeV. The study targets the fully leptonic final state, $pp \to ZZ\gamma \to \ell^+\ell^-\ell'^+\ell'^-\gamma$ with $\ell, \ell' = e$ or μ. A fiducial region is defined to suppress contributions from photon final-state radiation and maximize the signal-to-background ratio. The dominant background—non-prompt photons from jets—is estimated with a novel jet-ratio method that extrapolates from a high-statistics control region, achieving a relative systematic uncertainty of 18% on this background. Eight candidate events are observed with an expected background of 0.92 ± 0.15 events, corresponding to a significance of 4.4σ. The fiducial cross-section is measured as $\sigma^{\text{fid}}_{ZZ\gamma} = 0.144^{+0.077}_{-0.053}$ (stat.) ± 0.005 (syst.) fb, in agreement with the Standard Model prediction of 0.143 ± 0.005 fb. This measurement validates the Standard Model description of electroweak triple-gauge boson production within its uncertainties and provides a benchmark for future studies of anomalous quartic-gauge couplings with larger datasets.

Zusammenfassung

Das Standardmodell der Teilchenphysik sagt Triple-Eichboson-Prozesse voraus, die die nicht-abelsche elektroschwache Eichstruktur direkt testen. In dieser Arbeit wird die erste Messung der $ZZ\gamma$ Produktion mit dem ATLAS-Detektor am Large Hadron Collider vorgestellt. Die Analyse nutzt den kompletten Run 2 Datensatz (2015–2018), der einer integrierten Luminosität von $140\,\text{fb}^{-1}$ an Proton-Proton-Kollisionen bei $\sqrt{s} = 13$ TeV entspricht. Untersucht wird der vollständig leptonische Endzustand, $pp \to ZZ\gamma \to \ell^+\ell^-\ell'^+\ell'^-\gamma$ mit $\ell, \ell' = e$ oder μ. Eine Signalregion wird definiert, um den Beitrag von Ereignissen mit Bremsstrahlung zu minimieren und das Signal-zu-Untergrund-Verhältnis zu maximieren. Der dominante Untergrund—nicht-prompte Photonen aus Jets—wird mit einer neu entwickelten Jet-Verhältnis-Methode bestimmt, die aus einer Kontrollregion mit hoher Statistik extrapoliert; damit wird eine relative systematische Unsicherheit von 18% auf diesen Untergrund erreicht. Insgesamt werden acht Ereignisse gemessen bei einem erwarteten Untergrund von 0.92 ± 0.15 Ereignissen, was einer Signifikanz von 4.4σ entspricht. Der gemessene Wirkungsquerschnitt beträgt $\sigma^{\text{fid.}}_{ZZ\gamma} = 0.144^{+0.077}_{-0.053}$ (stat.) $\pm$ 0.005 (syst.) fb und stimmt mit der Vorhersage des Standardmodells von 0.143 ± 0.005 fb überein. Damit bestätigt die Messung im Rahmen ihrer Unsicherheit die Beschreibung der elektroschwachen Triple-Eichboson-Produktion im Standardmodell und liefert einen Referenzwert für zukünftige Studien anomaler quartischer Eichkopplungen mit größeren Datensätzen.

Contents

1 Introduction **1**

2 Theoretical background **5**
2.1 The Standard Model of particle physics 5
2.2 Triple-gauge-boson production 12

3 Experimental setup **15**
3.1 The Large Hadron Collider 15
3.2 The ATLAS detector 18
3.3 Particle reconstruction 22
3.4 Simulation of proton-proton collisions 27

4 The $ZZ\gamma$ analysis **31**
4.1 Analysis strategy 31
4.2 Event selection 34
4.3 Signal expectation 45

5 Background estimation **55**
5.1 Non-prompt photons 55
5.2 Misidentified leptons 71
5.3 Pileup 83
5.4 Summary 88

6 Results **91**
6.1 Signal extraction 91
6.2 Results 92
6.3 Interpretation and discussion 94

7 Conclusion **97**

References **99**

A Technical details **117**
A.1 Trigger selection 117
A.2 Identification and isolation working points 118
A.3 Monte Carlo simulation samples 122
A.4 Baseline and control region selection criteria 124

B Event selection studies **133**
B.1 Signal significance optimization 133
B.2 Kinematic distributions 136

C Non-prompt photons **139**
C.1 Comparison of the non-prompt photon estimates 139
C.2 Jet ratio uncertainties 142

D Misidentified leptons **145**
D.1 Derivation of the misidentified lepton estimate for a four-lepton final state 145

Acronyms

ALFA	Absolute Luminosity for ATLAS
ALICE	A Large Ion Collider Experiment
CERN	European Organization for Nuclear Research
CKM	Cabibbo-Kobayashi-Maskawa
CMS	Compact Muon Solenoid
COM	center-of-mass
CR	control region
CSC	Cathode Strip Chamber
CTP	Central Trigger Processor
EC	End-Cap
EM	electromagnetic
FCal	Forward Calorimeter
FR	fiducial region
FSR	final-state radiation
HEC	hadronic end-cap Calorimeter
HL-LHC	High-Luminosity Large Hadron Collider
HLT	High-Level Trigger
IP	interaction point
ISR	initial-state radiation
L1	Level-1
LEP	Large Electron-Positron Collider

LINAC	linear accelerator
LH	left-handed
LHC	Large Hadron Collider
LHCb	Large Hadron Collider beauty
LO	leading order
LUCID	Luminosity measurement using Cherenkov Integrating Detector
MC	Monte Carlo
MDT	Monitored Drift Tube
MS	Muon Spectrometer
NLO	next-to-leading order
NNLO	next-to-next-to-leading order
OSSF	opposite-sign same-flavor
PDF	parton distribution function
PS	Proton Synchrotron
PSB	Proton Synchrotron Booster
QCD	Quantum Chromodynamics
QED	Quantum Electrodynamics
QFT	quantum field theory
RH	right-handed
RPC	Resistive Plate Chamber
SCT	Semiconductor Tracker
SM	Standard Model of particle physics
SPS	Super Proton Synchrotron
SR	signal region
SSB	spontaneous symmetry breaking
SSSF	same-sign same-flavor

TDAQ	Trigger and Data Acquisition
TGC	Thin Gap Chamber
TRT	Transition Radiation Tracker
vev	vacuum-expectation value
VR	validation region
WP	working point

Chapter 1

Introduction

From the first Trans-Atlantic voyages to the discovery of the Higgs boson [1, 2], humanity's drive to explore the unknown has endured. Today that same spirit is channeled into testing the Standard Model of particle physics (SM) [3, 4], a quantum field theory (QFT) that successfully describes the properties and interactions of the fundamental particles. Despite its remarkable predictive power, the SM is incomplete and several open questions persist: why is gravity absent, what is the nature of dark matter, and why does matter dominate over antimatter? Consequently, precise tests of the SM and its structure are crucial for uncovering physics beyond it.

The Large Hadron Collider (LHC) [5]—the world's highest-energy accelerator—offers the most powerful means of testing the fundamental properties of the SM. During Run 2 (2015–2018), the LHC delivered proton-proton collisions at a center-of-mass (COM) energy of 13 TeV, corresponding to an integrated luminosity of 140 fb^{-1} recorded by the ATLAS detector [6]. This unprecedented dataset provides sufficient statistics to study rare electroweak processes that directly probe the non-abelian gauge structure of the SM. Fully neutral triple- and quartic-gauge couplings are forbidden in the SM; any deviation would therefore be a clear sign of new physics.

In this thesis we focus on electroweak processes and present the first measurement of $ZZ\gamma$ production. By selecting events with two opposite-sign same-flavor (OSSF) lepton pairs and an isolated photon, we define a fiducial region. Additional selection criteria suppress photon final-state radiation (FSR) contributions and maximize the signal-to-background ratio. The two dominant background contributions are non-prompt photons from jets and misidentified leptons from hadron decays. Both are estimated with data-driven techniques: a newly developed jet-ratio method for the

non-prompt photons and the classic matrix method for the misidentified leptons. With the number of observed events and predicted background, the fiducial cross-section is measured for the first time.

The remainder of the thesis is structured as follows. Chapter 2 and Chapter 3 provide the theoretical and experimental background, respectively. Chapter 4 details the analysis strategy, event selection, and signal expectation. Chapter 5 discusses the estimation of all non-negligible background contributions. Chapter 6 presents the signal extraction, the measured cross-section, and its interpretation. Finally, Chapter 7 summarizes the main results and future prospects.

Author's contribution

The analysis presented in this thesis would not have been possible without the collective effort of the entire ATLAS Collaboration. This includes the full detector construction and operation, data processing and computing infrastructure, as well as the organized support structures for analyses, discussions, and technical guidance.

As part of the ATLAS Collaboration, I ensured the correct timing of the Level-1 (L1) Trigger through analysis of splash events and a high-statistics timing study of special runs. Furthermore, I helped monitor the events where the trigger was mistimed and was the primary person responsible for updating the code that tracks these events for the Run 3 Phase-I system. Additionally, I took part in monitoring detector operations during Run 3 in the ATLAS control room.

This thesis is based on the work I did as part of the analysis team. All results presented in Chapters 4 to 6, including the analysis strategy, event selection, and background estimation, are my own work, except for the derivation of the theoretical uncertainties and the initial idea for the non-prompt photon estimation. As part of my role as the analysis contact, I also took care of the sample processing (DAODs to nTuples), the overall structure and organization of the analysis (team), and communication with the collaboration. As one of the three paper editors, I wrote a significant part of the publication, replied to the comments, and was responsible for the technical details during the publication process. The publication presenting the $ZZ\gamma$ analysis has been submitted to *Physical Review Letters* and is available as a pre-print [7].

Chapter 2

Theoretical background

Particle interactions through the fundamental forces of the weak, strong, and electromagnetic interactions can be described by the laws of QFT, a theory combining quantum mechanics, field theory, and the concept of special relativity. The SM is formulated as a QFT and describes the underlying laws of particle physics. Although it is still incomplete (e. g., the masses of neutrinos), the model has proven to be very successful, and particle physicists around the world are testing its limitations.

This chapter will provide the theoretical foundation for the analysis of the $ZZ\gamma$ production process. First, the theory of the SM will be outlined in Section 2.1. Subsequently, an overview of triple-gauge-boson production will be presented in Section 2.2.

2.1 The Standard Model of particle physics

The SM is a renormalizable gauge theory [8] based on the

$$SU(3)_C \otimes SU(2)_L \otimes U(1)_Y$$

symmetry group [4]. This model describes the strong, weak, and electromagnetic forces. The $SU(3)_C$ group is the non-abelian gauge group of the strong interaction, Quantum Chromodynamics (QCD). The subscript C represents the quantum number of QCD, known as color. Only quarks and gluons carry color charge, and hence are affected by QCD [9]. The $SU(2)_L$ group is a chiral, non-abelian symmetry group that acts only on left-handed (LH) weak-isospin doublets [10]. The $U(1)_Y$ group is also chiral but abelian; it has the weak hypercharge Y as its quantum number and the B_μ field as its force carrier. The $SU(2)_L \otimes U(1)_Y$ symmetry describes the electroweak

interactions, the unification of the weak and electromagnetic forces [11]. After spontaneous symmetry breaking (SSB), the $SU(2)_L \otimes U(1)_Y$ symmetry group breaks down to the $U(1)_{\mathrm{EM}}$ group, with the massless photon as force carrier; the gauge bosons of the electroweak force—the $W^{\pm}$ and Z bosons—acquire mass [12].

The SM currently consists of 12 spin-1 gauge bosons, 12 spin-$\frac{1}{2}$ fermions with their corresponding antiparticles, and one spin-0 scalar boson. The spin-1 gauge bosons are eight massless gluons, the heavy $W^{\pm}$ and Z bosons, and the massless photon; these bosons are the force carriers of the strong and electroweak forces. The fermions come in three generations, ordered by increasing mass, and can be grouped into quarks and leptons. While all quarks have electromagnetic and color charges, only three leptons (e, μ, τ) have electromagnetic charge and none has color charge. The three neutral leptons are neutrinos, which interact only via the weak force. The Higgs boson is the spin-0 boson, and it gives mass to all massive particles in the SM [11]. A pictorial overview of the SM is displayed in Fig. 2.1.

The SM is described by a Lagrangian, which can be broken down into different components:

$$\mathcal{L}_{\mathrm{SM}} = \mathcal{L}_{\mathrm{gauge}} + \mathcal{L}_{\mathrm{kinetic}} + \mathcal{L}_{\mathrm{Higgs}} + \mathcal{L}_{\mathrm{Yukawa}}. \tag{2.1}$$

Here, $\mathcal{L}_{\mathrm{gauge}}$ is the Lagrangian for the gauge-bosons' kinetic terms, describing their interactions and self-interactions. The fermion kinetic terms and the interaction of fermions with the gauge bosons are described in $\mathcal{L}_{\mathrm{kinetic}}$. All interactions involving the Higgs bosons are contained in $\mathcal{L}_{\mathrm{Higgs}}$ and $\mathcal{L}_{\mathrm{Yukawa}}$ describes the Yukawa couplings resulting in the fermion mass terms [12]. We will describe the components of the Lagrangian in more detail in the following sections.

2.1.1 Gauge-bosons' kinetic terms

The Lagrangian of the gauge-bosons' kinetic terms is given by

$$\mathcal{L}_{\mathrm{gauge}} = -\frac{1}{4} G^a_{\mu\nu} G^{\mu\nu,a} - \frac{1}{4} W^i_{\mu\nu} W^{\mu\nu,i} - \frac{1}{4} B_{\mu\nu} B^{\mu\nu}. \tag{2.2}$$

The field-strength tensor of the gluon gauge field is $G_{\mu\nu}$. The $W_{\mu\nu}$ and $B_{\mu\nu}$ gauge fields are the field-strength tensors of the $SU(2)_L$ and $U(1)_Y$

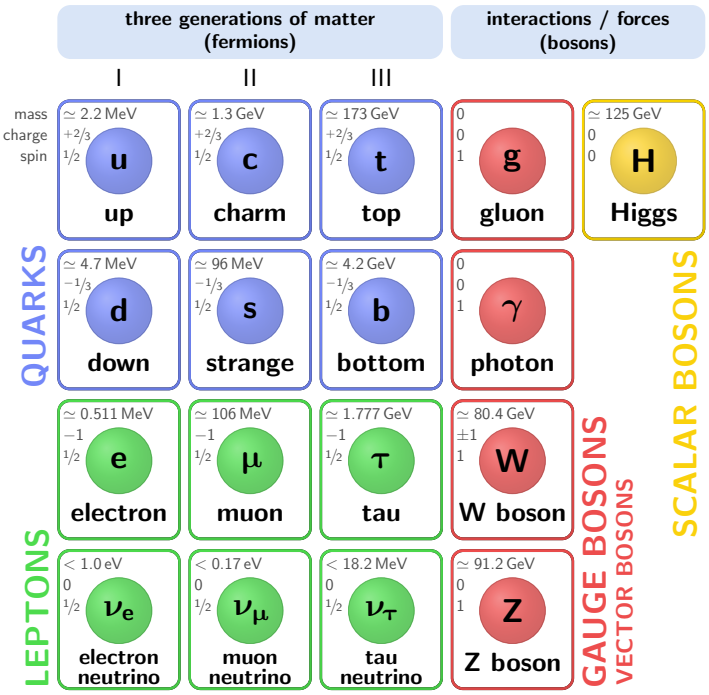


Figure 2.1: Pictorial representation of the Standard Model, taken and modified from [13]. The neutrinos are assumed to be massless in the SM, even though it has been proven that at least two neutrinos have mass [14].

symmetry groups, respectively. Since the $U(1)_Y$ group is abelian, its field strength is

$$B_{\mu\nu} = \partial_\mu B_\nu - \partial_\nu B_\mu. \tag{2.3}$$

In the case of the non-abelian $SU(3)_C$ and $SU(2)_L$ gauge groups, the field-strength tensors are given by

$$\begin{aligned} G^a_{\mu\nu} &= \partial_\mu G^a_\nu - \partial_\nu G^a_\mu - g_s f_{abc} G^b_\mu G^c_\nu \qquad a,b,c = 1,..,8 \\ W^i_{\mu\nu} &= \partial_\mu W^i_\nu - \partial_\nu W^i_\mu - g\epsilon_{ijk} W^j_\mu W^k_\nu \qquad i,j,k = 1,..,3. \end{aligned} \tag{2.4}$$

The gauge couplings of the $SU(3)_C$ and $SU(2)_L$ groups are g_s and g, respectively. These gauge groups have structure constants: f_{abc} for $SU(3)_C$

and ϵ_{ijk} for $SU(2)_L$ group. The non-abelian nature of the symmetry groups gives rise to the gauge-boson self-interactions [10, 12].

The interaction strength is proportional to the coupling strength and is determined by the coupling constant α. While in Quantum Electrodynamics (QED) the coupling strength decreases with distance, the opposite is true in QCD. This phenomenon is known as *running coupling*.

The self-interactions of the gluons result in the absence of free quark or gluon states at large distances (low energies). These particles are always confined in color-neutral hadrons, such as baryons (qqq) and mesons ($q\bar{q}$). Since the potential of the self-interaction grows stronger with distance, new gluons or quark-antiquark pairs are produced between the separating quarks and gluons, resulting in *hadronization*—the production of color-neutral bound states. While we have *confinement* at low energies, in the high energy regime the quarks and gluons are almost free, interacting weakly; this behavior is called *asymptotic freedom* [4, 9].

2.1.2 Fermion kinetic terms

For the fermion kinetic terms, the Lagrangian is given by

$$\mathcal{L}_{\text{kinetic}} = \bar{L}_i i\not{D} L_i + \bar{Q}_i i\not{D} Q_i + \bar{\ell}_{Ri} i\not{D} \ell_{Ri} + \bar{u}_{Ri} i\not{D} u_{Ri} + \bar{d}_{Ri} i\not{D} d_{Ri} + \text{h.c.}, \quad (2.5)$$

the slash notation refers to the contraction with the gamma matrices γ_μ and h.c. being the abbreviation for *Hermitian conjugate*. The covariant derivative D is given by

$$D^\mu = \partial^\mu + i g_S G_a^\mu L_a + i g W_i^\mu T_i + i g' B^\mu Y. \quad (2.6)$$

Here, L and Q are the LH isospin doublets for the three different generations and ℓ_R, u_R and d_R the right-handed (RH) singlets. The doublets are defined as

$$L = \begin{pmatrix} \nu_\ell \\ \ell^- \end{pmatrix} \qquad \text{and } Q = \begin{pmatrix} u \\ d \end{pmatrix} \quad (2.7)$$

with $\ell = e, \mu, \tau$, u up-type quarks (u, c, t) and d down-type quarks (d, s, b). Since the neutrinos are massless in the SM, there is no RH neutrino component. In the covariant derivative (Eq. (2.6)), G_a^μ, W_i^μ, and B^μ are the

eight gluon fields, the three weak-interaction fields, and the weak hypercharge field, respectively. The g' is the coupling constant associated with the $U(1)_Y$ group. The generators of the symmetry groups are L_a, T_i, and Y. They act only on their corresponding states, i. e. L_a acts only on color triplets, and T_i only on isospin doublets.

2.1.3 Higgs boson terms and gauge-boson masses

While the $SU(2) \otimes U(1)$ symmetry group describes the electroweak interactions well, the theory does not allow for any gauge-boson mass terms [15]. This contradicts the observed massive $W^{\pm}$ and Z bosons [16]. One solution to this problem is through SSB via the Brout-Englert-Higgs mechanism [17, 18]. Here, a complex scalar $SU(2)$ doublet Φ with a gauge-invariant so-called *Mexican-hat potential*:

$$V(\Phi) = -\mu^2 \Phi^\dagger \Phi + \frac{\lambda}{2} \left(\Phi^\dagger \Phi\right)^2, \quad \text{with } \Phi = \begin{pmatrix} \phi^+ \\ \phi^0 \end{pmatrix}, \tag{2.8}$$

is introduced, where μ and λ are parameters of the potential with $\mu^2 < 0$ [9]. This potential has one unstable local maximum at $\Phi = 0$ and a global, degenerate circle of minima whose radius equals the non-zero vacuum-expectation value (vev) $\frac{1}{\sqrt{2}}v$. Through the choice of a particular solution, the symmetry is spontaneously broken, giving mass to the gauge bosons [11].

This mechanism is embedded in the $SU(2)_L \otimes U(1)_Y$ symmetry and leads to the unification of the electromagnetic and weak interactions [19–21]. The $SU(2)_L \otimes U(1)_Y$ symmetry is spontaneously broken into $U(1)_{\text{QED}}$,

$$SU(3)_C \otimes SU(2)_L \otimes U(1)_Y \xrightarrow{\text{SSB}} SU(3)_C \otimes U(1)_{\text{QED}}$$

With the $U(1)_{\text{QED}}$ symmetry remaining, three out of four symmetries are broken, giving mass to three vector bosons—the $W^{\pm}$ and Z bosons. The remaining gauge boson stays massless and is the photon [22].

Because the complex scalar field has a non-zero vev, a massive excitation remains; this is the Higgs field [4]. The Lagrangian describing the Higgs

couplings is

$$\begin{aligned}\mathcal{L}_{\text{Higgs}} &= |D_\mu \Phi|^2 - V(\Phi) \\ &= |D_\mu \Phi|^2 + \mu^2 \Phi^\dagger \Phi - \frac{\lambda}{2} \left(\Phi^\dagger \Phi\right)^2,\end{aligned} \tag{2.9}$$

where the first term is the kinetic term with the covariant derivative as stated in Eq. (2.6). After SSB the Lagrangian becomes

$$\begin{aligned}\mathcal{L}_{\text{Higgs}} =& \frac{1}{4} g^2 W_\mu^- W^{\mu +} (v+h)^2 + \frac{1}{2} \frac{g^2 + g'^2}{4} Z_\mu Z^\mu (v+h)^2 \\ &- \mu^2 h^2 - \lambda v h^3 - \frac{1}{4} \lambda h^4,\end{aligned} \tag{2.10}$$

where h represents the Higgs field, which arises through the parametrization of the scalar doublet via the unitary gauge with [10, 15]

$$\Phi = \frac{1}{\sqrt{2}} \begin{pmatrix} 0 \\ h + v \end{pmatrix}. \tag{2.11}$$

The $W_\mu^\pm$ and Z_μ boson fields in Eq. (2.10) are combinations of the W_μ^i and B_μ fields according to

$$W_\mu^\pm = \frac{1}{\sqrt{2}} (W_\mu^1 \mp i W_\mu^2) \qquad \text{and} \qquad Z_\mu = \frac{1}{\sqrt{g^2 + g'^2}} (g W_\mu^3 - g' B_\mu). \tag{2.12}$$

The photon field A_μ is given by [19]

$$A_\mu = \frac{1}{\sqrt{g^2 + g'^2}} (g' W_\mu^3 + g B_\mu). \tag{2.13}$$

The kinetic terms describe the Higgs couplings to the massive gauge bosons through triple or quartic interactions and always involve two massive gauge bosons whose total electric charge is zero. The potential includes the Higgs boson triple and quartic self-interaction terms [3].

2.1.4 Yukawa coupling

While the Higgs mechanism solves the problem of massive gauge bosons, the Higgs field also provides the possibility of fermion mass terms. Due to the non-conserving gauge symmetry of the combination of LH doublets

and RH singlets, fermion mass terms are not allowed in the SM without the Higgs field. However, by adding the complex scalar Higgs field, invariance under gauge transformations is maintained [4]. The coupling between a fermion field and a scalar field is called a Yukawa coupling [12]. The SM Lagrangian of the Yukawa coupling is

$$\mathcal{L}_{\text{Yukawa}} = -y_\ell \bar{L}_i \Phi \ell_{Ri} - y_d \bar{Q}_i \Phi d_{Ri} - y_u \bar{Q}_i \Phi^c u_{Ri} + \text{h.c.} \tag{2.14}$$

with the Yukawa coupling constants y_ℓ, y_d, and y_u. To conserve the $U(1)_Y$ symmetry in the case of up-type quarks, the charge-conjugated Higgs doublet $\Phi^c = -i\sigma_2 \Phi^*$ is used, with σ_2 the second Pauli matrix. After SSB and using the unitary gauge parametrization, the Lagrangian can be written as

$$\mathcal{L}_{\text{Yukawa}} = -\sum_f \left(m_f \bar{f} f + m_f \frac{h}{v} \bar{f} f \right), \qquad \text{with } f = \ell, u, d. \tag{2.15}$$

Here, m_f is the fermion mass, defined as $m_f = \frac{y_f v}{\sqrt{2}}$. The first part of the Lagrangian gives the fermions their masses through the non-zero vev. The second part is the coupling between two fermions and the Higgs boson. This representation of the SM Yukawa coupling with the fields in the mass basis is the most general and does not include flavor indices or mixing matrices [4, 11].

We will briefly discuss the quark Yukawa couplings and their effects. In contrast to leptons, the flavor eigenstates of the quarks are not equal to their mass eigenstates. We can transition from the mass basis to the flavor basis with a unitary 3×3 rotation matrix. This matrix is called the Cabibbo-Kobayashi-Maskawa (CKM) matrix [23, 24], V_{CKM}, and the amplitude of the off-diagonal elements is proportional to the probability of flavor-changing weak interactions. The matrix has four parameters: three mixing angles and one phase. The phase is the only source of charge-parity violation in the SM [11, 12, 25].

We can now combine the different parts to write out the full SM La-

grangian,

$$\begin{aligned}\mathcal{L}_{\text{SM}} = &-\frac{1}{4}G^a_{\mu\nu}G^{\mu\nu,a} - \frac{1}{4}W^b_{\mu\nu}W^{\mu\nu,b} - \frac{1}{4}B_{\mu\nu}B^{\mu\nu} \\ &+ \bar{L}_i i\not{D} L_i + \bar{Q}_i i\not{D} Q_i + \bar{\ell}_{Ri} i\not{D} \ell_{Ri} + \bar{u}_{Ri} i\not{D} u_{Ri} + \bar{d}_{Ri} i\not{D} d_{Ri} + \text{h.c.} \\ &+ |D_\mu \Phi|^2 + \mu^2 \Phi^\dagger \Phi - \frac{\lambda}{2}\left(\Phi^\dagger \Phi\right)^2 \\ &- y_\ell \bar{L}_i \Phi \ell_{Ri} - y_d \bar{Q}_i \Phi d_{Ri} - y_u \bar{Q}_i \Phi^c u_{Ri} + \text{h.c.}.\end{aligned} \tag{2.16}$$

2.2 Triple-gauge-boson production

The Standard Model of particle physics has 19 independent free parameters that need to be experimentally determined [10]. We can probe the consistency of different parameters through a variety of measurements—over-constraining the SM. While we are trying to find deviations from the SM, a multitude of measurements are consistent with the present theory [26]. In the LHC era, with an unprecedented amount of data available, there are two complementary ways to test the limits of the SM: precision and rarity. The study of triple-gauge-boson production belongs to the second category. With the requirement of three gauge bosons in the final state, the production cross-section is drastically reduced.

Typical Feynman diagrams of the triple-gauge-boson production are presented in Fig. 2.2. These processes are among the few that involve triple and quartic gauge couplings at leading order (LO), resulting in a primary testing ground for probing the non-abelian nature of the weak interaction [27]. The exact cancellation of divergences from the interference of gauge-boson self-interactions and their interactions with the Higgs boson is essential for electroweak unification via SSB [28, 29]. Thus, studies of triple-gauge-boson production can test the theory of electroweak symmetry breaking.

An overview of the measured SM production cross-sections with the ATLAS detector at the LHC is given in Fig. 2.3. The cross-section measurements of triple-gauge-boson processes are shown in the lower-right corner. Despite their low cross-section and thus low number of expected events,

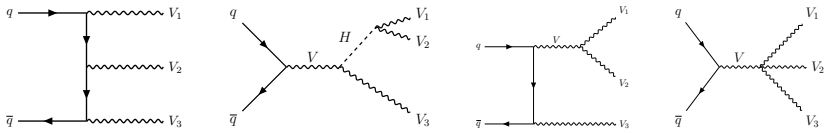


Figure 2.2: Typical Feynman diagrams producing triple-gauge-boson final states. Here, $V = \{Z, W^{\pm}, \gamma\}$, but not all combinations are allowed in the SM.

many triple-gauge-boson final states have been observed or measured, such as WWW [30], VVZ [31], $W\gamma\gamma$ [32], $WZ\gamma$ [33], and $Z\gamma\gamma$ [34]. However, the $ZZ\gamma$ final state remains unobserved. The full analysis and its first evidence will be presented in this thesis. Before detailing the analysis, the experimental setup will be described in the following chapter.

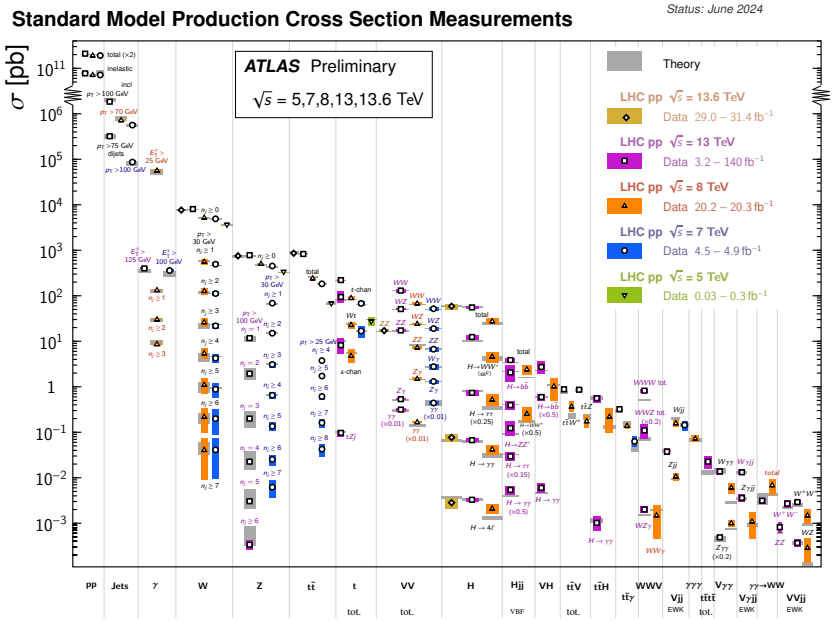


Figure 2.3: Cross-section measurements of Standard Model production processes from the ATLAS detector at the LHC, taken from [35].

Chapter 3

Experimental setup

By primarily colliding proton beams at luminosities up to $2.1 \cdot 10^{34}\,\mathrm{cm}^{-2}\mathrm{s}^{-1}$ and COM energies up to 13.6 TeV, the LHC is the most powerful tool to test the SM. As part of a large accelerator complex, the LHC belongs to the European Organization for Nuclear Research (CERN) and is located in Switzerland. Here, many experiments, such as the ATLAS experiment, share common resources and combined efforts, resulting in a wide-ranging physics program.

This chapter provides an overview of the experimental environment. The LHC, as part of an accelerator complex, will be outlined in Section 3.1, the ATLAS detector will be described in more detail in Section 3.2, and the reconstruction of particles traversing the ATLAS detector, as well as their simulation, will be presented in Section 3.3.

3.1 The Large Hadron Collider

The LHC is the highest-energy particle collider, located approximately 100 m underground in a 27 km long tunnel at the French-Swiss border [36]. The tunnel originally built for the Large Electron-Positron Collider (LEP) is repurposed to accommodate the main ring of the circular LHC. Due to the high beam intensity, the use of an antiproton beam is not feasible. Thus, two counter-rotating proton beams with opposite magnetic dipole fields need to fit in the same tunnel [5]. The ring contains dipole and quadrupole magnets, whose fields keep the particles on the LHC orbit and focus them [37].

The LHC accelerates particle beams that collide at four crossing points, also called interaction points (IPs) [5]. These four IPs house the four major

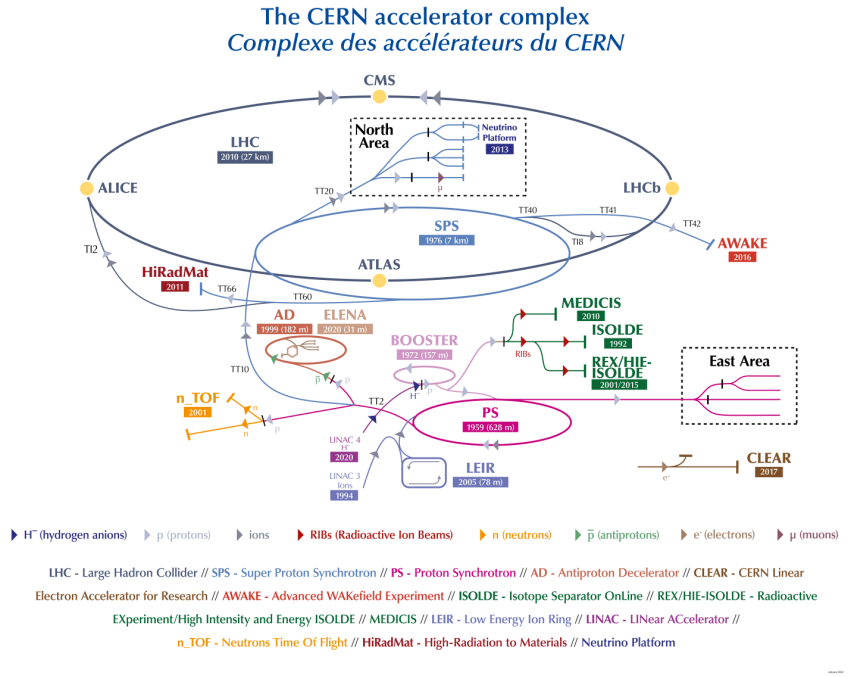


Figure 3.1: Schematic overview of the CERN accelerator complex with the LHC ring, its experiments, and injector chains. Taken from [42].

LHC experiments: A Large Ion Collider Experiment (ALICE) [38], the ATLAS experiment [6], the Compact Muon Solenoid (CMS) experiment [39], and the Large Hadron Collider beauty (LHCb) experiment [40]. While the ATLAS and CMS experiments have general-purpose detectors and a wide-ranging physics program to exploit the full potential of the LHC, the ALICE experiment focuses on heavy-ion physics and the LHCb experiment on flavor physics—especially *b*-physics. Besides protons, the LHC can be supplied with (heavy) ions, such as lead, which allows the study of extreme energy densities, such as quark-gluon plasma [41].

Before the particles enter the LHC, they are accelerated by an entire accelerator complex (see Fig. 3.1). In the case of protons, their journey starts as negatively charged hydrogen ions, which are accelerated in a linear accelera-

tor (LINAC) and stripped of electrons during the transfer to a booster. Up to 2018, LINAC2 supplied the Proton Synchrotron Booster (PSB) with 50 MeV protons. Since 2020, LINAC4 accelerates the protons to 160 MeV [43, 44]. In the PSB, the protons are further accelerated to 1.4 GeV and injected into the Proton Synchrotron (PS). Before transferring the protons to the Super Proton Synchrotron (SPS), they reach an energy of 26 GeV. The SPS supplies the LHC with 450 GeV protons, which can then be further accelerated up to the design COM energy of 7 TeV [45].

The LHC schedule is divided into different *run periods* for data-taking and *long shutdowns* for maintenance and upgrades. The data analysis in this thesis is from *Run 2*, the second data-taking period from 2015 to 2018. Currently, *Run 3* is ongoing, and after the next long shutdown, further data-taking periods with the High-Luminosity Large Hadron Collider (HL-LHC) will start [46, 47]. For the HL-LHC, the LHC will upgrade its injector complex to reach higher beam intensities and replace the focusing magnets to squeeze the beam further [36, 48].

3.1.1 Luminosity

The two key parameters that characterize particle colliders are the beam energy and its luminosity. The higher the COM energy, the heavier particles can be produced—or the smaller scales can be probed—and the larger the luminosity, the more collisions occur per unit time [49]. Luminosity, L, is a quantity that measures the number of interactions produced per unit time:

$$\frac{dR}{dt} = L\sigma. \tag{3.1}$$

Here, an interaction (event) is the collision of two particles; dR/dt is the number of events per unit time [50], and σ is the cross-section—a measure of the probability of a collision. In the LHC, we do not have individual particles colliding; instead, we have bunched beams with N particles per beam and a beam density ρ. Thus, the luminosity in a head-on collision is given by

$$L = 2N_1N_2fN_b \int\int\int\int \rho_1(x,y,z,t)\rho_2(x,y,z,t)\,\mathrm{d}x\,\mathrm{d}y\,\mathrm{d}z\,\mathrm{d}t, \tag{3.2}$$

where the indices 1 and 2 refer to the two beams, N_b is the number of bunches (packages of particles) per beam, and f is the revolution frequency. Assuming equal Gaussian beams with beam widths σ_x and σ_y, and head-on collisions, the definition of the luminosity simplifies to

$$L = \frac{N_1 N_2 f N_b}{4\pi\sigma_x\sigma_y} \tag{3.3}$$

Here, L is the luminosity at a given moment in time and is called *instantaneous* luminosity. In contrast, the *integrated* luminosity, $\mathcal{L}$, is defined as $\mathcal{L} = \int L \, \mathrm{d}t$. Since the integrated luminosity $\mathcal{L}$ directly relates the number of events to its cross-section,

$$N = \mathcal{L}\sigma, \tag{3.4}$$

the precise knowledge of it is crucial [49, 50].

3.2 The ATLAS detector

The high interaction rates, radiation doses, and requirements for precision measurements of different particle signatures demand a custom-built detector. The ATLAS experiment is a cylindrical detector with different layers of custom-made sub-detectors surrounding the IP[1]. The detector provides full azimuthal angle coverage and a large pseudorapidity acceptance with its central barrel and two End-Cap (EC) structures.

The innermost part, the Inner Detector, provides precise tracking information for charged particles. Their trajectories are bent by the superconducting solenoid, which surrounds the Inner Detector. Electromagnetic and hadronic showers are mostly contained, and their energies are measured in the electromagnetic (EM) and hadronic calorimeters around the solenoid. The outermost layer is the muon spectrometer, which is immersed in the

[1] ATLAS uses a right-handed coordinate system with the origin at the nominal IP at the center of the detector. The z-axis is along the beam line, while the x-axis points towards the center of the LHC ring and the y-axis points upwards. Most of the time spherical coordinates are used with the azimuthal angle ϕ around the z-axis in the transverse plane, and the polar angle θ from the beam axis. The pseudorapidity is defined as $\eta = -\ln\tan(\theta/2)$ and, in the relativistic limit, agrees with the rapidity y, $y = \frac{1}{2}\ln\left(\frac{E+p_z}{E-p_z}\right)$. Angular distances are defined as $\Delta R \equiv \sqrt{(\Delta\eta)^2 + (\Delta\phi)^2}$ [6].

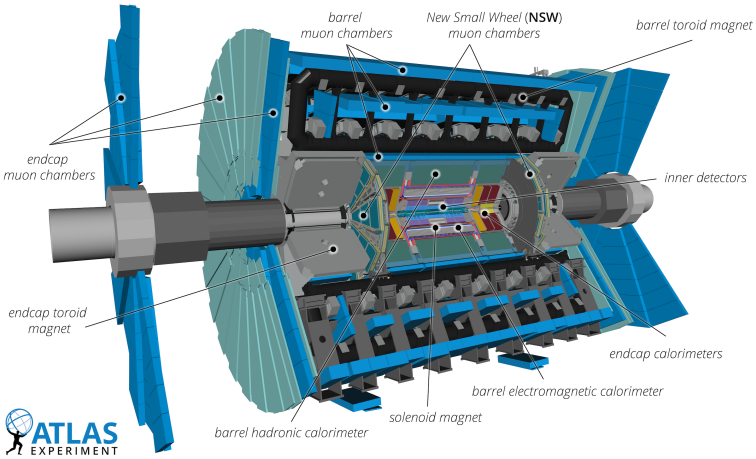


Figure 3.2: Schematic overview of the ATLAS detector for Run 3. The new small wheel muon chambers were installed during the long shutdown between Run 2 and Run 3. The remaining layout of the detector has not been changed. Taken from [55].

magnetic field of the three large superconducting toroids [6, 51]. Events are selected by successfully passing the L1 trigger and the High-Level Trigger (HLT) [52].

A schematic overview of the detector is presented in Fig. 3.2 and will be described in more detail in the following sections. While the ATLAS detector is the main part of the experiment, smaller detectors such as Luminosity measurement using Cherenkov Integrating Detector (LUCID)-2 [53] or Absolute Luminosity for ATLAS (ALFA) [54] provide crucial information about luminosity measurements and the total inelastic proton-proton (pp) cross-section.

3.2.1 The magnet system

The ATLAS detector has a central solenoid and three toroidal magnets: one barrel toroid and two EC toroids. These magnets provide the necessary bending power to measure charged-particle momenta [6, 56]. The superconducting solenoid is located in the center of the experiment and creates

a 2 T magnetic field in the Inner Detector [57]. The three superconducting toroids have eight coils, which are radially and symmetrically arranged around the beam line. Here, the EC toroids are rotated by 22.8° for optimal bending power [56, 58].

3.2.2 The Inner Detector

The Inner Detector is immersed in the solenoid field and provides tracking information for charged particles up to $|\eta| < 2.5$ through its three independent, complementary sub-detectors [6].

The innermost sub-detector is the silicon-pixel detector, providing precision tracking and secondary-vertex positions near the IP. The three pixel layers are accompanied by a fourth layer—the Insertable B-layer, which was installed closest to the beam pipe before the start of Run 2 [59, 60].

The pixel detector is surrounded by the Semiconductor Tracker (SCT), with four layers of silicon-strip sensor modules in the barrel and nine disks in the ECs [61].

The outermost part of the Inner Detector is the Transition Radiation Tracker (TRT), where straw tubes are used as tracking drift chambers. The spaces between the straws are filled with fiber/foil to create transition radiation for electron identification [59, 62]. The TRT is separated into a barrel and two EC detectors, providing approximately 35 hits per track [63, 64].

3.2.3 The calorimeters

The calorimeters of the ATLAS detector cover a pseudorapidity range of $|\eta| < 4.9$. A fine-granularity EM sampling calorimeter with liquid argon as the active material and lead absorber plates covers the pseudorapidity up to $|\eta| = 3.2$. The calorimeter has accordion-shaped layers for full azimuthal coverage and uses liquid argon for its radiation hardness, linear behavior, and stability. The EM sampling calorimeter is split into a barrel and two EC parts, resulting in a transition region ($1.37 < |\eta| < 1.52$) between them [6, 65]. To minimize the energy loss of particles in front of the calorimeters, their vacuum vessel is shared with the solenoid. Additionally, a pre-sampler

corrects for the energy loss from upstream material [66].

The hadronic sampling calorimeter with steel absorbers and plastic scintillating tiles covers the pseudorapidity $|\eta| < 1.7$. It consists of a long barrel and two extended barrels with the tile gap ($1.0 < |\eta| < 1.1$) in between [67]. The hadronic tile calorimeter is accompanied by the hadronic end-cap Calorimeters (HECs), two wheels each containing a liquid-argon sampling calorimeter and copper absorber plates on each EC [68].

In the forward regions ($3.2 < |\eta| < 4.9$), additional EM and hadronic calorimeters—the Forward Calorimeters (FCals)—are installed to extend the energy measurements to higher pseudorapidities. The FCals experience high radiation and thus have, per side two layers of tungsten (hadronic) and one layer of copper (EM) as absorbers, and liquid argon as active material [66].

Overall, the different ATLAS calorimeters not only cover a large pseudorapidity range but also contain the EM and hadronic showers well. The EM calorimeters have a depth of up to $24\,X_0$ (radiation length), and the hadronic calorimeters extend to $11\,\lambda$ (interaction length) [6].

3.2.4 The muon system

The high-resolution Muon Spectrometer (MS) has precision tracking chambers for $|\eta| < 2.7$ as well as standalone triggering chambers for $|\eta| < 2.4$. The muon trajectories are deflected by the three large air-core toroids and measured by three layers of Monitored Drift Tubes (MDTs) or Cathode Strip Chambers (CSCs). The MDTs are precision tracking chambers made of aluminum tubes with wires inside. Closest to the beam pipe and at larger pseudorapidities, CSCs—multi-wire proportional chambers with cathode-strip readout—are used due to the high background.

For triggering, Resistive Plate Chambers (RPCs) and Thin Gap Chambers (TGCs) are implemented in the barrel and ECs, respectively. While RPCs are gaseous detectors with narrow gas gaps between two parallel resistive plates, TGCs are multi-wire proportional chambers with a small wire distance resulting in a short drift time. Besides triggering information, these chambers also provide information on the bunch-crossing identification and the second coordinate of the muon trajectories [6, 69].

3.2.5 The trigger and data acquisition system

The main functions of the Trigger and Data Acquisition (TDAQ) system are managing the data flow and online event selection [70]. The ATLAS experiment has a two-level trigger system for filtering and selecting events—the hardware-based L1 trigger with custom electronics and the software-based HLT.

The L1 trigger reduces the event rate from 40 MHz to 100 kHz with a latency of 2.5 μs [6, 71]. The trigger decision is made by the Central Trigger Processor (CTP) after receiving reduced granularity information from the L1 Calorimeter trigger and the L1 Muon trigger, as well as topological requirements from the L1 topological trigger. In case of a *L1 Accept*, *Regions-of-Interest* are sent to the HLT.

With fast trigger algorithms to reject events early and more computationally intensive and precise algorithms thereafter, the HLT reduces the event rate to 1.2 kHz. All events passing the HLT are sent to permanent storage for further offline analysis [52].

3.3 Particle reconstruction

The particles created in pp collisions at the IP traverse the ATLAS detector, leaving characteristic signatures. This section will provide an overview of the signals generated by each sub-detector and how they are combined to reconstruct properties of different particles. The reconstruction of objects relevant for the analysis, e. g., electrons, photons, and muons, will then be described in more detail.

3.3.1 Particle signatures

Charged particles traversing the Inner Detector leave hits—signals in the sub-detectors. The hits are combined into tracks using the Kalman-filter algorithm [72]. The track curvature depends on the particle's transverse momentum and charge.

In the EM calorimeters, particles deposit their energy through material interactions with the lead absorbers. The deposited energy is measured in

the active material, liquid argon, via ionization. Highly energetic particles, especially hadrons, produce large showers that extend to the hadronic calorimeters. Here, the deposited energy is measured by scintillating tiles or liquid argon.

The minimum-ionizing muons and some extremely high-energy particles can reach the muon spectrometer, where the charged particles are bent by the magnetic field, and leave signals in the tracking and triggering chambers. Through the combination of these signals, tracks can be reconstructed [45, 51].

3.3.2 Reconstruction overview

Electron and photon candidates are reconstructed through their energy deposits in the EM calorimeters. Additional information from the Inner Detector is needed to differentiate between electrons, converted and unconverted photons. Converted refers to photons producing an electron-positron pair in the Inner Detector via material interaction. While the photons leave no hits in the Inner Detector, the electron-positron pair does. This results in a conversion vertex with oppositely bent hits emerging from it. Energy deposits matched to a track in the Inner Detector are reconstructed as electrons. If no track is matched to the energy deposit, it is reconstructed as unconverted photon, and matched conversion vertices are reconstructed as converted photons [73].

Muon candidates are objects that have matched tracks in the Inner Detector and the MS [74].

Neutrinos escape the detector without leaving any signals behind. The only way to reconstruct neutrinos is indirectly through the energy imbalance. Energy conservation demands that the total transverse energy be the same before and after the collision. Since the transverse energy is zero before the collision, the vector sum of all energy deposits must cancel. Thus, the missing energy can be inferred from the sum of the measured energy [45, 51].

Quarks or gluons are not observed as free particles due to confinement. Their hadronization results in a multitude of collimated objects defined as jets. Specific algorithms are needed to group the energy deposits from the

particles together. The ATLAS experiment uses the anti-k_T algorithm [75, 76] based on recursive clustering of the energy clusters. To compensate for energy losses, e. g., from decays into neutrinos, or energy deposits from other *pp* collisions in the same or neighboring bunch crossings, sophisticated energy-scale calibrations are applied to reconstructed jets [77].

3.3.3 Primary vertex reconstruction

Vertices are the interaction points of particle collisions or decays. In the ATLAS detector, the primary vertices refer to the collisions of the incoming protons and lie along the beam line. Secondary vertices are displaced vertices originating from material interactions or decays of particles that travel a measurable distance in the detector [78].

For the reconstruction of the primary vertices, a subset of all reconstructed tracks is used. These tracks are required to have a minimum transverse momentum of 400 MeV, a sufficient number of hits in the Inner Detector, and to fulfill minimum transverse and longitudinal impact-parameter requirements [79]. The transverse impact parameter, d_0, is the transverse distance of the track's closest approach to the beam line, and the longitudinal impact parameter is the z position at the track's closest approach [51].

An iterative fitting algorithm estimates the best vertex position for the tracks. Not all tracks belong to a single vertex. Thus, the algorithm chooses a subset of tracks for one primary vertex and applies the same fitting procedure to the remaining tracks until no tracks are left.

Of all reconstructed primary vertices from one *pp* collision, approximately one belongs to the hard-scatter physics process. This vertex has the highest sum of squared transverse momenta of the contributing tracks [79, 80]. In the following, this vertex is called the primary vertex, and all other primary vertices are called pileup vertices. Pileup refers to all *pp* interactions other than the hard-scatter in the same or neighboring bunch crossings [81].

3.3.4 Electron and photon reconstruction

Electron and photon candidates start by dynamically and topologically clustering EM calorimeter cells into EM topological clusters. Afterwards,

the track candidates reconstructed in the Inner Detector are matched to the topological clusters [73].

An electron candidate is reconstructed if a track matches the topological cluster; a primary track with hits in the innermost two layers is chosen. To reduce the background contribution from non-prompt electrons that are reconstructed as electron candidates, further identification and isolation requirements are imposed.

Regarding the candidate identification, three working points (WPs) with fixed efficiencies for a prompt electron to pass each WP are defined—loose (93%), medium (88%), and tight (80%). Lateral and longitudinal shower-development variables, as well as track-quality criteria, are used to create signal- and background-likelihood distributions. Different thresholds of the likelihood discriminant define the WPs.

For calorimeter isolation, the energy of all clusters whose barycenter lies within a fixed radius around the EM topological cluster is selected and summed. The energy of the particle candidate is subtracted, as well as leakage and pileup correction. Track isolation is sum of the momenta of good-quality tracks with $p_{\mathrm{T}} \geq 1\,\mathrm{GeV}$ in a cone around the primary track. Photon conversions and bremsstrahlung are not included. For particle isolation, different WPs are defined with thresholds on calorimeter and tracking isolation [73, 82–84].

Photon candidates are classified into two categories: if a reconstructed conversion vertex is matched to an EM topological cluster, the photon is classified as converted; otherwise, it is classified as unconverted. Similar to electron candidates, identification and isolation requirements are imposed on photon candidates.

The loose identification WP of photons is defined through one-dimensional selection criteria on shower shape variables and calorimeter energy. The tight identification WP is optimized differently for converted and unconverted photons using a multivariate analysis. The definition of calorimeter isolation for photons is the same as for electrons. For track isolation, the momenta of tracks matching a cone around the EM topological cluster direction are summed [73, 82–85].

3.3.5 Muon reconstruction

Muons are minimum-ionizing particles that leave a signature in all detectors. The reconstruction of muons primarily combines tracking information from the MS and the Inner Detector. Additional information from calorimeters and the second-coordinate measurement of the MS triggering chambers is used as well [74].

For MS tracks, hits in the MDT or CSC are grouped into segments according to the Hough transform [86]. These segments are fitted together with the second-coordinate measurements of the RPC/TGC to form track candidates [87]. There are five different types of muon candidates, depending on what information is used and how it is combined. Muon candidates used in analyses are mainly *combined muons*, where MS track candidates are combined with Inner Detector track candidates and energy losses in calorimeters by applying a combined track fit. Extrapolated Inner Detector tracks that are then combined with MS hits and calorimeter information to recover MS inefficiencies are called *inside-out combined*. The other muon types (MS extrapolated, segment-tagged, and calorimeter-tagged) use information from only one or two subsystems and are lower-quality muon candidates [74].

To increase the selection efficiency and purity of muon candidates, further identification and isolation requirements can be imposed. Five identification WPs are defined: while most analyses use the tight, medium, and loose WPs, which are subsets of each other, a high-p_{T} and a low-p_{T} WP exist for targeting extreme phase spaces. The tighter the WP, the higher-quality muon candidates are selected; consequently, more track hits are required, stricter track-fit criteria are imposed, and the compatibility among the Inner Detector, calorimeters, and MS information improves.

Muon isolation WPs are constructed similarly to electron and photon WPs: in a cone around the muon candidate, track-based and calorimeter-based isolation are defined as the sum of transverse-momentum tracks or the sum of EM topological clusters, respectively. The isolation WPs use different thresholds for isolation; most WPs combine track- and calorimeter-based isolation information to improve performance [74, 87, 88].

3.4 Simulation of proton-proton collisions

To understand and analyze the reconstructed data from the ATLAS detector, theoretical predictions and their simulations are needed. However, the exact modeling of the multidimensional distributions with limited theoretical understanding and computationally heavy integrations is, by today's standards, an impossible task to perform. The use of Monte Carlo (MC) sampling techniques, to select variables from probability density functions, and the factorization into different steps, results in event generators describing the physical processes and their experimental characteristics sufficiently [89].

We will give an overview of the different components and limitations of a general-purpose event generator in the next section, followed by a short description of the detector simulation and event-weighting.

3.4.1 Event simulation

The event generators simulate the physics process of interest with corresponding parameters (e. g., COM, beam). Starting with the inclusive cross-section calculation of the hard interaction (e. g., $\sigma_{pp\to X}$), most event generators factorize the integration into the matrix element at fixed order in perturbation theory, and the parton distribution functions (PDFs) of the incoming particles.

The order in perturbation theory refers to the order of the strong coupling constant, α_s, present in the matrix-element calculation. While LO refers to the tree-level calculation, next-to-leading order (NLO) or next-to-next-to-leading order (NNLO) include an increasingly larger amount of (loop) corrections [90].

At LO, the PDFs of the incoming particles represent the probability to find a parton—quark or gluon—in the hadron (e. g., proton) depending on the momentum fraction x of the hadron carried by the parton [91]. The integration over the PDFs of the incoming particles determines the rate of the physics process. Since the PDFs cannot be determined accurately from the current theoretical understanding of QCD and the available computing power, a global fit to all deep-inelastic and hard-scattering data at different

energy scales is performed [92, 93].

After the inclusive cross-section calculation, the event generators simulate (QCD) bremsstrahlung from the initial- and final-state particles, called initial-state radiation (ISR) and FSR, respectively. While ISR results in parton radiation in the direction of the incoming particles, FSR can happen from any particle after the hard interaction and is also responsible for the broad jet structure. These radiation processes are referred to as parton shower. Through the iterative branching of one particle into two particles under flavor and four-momentum conservation, the parton shower produces approximate higher-order real-emission corrections to the inclusive cross-section [89, 90, 94].

So far, only radiation from the hard interaction has been considered. However, more than one parton-parton interaction can take place during a hadron-hadron collision. These interactions can occur either through the color charges of partons within the hadron, or via additional parton-parton interactions resulting from the hadron-hadron collision, and are referred to as the underlying event [95]. These semi-hard parton-parton interactions are described by independent models, such as those developed by Sjöstrand and van Zijl [96].

Due to color confinement, all partons from the hard interaction, the parton shower, and the underlying event must hadronize into observable, color-neutral bound states. This transition is implemented through models such as the Lund string model [97, 98] or the cluster model [99–101]. While both models form color-connected singlets and decay non-perturbatively, the Lund string model is based on string fragmentation, treating the color singlets as connected strings that fragment into hadrons. The cluster model, on the other hand, is based on pre-confinement, treating the color singlets as massive clusters that decay into hadrons [90, 102].

3.4.2 Detector simulation

Through the combination of the previously described steps, event generators simulate particle interactions at the so-called *particle level*, independent of the detector. To use the output of the event generators for detector corrections, performance optimizations, analysis optimizations, and comparisons

to data, a simulation of the modeled particles as they pass through the detector is necessary [89].

In the case of the ATLAS experiment, the detector simulation is performed using GEANT4 [103], a toolkit for simulating particle interactions with matter. The detector simulation involves the geometry of the system, material densities and distributions, as well as detector components and their response to particle interactions.

By combining event generation with detector simulation, the simulation of particle collisions and their corresponding detector responses is obtained. For the ATLAS experiment, the full event simulation produces output in a hit format identical to that of the detector output format. The output of both—data and simulated events—are digitized. Simulated events are then overlaid with additional pp interactions (pileup), and noise is added to create a more realistic setting.

Energy, trajectories, and transverse momenta are reconstructed using the same algorithms for both event types. After completing the full simulation chain, the data and simulated events can be compared for calibration or analysis purposes at the so-called *reconstruction level* [104].

3.4.3 Weights and scaling

An advantage of simulations is the possibility of increasing the number of simulated events arbitrarily; however, computational resources are normally the limiting factor and trade-off against unlimited statistical precision. In order to save computing resources while maintaining a high statistical precision, event weights have been introduced. The weights reflect the relative probability of the event. Since we want to compare simulation to data, we are interested in the number of selected events, N_{sim}, for a given integrated luminosity. Thus, the selected events with weights, w_{sel}, need to be scaled according to:

$$w_{\text{sel}} \Rightarrow w_{\text{sel}} \frac{\sigma_{\text{sim}} \mathcal{L}}{\sum_i w_i}, \tag{3.5}$$

with the simulated cross-section σ_{sim}, the integrated luminosity $\mathcal{L}$, and the sum of all simulated weights $\sum_i w_i$ for normalization.

The simulated events in the MC event generator samples are additionally reweighted to minimize differences between simulation and measurement. For all simulated efficiencies (e. g., reconstruction, identification, isolation, and trigger), correction factors—also called *scale factors*—with their uncertainties are determined [73]. These scale factors are used to correct each event weight.

Chapter 4

The $ZZ\gamma$ analysis

The analysis to determine the $ZZ\gamma$ production cross-section will be presented in this thesis. Due to the low cross-section of this triple-gauge-boson production process, which results in a low number of produced events, the measurement of the $ZZ\gamma$ production has not been achieved earlier. In recent years, an unprecedented integrated luminosity has been delivered by the LHC, addressing the low event rate. The analysis uses the full Run 2 dataset taken by the ATLAS detector at the LHC between 2015 and 2018, corresponding to an integrated luminosity of 140 fb^{-1}, and recorded at a COM energy of $\sqrt{s} = 13\,\text{TeV}$. While this Run 2 dataset contains billions of events, only a very few are expected to originate from the $ZZ\gamma$ production. The $ZZ\gamma$ analysis, with its optimized event selection and precise estimation of the background, yields the first evidence of the $ZZ\gamma$ production.

In the following, the overall analysis strategy for the measurement of $ZZ\gamma$ production will be described. Subsequently, the event selection, with its characteristic criteria, will be presented in Section 4.2, and the expected signal contribution with its uncertainties will be outlined in Section 4.3.

4.1 Analysis strategy

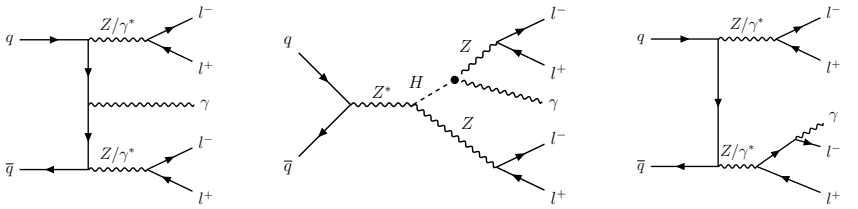
The analysis of the measurement of $ZZ\gamma$ production must fulfill three main requirements: efficiently selecting the signal contribution, suppressing background, and estimating the remaining background with high precision to achieve in a sufficiently large signal significance. The analysis is performed blinded to prevent bias. This means that data fulfilling the signal selection are not used for any selection optimization or background estimation.

This analysis focuses on the leptonic decays of both Z bosons into electrons or muons. The hadronic decay channels cannot be distinguished from large background contributions. The Z-boson decays into tau leptons are not explicitly considered. The tau leptons decay within the ATLAS detector and their reconstruction is not precise enough. While they mainly decay hadronically—not feasible due to the large background contribution—, their leptonic decay contains missing transverse momentum due to the neutrinos, resulting in a poor reconstruction of the invariant Z-boson mass. However, tau leptons decaying to electrons or muons and passing the selection criteria are considered signal. While this choice reduces the cross-section ($\sigma_{ZZ\gamma}(p_{\mathrm{T}}^{\gamma} > 15\,\mathrm{GeV}) \sim 30\,\mathrm{fb}$) by a factor of 200, it results in a very clean final state: two pairs of OSSF leptons and one photon, $\ell^+\ell^-\ell'^+\ell'^-\gamma$ ($4\ell\gamma$) with $\ell, \ell' = e$ or μ.

The production of the fully leptonic $ZZ\gamma$ final state is predominantly produced via Feynman diagrams such as those shown in Fig. 4.1a. The three gauge bosons are all produced through an incoming quark-antiquark pair. We refer to these processes as *direct production*.

The same final state can be produced through Higgs radiation from a Z boson, referred to as *Higgs contribution*. A typical production diagram of this process is given in Fig. 4.1b. The cross-section of the radiation of a Higgs boson off a Z boson is relatively large ($\sigma \sim 0.9\,\mathrm{pb}$ [105]) but the branching ratio of the Higgs boson into a Z boson and a photon is loop-suppressed, and thus very low ($BR_{H\to Z\gamma} \sim 10^{-3}$ [106]), resulting in an overall small but not negligible contribution to the $4\ell\gamma$ final state. The Higgs contribution contains $ZZ\gamma$ production and is considered part of the signal.

Another process results in the same $4\ell\gamma$ final state: ZZ production with a photon being radiated off one of the final leptons, see Fig. 4.1c. Events from this production are called *final-state radiation* events. Due to the significantly larger cross-section of ZZ production ($\sigma \sim 17\,\mathrm{pb}$ [35]) relative to the expected $ZZ\gamma$ production, even with a tight $ZZ\gamma$ event selection, more than two out of three events are FSR events. While the final state of the FSR events is indistinguishable from the final state of the signal process, other event characteristics and properties provide discriminating power, such as the isolation of the radiated photon or the invariant mass of



(a) Direct production **(b)** Higgs contribution **(c)** Final State Radiation

Figure 4.1: Typical Feynman diagrams that produce an $\ell^+\ell^-\ell'^+\ell'^-\gamma$ final state. The dominant production of the $ZZ\gamma$ final state can be represented by Feynman diagrams of the type presented in (a). A non-negligible signal contribution comes from processes with Higgs strahlung, represented by Feynman diagrams such as (b). Since the Higgs boson does not directly decay into a Z boson and a photon, the decay is represented by an effective coupling in the Feynman diagram. Final-state photon radiation off a lepton from ZZ production results in the same final-state particles; see (c). The FSR contribution is suppressed in the signal selection.

the OSSF pair with the FSR photon. It is crucial to suppress FSR events in the signal selection to ensure that only $ZZ\gamma$ production events are selected.

For the measurement of $ZZ\gamma$ production, each event must pass a set of selection criteria to be analyzed further. A signal region (SR) is defined where the signal-to-background ratio is maximized. In this selection, the final-state particles are required to satisfy minimum transverse-momentum, isolation, and identification criteria. Additionally, event characteristics of the signal and background processes are used to optimize the signal selection. A description of the selection will be given in Section 4.2.

Given the event selection, the signal contribution—including its kinematic distributions and characteristics—must be fully understood. For this, MC event simulations of the processes shown in Fig. 4.1 are studied. The simulations are also used to estimate the theoretical and experimental uncertainties on the signal. A summary of these studies will be presented in Section 4.3.

Although the event selection is optimized to reject as much background as possible, a remaining fraction of around 12% is still present. For the study

of the $ZZ\gamma$ signal sensitivity, it is crucial to understand the different sources of background and estimate their contributions with the highest possible accuracy. Various MC simulations and the analysis of data in regions orthogonal to the blinded SR, referred to as control regions (CRs), are used for background estimation. Three different background sources with non-negligible contributions have been identified: non-prompt photon events from e. g., ZZ events (9%), events with misidentified or non-prompt leptons, e. g., from $WZ\gamma$ or $t\bar{t}\gamma$ events, (2%), and pileup (1%).

The non-prompt photon contribution is estimated using a ratio method due to the limited statistics in the phase space close to the signal selection. Data-driven approaches are used to estimate the number of non-prompt photon events in a $Z\gamma$ CR, which are extrapolated into the SR.

A data-driven matrix method, applied in a ZZ CR without any photon requirements (to avoid limited statistics), is used to derive the misidentified and non-prompt lepton background.

Pileup is a combinatorial background arising from the simultaneous production of a ZZ event and a single photon event in the same bunch crossing. The background is estimated by overlaying MC event simulations.

The study and estimation of the different contributions, including their uncertainties, will be outlined in Chapter 5.

After the full study of signal and background events, the data are unblinded. The signal extraction results in the measurement of the fiducial cross-section and is compared to the SM expectation. The results and their interpretation will be detailed in Chapter 6.

4.2 Event selection

This analysis applies a classical event selection with predefined thresholds and selection criteria to select the $ZZ\gamma$ events in the Run 2 dataset. The set of conditions can be separated into a baseline selection, which will be fulfilled by all events in every region (SR and CRs), and a tighter signal selection, defining the SR.

4.2.1 Baseline selection

The baseline selection imposes minimum event-selection criteria and loose object-selection requirements on electrons, muons, photons, and jets. The first requirement of each event is to be on the *Good Run List*. All events on the list are recorded during normal detector operating conditions and pass the data quality requirements as described in Ref. [107].

Each selected event must have a reconstructed primary vertex, and one of the considered triggers must have fired. These two selection criteria ensure that the event has a hard interaction and contains at least one of the final-state particles with sufficient transverse momentum. The $ZZ\gamma$ analysis uses unprescaled single- and dilepton triggers with the lowest transverse-momentum thresholds; a detailed list is given in Appendix A.1.

Unprescaled (prescale factor $= 1$) means that every event that fulfills the trigger requirements is selected. Prescaled triggers with a prescale factor of n only select every n^{th} event passing its conditions. If lower thresholds are needed, triggers can be prescaled to reduce the rate.

With a photon and leptons in the final state, single-photon triggers as well as lepton triggers are of interest. The unprescaled single-lepton trigger with the lowest transverse-momentum threshold in 2016–2018 requires a lepton with a transverse momentum of $p_{\text{T}}^{\ell} > 26\,\text{GeV}$ [108, 109]. The lepton with the highest transverse momentum, referred to as the *leading lepton*, has a transverse-momentum distribution peaking around $p_{\text{T}}^{\ell} \sim 60\,\text{GeV}$, well above the trigger threshold.

Since this trigger has additional requirements on identification and isolation, single-lepton triggers with higher transverse-momentum thresholds and looser identification and isolation requirements, as well as dilepton triggers with even lower transverse-momentum thresholds, are considered as well. The combination of these triggers, with a logical *OR*, results in a fully efficient selection and the least biased dataset. Thus, there is no need to include any single-photon or prescaled triggers.

To reduce the introduced bias as much as possible, all events from MC simulations are required to have been triggered by one of the above-mentioned triggers. The trigger requirements and inefficiencies are implemented in the detector simulation. Additional scale factors are derived by

reweighting the simulations to match data, resulting in good agreement.

Next, we consider the selection criteria for the particle candidates of the $4\ell\gamma$ final state. Lepton candidates—electrons and muons—must have a minimum transverse momentum of $p_{\mathrm{T}}^{\ell} > 10\,\mathrm{GeV}$. The reconstruction algorithms become inefficient for leptons with lower transverse momenta.

Electron candidates must pass the loose identification WP [73] (see Appendix A.2.1) and their absolute pseudorapidity must satisfy $|\eta| < 2.47$. This pseudorapidity limit comes from the limited coverage of the precision tracking of the Inner Detector, which provides discrimination between electron and photon candidates. Electron candidates with pseudorapidities within the transition region—the gap between the barrel and end-cap EM calorimeters ($1.37 < |\eta| < 1.52$)—are excluded due to dead material and reduced instrumentation in this region.

Additionally, requirements on transverse and longitudinal impact parameters increase the probability that the electron track originates from the primary vertex. Thus, a transverse-impact-parameter significance, $|d_0|/\sigma_{d_0}$, of less than 5 is required, and the longitudinal impact parameter, z_0, must satisfy $|z_0 \sin(\theta)| < 0.5\,\mathrm{mm}$ [80, 110].

Muon candidates must have an absolute pseudorapidity less than $|\eta| < 2.5$, pass the medium identification WP [87] (see Appendix A.2.1), have a d_0 significance of less than 10, and also satisfy $|z_0 \sin(\theta)| < 0.5\,\mathrm{mm}$ [74].

Photon candidates are required to have a transverse momentum of $p_{\mathrm{T}}^{\gamma} > 15\,\mathrm{GeV}$, a loose identification WP [73] (see Appendix A.2.1), and a pseudorapidity of $|\eta| < 2.37$, excluding the transition region. The pseudorapidity coverage is smaller than that for electrons due to the higher granularity requirements on the calorimeters needed to suppress photons originating from neutral-pion decays, $\pi^0 \to \gamma\gamma$ [85].

Jets are considered in CRs. Using particle-flow objects [111], jet candidates must pass a minimum transverse-momentum threshold of $p_{\mathrm{T}} > 20\,\mathrm{GeV}$ and have an absolute rapidity of $|y| < 4.4$.

The reconstruction algorithms for different physics objects (e. g., electrons, muons, jets) are independent of each other. Thus, multiple physics objects can be reconstructed from the same hits or clusters. To prevent double-counting, objects that are too close to each other in ΔR space are removed. This step is referred to as *overlap removal*. Only candidates that

pass the previously mentioned requirements are considered in the overlap removal. For each event, physics objects are removed in the following order:

1. remove jets overlapping with photons within $\Delta R < 0.4$
2. remove jets overlapping with electrons within $\Delta R < 0.2$
3. remove photons overlapping with electrons within $\Delta R < 0.4$
4. remove photons overlapping with muons within $\Delta R < 0.4$
5. remove electrons overlapping with muons within $\Delta R < 0.2$

This order prefers lepton and photon candidates over jet candidates, lepton candidates over photon candidates, and muon candidates over electron candidates. It reflects the interest in the final-state particles and favors physics objects with more reliable reconstruction algorithms.

The physics objects that survive the overlap removal are used for the selection requirements of the SR and CRs. There are no explicit requirements on the presence or absence of additional physics objects. In the following, we will describe the selection criteria of the SR in detail. The CRs will be defined when needed, and the differences relative to the SR will be highlighted. An overview of the baseline selection is presented in Table A.6.

4.2.2 Signal selection

The events in the SR of the $ZZ\gamma$ analysis must contain at least four leptons and one photon—the final-state particles. Since the four leptons originate from Z-boson decays, two pairs of OSSF lepton pairs are required. In cases where there are more than two potential pairs or an inherent pairing ambiguity (e. g., four electrons or four muons), the two pairs whose dilepton invariant mass, $m_{\ell\ell,1}$ and $m_{\ell\ell,2}$, closest to the Z-boson mass, $m_Z = 91.1876 \pm 0.0021\,\text{GeV}$ [112], are selected, minimizing $(|m_{\ell\ell,1} - m_Z| + |m_{\ell\ell,2} - m_Z|)$. To remove low-mass resonances (i. e. J/ψ) and optimize the signal-to-background ratio (see Appendix B.1), a minimum dilepton invariant mass requirement of $m_{\ell\ell} > 40\,\text{GeV}$ is applied afterwards.

The four selected leptons are ordered by transverse momentum. The leading and sub-leading lepton must have transverse momenta exceeding

$p_{\mathrm{T}}^{\ell} > 30\,\mathrm{GeV}$ and $p_{\mathrm{T}}^{\ell} > 25\,\mathrm{GeV}$, respectively. Due to the Z-boson mass of around $m_Z \sim 90\,\mathrm{GeV}$, the leptons are expected to carry a substantial amount of momentum. In a Z-boson decay at rest, both leptons should have a momentum of around $p^{\ell} \sim 45\,\mathrm{GeV}$. However, in the experimental setting of the ATLAS detector at the LHC, a Z-boson decay at rest is not guaranteed, and through radiation or measurement uncertainties, a broader momentum distribution is observed. Depending on the decay, a considerable portion of the momenta is in the transverse plane. The transverse-momentum thresholds ensure fully efficient triggering.

If one of the selected leptons is an electron, the medium identification WP and loose isolation WP [73] (see Appendix A.2) are imposed. This reduces the number of misidentified electrons and increases the purity of the selected electrons.

If one of the selected leptons is a muon, the PflowLoose isolation WP (see Appendix A.2.2) and a d_0 significance below $|d_0|/\sigma_{d_0} < 3$ [74] must be satisfied. This ensures that muons originate from the hard interaction and not from heavy-flavor decays.

The photon candidate with the highest transverse momentum is selected. For an improved signal significance, a transverse momentum of $p_{\mathrm{T}}^{\gamma} > 20\,\mathrm{GeV}$ is required (see Appendix B.1). To reduce the background contribution from non-prompt photons coming from hadron decays, the photon must pass the tight identification WP and the loose isolation WP [85] (see Appendix A.2).

4.2.3 Final state radiation rejection

So far, the signal selection has targeted prompt leptons coming from a ZZ decay. The requirements on the selected photon suppress the contribution from non-prompt photons within jets but barely affect FSR photons. Because we want to suppress FSR events, we remove them from the signal selection with a dedicated rejection criterion:

$$(m_{\ell\ell\gamma} + m_{\ell\ell}) > 2 \cdot m_Z. \tag{4.1}$$

The requirement that the three-body invariant mass of two leptons and the photon, $m_{\ell\ell\gamma}$, plus the two-body invariant mass of the same two lep-

tons, $m_{\ell\ell}$, must be larger than twice the Z-boson mass, m_Z, results in the rejection of FSR events.

In case of an FSR photon radiating off one of the leptons from the Z-boson decay, this decay is no longer a two-body decay, but a three-body decay. Due to the missing energy of the radiated photon, the dilepton invariant mass is expected to be below the Z-boson mass. However, the three-body invariant mass of the two leptons and the photon should reflect the Z-boson invariant mass. This property provides discriminating power needed to reject FSR events in the signal selection.

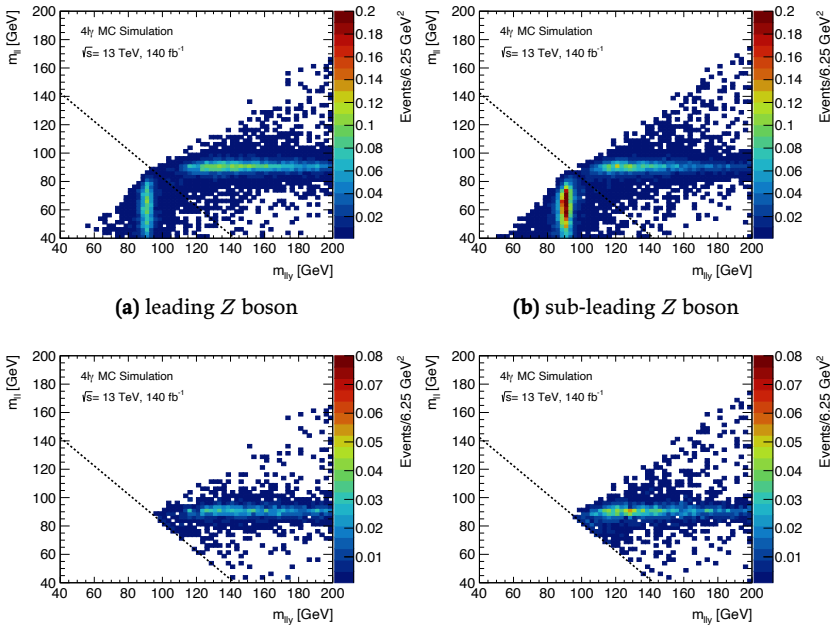
In Fig. 4.2, the 2D distributions of the three-body invariant mass of two leptons plus photon, $m_{\ell\ell\gamma}$, versus the dilepton invariant mass of the same two leptons, $m_{\ell\ell}$, are presented. From the main signal sample—an inclusive production of the $4\ell\gamma$ final state with FSR and signal events but without the Higgs contribution—all events passing the above-mentioned selection criteria, not including the FSR rejection criterion, are shown in the upper two distributions of Fig. 4.2. The number of events is scaled to the full Run 2 integrated luminosity of 140 fb^{-1}.

Both upper distributions have accumulations of events in two regions: a vertical band around 90 GeV on the x-axis, and a horizontal band around 90 GeV on the y-axis. The vertical band shows an accumulation of FSR events. As expected, the three-body invariant mass of the two leptons plus photon is centered around 90 GeV, the invariant mass of the Z boson. The dilepton invariant mass of these events shows a broad distribution around 65 GeV, roughly the difference between the minimum transverse momentum of the photon and the Z-boson mass.

The horizontal band shows the accumulation of events without photon radiation from one of the leptons from the Z-boson decay. Here, the dilepton invariant mass is centered around 90 GeV, and the three-body invariant mass is mainly distributed between 120 GeV and 160 GeV.

A striking feature of the two figures is the larger contribution of FSR events in the distribution of the sub-leading Z boson. Due to the radiation of a photon, the reconstructed energy and momentum of the Z boson through its decay leptons is underestimated and results in lower values.

Since the FSR events can clearly be distinguished in the distributions shown in Fig. 4.2, the three-body invariant mass and two-body invariant



(a) leading Z boson

(b) sub-leading Z boson

(c) leading Z boson

(d) sub-leading Z boson

Figure 4.2: The 2D distributions of the three-body invariant mass of two leptons plus photon, $m_{\ell\ell\gamma}$, versus the dilepton invariant mass of the same two leptons, $m_{\ell\ell}$, for the $pp \rightarrow 4\ell\gamma$ signal MC simulation sample. Top: The distributions of the leptons from the leading and sub-leading Z boson before the FSR rejection are shown in (a) and (b), respectively. The FSR events are accumulated in the band around the Z-boson mass on the x-axis, while decays without photon radiation are centered in the band around the Z-boson mass on the y-axis. Bottom: The same two distributions for the leading and sub-leading Z boson are shown after the FSR rejection in (c) and (d), respectively. The diagonal line visualizes the FSR rejection criterion, $(m_{\ell\ell\gamma} + m_{\ell\ell}) > 2 \cdot m_Z$.

mass are used to apply the rejection criterion on the FSR events, $(m_{\ell\ell\gamma} + m_{\ell\ell}) > 2 \cdot m_Z$. The requirement results in a rejection of all events in the lower-left region. The lower two distributions in Fig. 4.2 show the 2D distribution of all events passing the FSR rejection.

The rejection criterion is applied to the leptons of the leading and sub-leading Z boson separately to account for FSR of all selected leptons. This means that events in the horizontal band in one distribution (e. g., leading Z boson) might have an FSR photon in the decay of the other Z boson, thus lying in the vertical band of that distribution (e. g., sub-leading Z boson) and are rejected by the requirement in Eq. (4.1). This results in a significant reduction of events, approximately $\frac{2}{3}$ of the events.

4.2.4 Pairing

While the FSR rejection criterion efficiently rejects correctly paired FSR events, the minimization algorithm selecting the two OSSF lepton pairs might fail in the case of an FSR event due to the momentum carried by the photon. After selecting the two best lepton pairs $(m_{\ell\ell,1}, m_{\ell\ell,2})$ with the minimization algorithm, an additional algorithm corrects the pairing if a different lepton combination $(m'_{\ell\ell,i}, m'_{\ell\ell,j})$ with an FSR photon is more suitable, minimizing:

$$\min\left(|m'_{\ell\ell,i} - m_Z| + |m'_{\ell\ell\gamma,j} - m_Z|, |m_{\ell\ell,1} - m_Z| + |m_{\ell\ell,2} - m_Z|\right), \quad (4.2)$$

where i, j represent all exclusive potential OSSF lepton pairs in the event. This minimization process selects a different lepton combination if the differences to the Z-boson mass of the dilepton invariant mass of the one pair, $m'_{\ell\ell,i}$, and the three-body invariant mass of the photon and the leptons from another pair, $m'_{\ell\ell\gamma,j}$, are smaller than the differences to the Z-boson mass of the previously chosen pairs $(m_{\ell\ell,1}, m_{\ell\ell,2})$. All events for which the pairing is changed through this minimization process are FSR events and are subsequently rejected by the FSR rejection criterion. The effect of this improved algorithm is studied in more detail in the following.

After applying the full signal selection, including the FSR rejection but without the improved minimization algorithm, we can cross-check whether we paired the leptons correctly in events with four electrons or four muons

in the final state. These events have an inherent pairing ambiguity, and we can invert the pairing:

$$Z_1 : \ell_1^+\ell_2^-, Z_2 : \ell_3^+\ell_4^- \xrightarrow[\text{pairing}]{\text{invert}} Z_1' : \ell_1^+\ell_4^-, Z_2' : \ell_3^+\ell_2^- \tag{4.3}$$

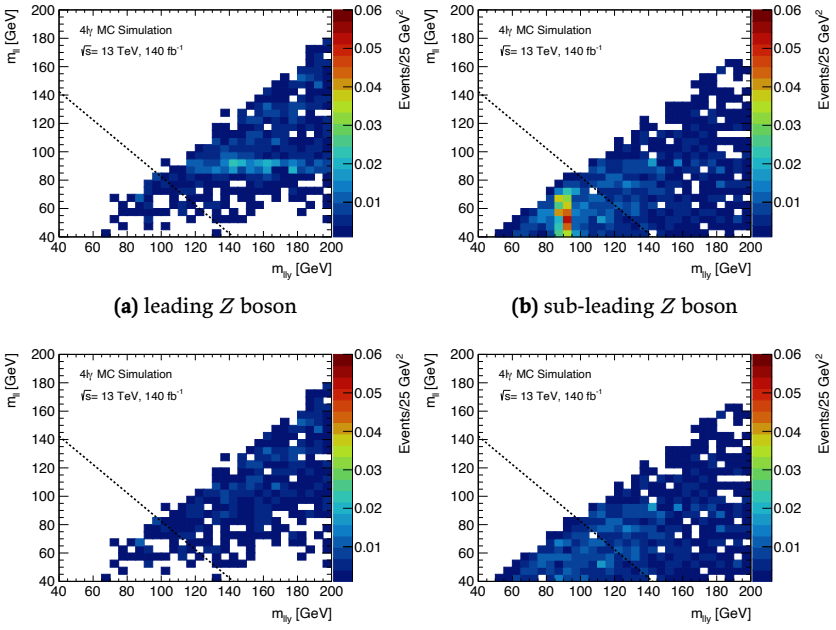
If all events have been paired correctly, invariant mass distributions of the inverted pairs should be relatively homogeneous and have no distinct features. However, when we consider the same 2D distributions as for the FSR rejection with inverted pairing, see Fig. 4.3, structures are evident.

Focusing on Fig. 4.3a, we can see an accumulation of events around the Z-boson mass on the y-axis. This indicates that the inverted pairing appears correct since the dilepton invariant mass is very close to the Z-boson mass. The goal of the minimization algorithm is to select this combination, so why did it fail? In Fig. 4.3b, an accumulation of events with an FSR photon from the sub-leading Z-boson decay is visible. Combining these two observations, the algorithm seems to fail in the case of an FSR event.

This can be explained by the transverse momentum and energy carried by the photon, which are missing from reconstructed invariant mass. In certain events, the invariant mass contribution of the photon is large enough to result in a significant difference of the dilepton invariant mass from the Z-boson mass. In such a case, a different lepton pairing might result in a smaller difference to the Z-boson mass.

We can now study the effect of the improved algorithm on the inverted lepton pairs for the $4e$ and 4μ events. The lower two distributions in Fig. 4.3 show the 2D distributions for the inverted pairs after applying the improved selection algorithm. No structure or accumulation of events is observed. The relatively homogeneous distribution of events indicates that the refined algorithm selects the correct decay products even when photon radiation occurs off one of the leptons.

The improved selection algorithm is always applied whenever there is at least one Z boson and a photon in the selection region. A summary of the selection criteria applied to all events in the SR is given in Table 4.1.



(a) leading Z boson

(b) sub-leading Z boson

(c) leading Z boson

(d) sub-leading Z boson

Figure 4.3: The 2D distributions of the three-body invariant mass of two leptons plus photon, $m_{\ell\ell\gamma}$, versus the dilepton invariant mass of the same two leptons, $m_{\ell\ell}$, for $4e$ or 4μ events of the $pp \rightarrow 4\ell\gamma$ signal MC simulation sample. The pairing of the minimization algorithm is inverted. Top: The inverted lepton pair of the leading and sub-leading Z boson after the full event selection, including the FSR rejection, is shown in (a) and (b), respectively. Bottom: The same 2D distributions are shown after the implementation of the refined algorithm for the leading and sub-leading Z boson in (c) and (d), respectively. The diagonal line visualizes the FSR rejection criterion, $(m_{\ell\ell\gamma} + m_{\ell\ell}) > 2 \cdot m_Z$.

Table 4.1: Overview of the event selection in the SR.

	Electrons	Muons	Photon
Kinematics	$p_{\mathrm{T}} > 30, 25, 10, 10\,\mathrm{GeV}$		$p_{\mathrm{T}} > 20\,\mathrm{GeV}$
	$\lvert\eta\rvert < 2.47$	$\lvert\eta\rvert < 2.5$	$\lvert\eta\rvert < 2.37$
excluded	$1.37 < \lvert\eta\rvert < 1.52$		$1.37 < \lvert\eta\rvert < 1.52$
Isolation	Loose	PflowLoose	Loose
	$\Delta R(\mu, e) > 0.2$		$\Delta R(\ell, \gamma) > 0.4$
Identification	Medium	Medium	Tight
$d0$ significance	< 5	< 3	
Multiplicity	≥ 2 OSSF pairs		≥ 1 photon
Invariant mass	$\min(\lvert m_{\ell\ell,1} - m_Z\rvert + \lvert m_{\ell\ell,2} - m_Z\rvert)^*$, $m_{\ell\ell} > 40\,\mathrm{GeV}$, $(m_{\ell\ell\gamma} + m_{\ell\ell}) > 2 \cdot m_Z$		
Trigger	Single and dilepton trigger		

*improved pairing algorithm

4.2.5 Fiducial region

Similar to the SR, a *fiducial region (FR)* at particle level is defined. In this region, independent of detector effects, the cross-section measurement is performed. The fiducial selection is as similar as possible to the signal selection at the reconstruction level to reduce model dependence, but does not need to account for special detector requirements.

For the selection of the FR at particle level, only photons and leptons that do not originate from hadron decays within jets are considered.

To correct for lepton energy losses due to radiation, the energy of all photons within $\Delta R < 0.1$ of the lepton is summed and added to the lepton. All photons within $\Delta R < 0.4$ of a lepton are discarded. A harmonized pseudorapidity requirement of $|\eta| < 2.5$ is applied to both electrons and muons. The transition region is not excluded. The four signal leptons are selected using the same refined pairing algorithm as in the definition of the SR, a minimum dilepton invariant mass of 40 GeV is required, and the transverse-momentum requirements of the SR must be satisfied. No isolation or identification requirements are imposed on the leptons.

Table 4.2: Overview of the fiducial selection.

	Electrons	Muons	Photon
Kinematics	$p_{\mathrm{T}} > 30, 25, 10, 10\,\mathrm{GeV}$		$p_{\mathrm{T}} > 20\,\mathrm{GeV}$
	$\lvert\eta\rvert < 2.5$	$\lvert\eta\rvert < 2.5$	$\lvert\eta\rvert < 2.37$
Isolation			$E_T^{cone20}/E_T^{\gamma} < 0.07$
			$\Delta R(\ell, \gamma) > 0.4$
Multiplicity	≥ 2 OSSF pairs		≥ 1 photon
Invariant mass	$\min(\lvert m_{\ell\ell,1} - m_Z\rvert + \lvert m_{\ell\ell,2} - m_Z\rvert)^*$, $m_{\ell\ell} > 40\,\mathrm{GeV}$, $(m_{\ell\ell\gamma} + m_{\ell\ell}) > 2 \cdot m_Z$		

*improved pairing algorithm

The highest-energy photon is selected and must pass the pseudorapidity condition $|\eta| < 2.37$ and be isolated. Since all isolation WPs depend on detector parameters, the photon isolation at the particle level is defined through the *isolation cone sum*. This sum is the transverse-momentum sum of all stable particles (traveling more than approximately 10 mm before decaying), except neutrinos and muons, within a cone of radius $\Delta R = 0.2$ around the photon. This isolation cone sum must be less than 7% of the photon's own transverse momentum for the photon to be considered isolated. The relative fraction of transverse momentum in the cone was optimized in the ATLAS $Z\gamma$ analysis [113].

The FSR rejection is also applied to events at particle level. An overview of all selection criteria applied to electrons, muons, and photons in the FR is presented in Table 4.2.

4.3 Signal expectation

The signal contribution consists of the direct $ZZ\gamma$ production and the Higgs contribution. Both production channels can be modeled using MC event generators, which are used as a basis for studying kinematic distributions, event characteristics, and the number of expected signal events.

The direct production is simulated using the SHERPA 2.2.11 $pp \rightarrow$

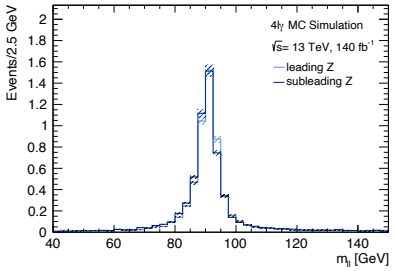
$\ell^+\ell^-\ell'^+\ell'^-\gamma$ MC event-generator sample [95], also referred to as the $4\ell\gamma$ sample. The matrix element with zero jets in the final state is calculated at NLO and with up to two jets at LO. The NNPDF 3.0 NNLO PDF sets are used [114]. This calculation is merged with the SHERPA parton shower algorithm [115] following the CKKW procedure [116]. Since this sample represents the inclusive production of four leptons and one photon, FSR events are included.

Due to the higher-order, loop-suppressed Higgs-boson decay to a Z boson and a photon, the Higgs contribution is not included in the $4\ell\gamma$ sample. An additional sample simulating this process is generated: the POWHEGPYTHIA8 $pp \to ZH \to ZZ\gamma$ sample, referred to as the $ZH \to ZZ\gamma$ sample. The matrix element is calculated using POWHEGBOX [117–119] and includes Higgs radiation off the Z boson and the explicit decay of the Higgs boson into a Z boson and a photon. The CTEQ6 LO PDF sets are used [120]. All Z-boson decays are simulated, reducing the statistics of the simulated events in the $\ell^+\ell^-\ell'^+\ell'^-\gamma$ final state. The parton shower is simulated using PYTHIA8 [121]. Due to the small total width of the Higgs boson [122], the interference contribution between direct production and the Higgs contribution is assumed to be negligible.

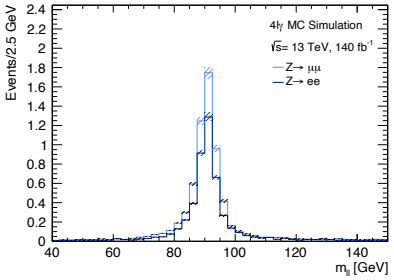
To analyze the signal contribution and its distributions, we require all events in the aforementioned signal samples to pass the requirements of the SR. This leads to a signal expectation of 7.04 ± 0.20 events for Run 2. Events with a Z-boson decay into tau leptons that pass the signal selection are included in the signal expectation ($Z \to \tau^+\tau^-$ contribution: 0.036 ± 0.007). The separation into different signal samples and decay channels of the final state ($4e$, $2e2\mu$ and 4μ), as well as their combinations, are shown in Table 4.3. Total uncertainties are given. Individual uncertainty components and their contributions to the signal samples will be described in Section 4.3.1.

Furthermore, we can study the distributions of different kinematic properties, such as the dilepton invariant mass or the transverse momentum of final-state particles, Fig. 4.4. All distributions represent selected events from the $4\ell\gamma$ signal sample in the SR. The same distributions for the $ZH \to ZZ\gamma$ signal sample are shown in Appendix B.2.

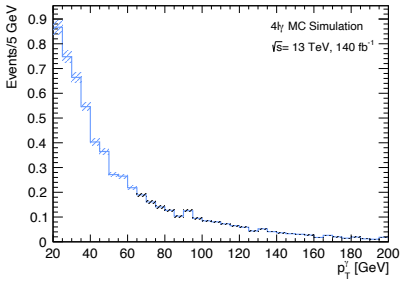
In Fig. 4.4a, the dilepton invariant mass distribution for the leading and sub-leading Z boson is shown. Differences between distributions are



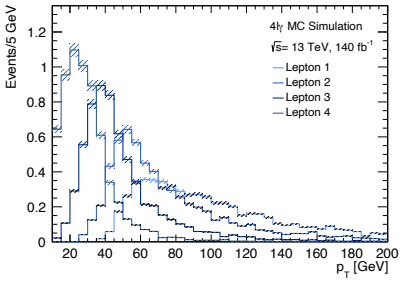
(a) dilepton invariant mass, Z_1 and Z_2



(b) dilepton invariant mass, m_{ee} and $m_{\mu\mu}$



(c) photon transverse momentum



(d) lepton transverse momentum

Figure 4.4: Top: The invariant mass distributions of the two leptons from the leading and sub-leading Z bosons (a) and the dilepton invariant mass of electron- and muon-pairs (b). Bottom: The kinematic distributions of the transverse momentum of the photon (c) and the transverse-momentum distribution of the leading, sub-leading, third-leading and fourth-leading leptons (d). All distributions show events simulated with the $4\ell\gamma$ signal sample that pass the SR selection criteria. Total uncertainties are shown as shaded bands, and the events are scaled to the Run 2 luminosity.

Table 4.3: Summary of the signal contributions for the different channels ($4e$, $2e2\mu$, and 4μ) and their combination (4ℓ). Total uncertainties are shown.

	$4e$	$2e2\mu$	4μ	4ℓ
$4\ell\gamma$	1.13 ± 0.09	3.04 ± 0.11	2.11 ± 0.07	6.28 ± 0.20
$ZH \to ZZ\gamma$	0.12 ± 0.02	0.38 ± 0.04	0.26 ± 0.02	0.76 ± 0.04
Signal	1.25 ± 0.09	3.42 ± 0.12	2.37 ± 0.07	7.04 ± 0.20

very minor. The invariant mass distribution of the sub-leading Z boson is shifted slightly to lower invariant masses, as expected from its definition; the width of the two distributions is approximately the same. Both Z bosons are mainly produced on-shell since the distributions show a clear peak around the Z-boson mass. Additionally, no significant remnants of FSR events are visible; these would appear as a broad distribution centered around $m_{\ell\ell} \sim 60\,\text{GeV}$.

The comparison between di-electron and di-muon invariant mass distributions is displayed in Fig. 4.4b. Both distributions agree with the invariant mass distributions of decay products from an on-shell Z boson. While the branching ratios for Z-boson decays into electrons and muons are the same [112], more muon pairs are selected. This preference results from the differences in reconstruction efficiency and pseudorapidity acceptance.

The transverse-momentum distribution of the photon (Fig. 4.4c) is a falling distribution. It can be clearly seen that the transverse-momentum threshold of $p_{\text{T}}^{\gamma} > 20\,\text{GeV}$ has a significant impact on the selected number of signal events. The increase in photons with low transverse momenta is a direct result of photon production through bremsstrahlung.

The comparison between the transverse momentum of the four selected signal leptons is shown in Fig. 4.4d. Leptons are ordered by their transverse momentum and labeled as *lepton 1* (leading), *lepton 2* (sub-leading), *lepton 3*, and *lepton 4*. The mean of the transverse-momentum distribution shifts to smaller values from lepton 1 to lepton 4; while this directly results from the ordering of the leptons, one can also observe that the width of the distributions decrease because the available phase space is reduced.

4.3.1 Signal uncertainties

The total uncertainties stated in Table 4.3 consist of a statistical uncertainty contribution (stat.), experimental uncertainties arising from the measurement and reconstruction of the final-state particles in the detector (exp.), and theoretical uncertainties from the limited theory knowledge (theo.). Split into their different uncertainty contributions, we can write the signal contributions as follows:

$$4\ell\gamma : N_{sig} = 6.28 \pm 0.09\ (\text{stat.}) \pm 0.16\ (\text{exp.}) \pm 0.09\ (\text{theo.})$$
$$ZH \to ZZ\gamma : N_{sig} = 0.76 \pm 0.03\ (\text{stat.}) \pm 0.03\ (\text{exp.}) \pm 0.01\ (\text{theo.}).$$

Statistical uncertainties

The statistical uncertainty arises from the finite number of simulated events in the MC simulation samples. In a weighted MC simulation sample, the statistical uncertainty of each selected event is $\sqrt{w_{\text{sel}}^2}$. For a sample of events—events are independent of each other and thus uncorrelated—the total statistical uncertainty is the sum of all selected events, $\sqrt{\sum w_{\text{sel}}^2}$ [123, 124].

Experimental uncertainties

The experimental uncertainties account for: uncertainties in calibration and measurement efficiencies during the reconstruction of the final-state particles; the uncertainty in the luminosity measurement; and the variations arising from the pileup reweighting—the overlaying of additional pp events in simulation. All these systematic uncertainties are centrally provided by ATLAS. The determination of the luminosity uncertainty is presented in Ref. [125] and corresponds to 0.83%. The $\pm 1\sigma$ variations of all other experimental uncertainties are propagated through the analysis, and the difference between the resulting event yield and the nominal value is taken as the uncertainty. The different sources and their relative contribution to the signal samples are presented in Table 4.4.

The electron reconstruction, identification, isolation, and trigger efficiency uncertainties are propagated via scale factors. Scale factors represent the relative difference between the efficiency measurements in data and MC

Table 4.4: Relative values of the different experimental uncertainties for the two signal samples. In the case of asymmetric uncertainties, the larger one is used and symmetrized. Uncertainties contributing less than 0.1% are not listed.

Source	Relative uncertainty [%]	
	$4\ell\gamma$	$ZH \to ZZ\gamma$
Electron identification efficiency	0.54	0.48
Electron reconstruction efficiency	0.17	0.18
Photon identification efficiency	1.23	1.37
Photon isolation efficiency	1.01	1.02
Electron-photon energy resolution	0.37	0.24
Electron-photon energy scale	0.37	0.21
Muon isolation efficiency	0.56	0.61
Muon reconstruction efficiency	0.49	0.43
Muon momentum resolution	0.29	0.22
Muon momentum scale	0.32	0.29
Pileup reweighting	1.35	3.21
Luminosity	0.83	0.83
Total experimental uncertainty	2.53	3.87

event simulations. Each of the electron efficiencies is determined through tag-and-probe methods or template fits in data and MC event simulations. The systematic uncertainties in the efficiencies are estimated, for example, by varying the selection criteria, changing the template or fit function, or varying the normalization of different contributions (e. g., signal, background) [73, 126].

The photon reconstruction, identification, and isolation efficiencies also have uncertainties, which are propagated through scale factors. The photon efficiencies are measured separately for converted and unconverted photons. In the low-p_{T} region, photons are mainly selected from $Z \to \ell\ell\gamma$ decays, and the efficiencies are estimated with a template fit. Alternatively, the efficiencies are estimated with a matrix method using photons from an inclusive photon sample, triggered by one of the single-photon trig-

gers, or by extrapolating from the electron efficiency after adjusting the shower-shape variables. Efficiency uncertainties arise mainly from MC event generator modeling uncertainties or non-closure uncertainties [82, 85, 127].

Electrons and photons are reconstructed from energy deposits in the calorimeters, resulting in a combined energy resolution and scale uncertainty. After the energy calibration, their scale and resolution are determined from the invariant mass of $Z \to e^+e^-$ decays. The uncertainties are propagated from material and calibration uncertainties, as well as estimated via variations of the $Z \to e^+e^-$ event selection [83].

The muon reconstruction, identification, isolation, and trigger efficiencies are determined via tag-and-probe and template fit methods in data and simulation. The systematic uncertainties in the efficiencies arise mainly from the applied methods (e. g., template shape, background fit, matching procedure) [74, 109].

The muon momentum resolution and scale are estimated via $Z \to \mu^+\mu^-$ and $J/\Psi \to \mu^+\mu^-$ decays. Muon momentum scale corrections are needed because of detector misalignment and are derived from a fit to simulated samples with ideal detector alignment. The dominant uncertainties are determined by varying the event-selection criteria and the fitting procedure. The resolution is only corrected in simulation by matching it to data [128].

Theoretical uncertainties

The limited knowledge of PDFs and the strong coupling constant α_s, as well as the missing higher-order terms in the matrix-element calculation at fixed order in perturbation theory, lead to the dominant sources of theoretical uncertainties.

The PDFs used in event generators are determined through a global fit to data. Various PDF sets from different groups contain variations in their central values and uncertainties, e. g., Refs. [92, 114, 120, 129, 130]. These differences can come from the experimental data considered in the fit or the underlying model assumptions.

The value of α_s is also experimentally determined. Due to the running

coupling, α_s depends on the momentum scale. It is most precisely measured at the Z-boson mass, $\alpha_s(m_Z) = 0.1179 \pm 0.0010$ [112], and its value at different energy scales is extrapolated from $\alpha_s(m_Z)$. Furthermore, α_s is one of the parameters in the PDF fits.

By varying the used PDF sets and the value of α_s within its uncertainty as input to the PDF fit, the difference from the nominal cross-section is taken as the corresponding theoretical uncertainty. These uncertainties are treated as uncorrelated and can be added in quadrature [131].

The factorization of the hard interaction cross-section calculation into long-distance non-perturbative physics described by the PDFs and short-distance perturbative physics calculated by the matrix-element integration requires a scale to differentiate between these two regimes. This scale is called the factorization scale μ_F [90, 132].

Due to large loop momenta, the matrix-element calculation can result in divergences. To keep the matrix element finite, a cut-off at a certain momentum scale needs to be introduced—the renormalization scale μ_R [3].

The matrix-element calculation at fixed order in perturbation theory has missing higher-order corrections. The uncertainties in the matrix-element calculation depend on these missing higher-order corrections, which are estimated by variations of the scale parameters μ_F and μ_R [133, 134].

The theoretical uncertainties in the PDFs and α_s from the PDF set variations and the uncertainties in the matrix element from the scale variations are presented in Table 4.5.

Table 4.5: Relative theoretical uncertainty of the two signal samples.

Source	Relative uncertainty [%]	
	$4\ell\gamma$	$ZH \to ZZ\gamma$
PDF and α_s	± 1.30	± 1.08
Scale variations	$^{+0.63}_{-0.10}$	$^{+1.80}_{-0.50}$
Total theoretical uncertainty	$^{+1.45}_{-1.30}$	$^{+2.10}_{-1.19}$

4.3.2 Correction factor

To translate the cross-section measurement from reconstruction level to particle level, a so-called *correction factor* C is needed. The fiducial cross-section at particle level is defined as

$$\sigma^{\text{fid}}_{pp\to 4\ell\gamma} = \frac{N_{\text{sig}}}{C \cdot \mathcal{L}}, \tag{4.4}$$

with the number of selected signal events N_{sig} in the SR. The correction factor C corrects for reconstruction inefficiencies, limited detector resolution, and acceptance differences. The factor is defined as the ratio of simulated reconstructed signal events in the SR, $N^{\text{SR}}_{\text{MC}}$, to simulated signal events at particle level passing the FR selection requirements, $N^{\text{FR}}_{\text{MC}}$. The correction factor is unique to each MC simulation sample but similar for the same process. The values for the $4\ell\gamma$ and $ZH \to ZZ\gamma$ signal samples are $C \approx 0.35$, and they are shown in Table 4.6.

Table 4.6: The number of simulated signal events passing the selection criteria of the FR at particle level, $N^{\text{FR}}_{\text{MC}}$, the number of simulated signal events passing the selection criteria of the SR at reconstruction level, $N^{\text{SR}}_{\text{MC}}$, and the correction factor, C, for the $4\ell\gamma$ and $ZH \to ZZ\gamma$ signal samples are listed. Only the statistical uncertainties are given.

	$4\ell\gamma$ sample	$ZH \to ZZ\gamma$ sample	Combined
$N^{\text{FR}}_{\text{MC}}$	17.95 ± 0.14	2.03 ± 0.05	19.98 ± 0.15
$N^{\text{SR}}_{\text{MC}}$	6.28 ± 0.09	0.76 ± 0.03	7.04 ± 0.09
C [%]	34.99 ± 0.38	37.44 ± 1.30	35.24 ± 0.36

Chapter 5

Background estimation

The definition of the SR has been optimized to minimize the background contribution. However, a remaining contribution is present and must be estimated.

The dominant background contribution comes from ZZ events with additional non-prompt photons. Non-prompt photons are defined as all photons produced within the parton shower and that do not originate from the hard interaction, ISR, or FSR. The estimation of this background contribution is described in detail in Section 5.1.

Another background present in the SR consists of events with one or more misidentified leptons. Misidentified leptons are primarily jets reconstructed as leptons, but also non-prompt leptons from hadron decays. The estimation of events with misidentified leptons is detailed in Section 5.2.

A small combinatorial background arising from ZZ and single-photon events that originate from two different simultaneous pp interactions is defined as pileup background and is described in Section 5.3.

Additional background contributions are present, such as $pp \to ZH \to \ell\ell\mu\mu$ plus an FSR photon, or combinatorial background from double-parton scattering. Their contributions have been estimated to be less than 1% of the signal yield; consequently, they are considered negligible and are not discussed further.

5.1 Non-prompt photons

Non-prompt—also called *fake*—photons are mainly produced within jets. In their hadronization process, neutral mesons such as π^0 are produced. The π^0 decays into two photons, which can be very collinear and be de-

tected as one single high-energy photon. A characteristic difference to promptly produced photons is the hadronic activity surrounding them. Thus, isolation requirements on the photon reduce the non-prompt photon background contribution significantly, but not completely. The remaining fraction needs to be estimated. Since this background is dominant, a precise estimation with a small uncertainty is crucial for a high signal significance.

The simulation of the non-prompt photon characteristics and kinematic distributions is not modeled sufficiently well in MC event generators for a simulation-based analysis. Data are needed for a reliable estimate.

The direct application of data-driven methods, e. g., template fit, 2D sideband method, or matrix method [34], is not feasible due to the low-event-count in CRs close to the SR. Therefore, a different approach, referred to as the *ratio method*, is applied. The underlying idea is that the fraction of jets misidentified as non-prompt photons is generally independent of the number of Z bosons in the event. With this approximation, the following relation holds:

$$\frac{N_{ZZ\gamma}^{\gamma_{\text{fake}}}}{N_{ZZ}^{\text{jet}}} = \frac{N_{Z\gamma}^{\gamma_{\text{fake}}}}{N_{Z}^{\text{jet}}}. \tag{5.1}$$

The number of events with a non-prompt photon in the SR is defined as $N_{ZZ\gamma}^{\gamma_{\text{fake}}}$. While $N_{Z\gamma}^{\gamma_{\text{fake}}}$ is the number of $Z\gamma$ events with a non-prompt photon, N_{Z}^{jet} and N_{ZZ}^{jet} are the number of events with at least one jet and one or two Z bosons, respectively. An exemplary conceptual representation of Eq. (5.1) is presented in Fig. 5.1.

The relation in Eq. (5.1) contains some implicit assumptions, such as that the jets in ZZ+jet and Z+jet events have the same characteristics and thus, the same probability to produce a non-prompt photon. This is studied in more detail in Section 5.1.2, and appropriate systematic uncertainties are determined.

The non-prompt-photon and jet kinematic properties might differ. To minimize their differences, the phase-space requirements on the two objects have been harmonized as much as possible. Similar to the photon, we require at least one jet in each ZZ+jet and Z+jet event. With a large fraction of the jet's transverse momentum is in a photon-like cluster, the

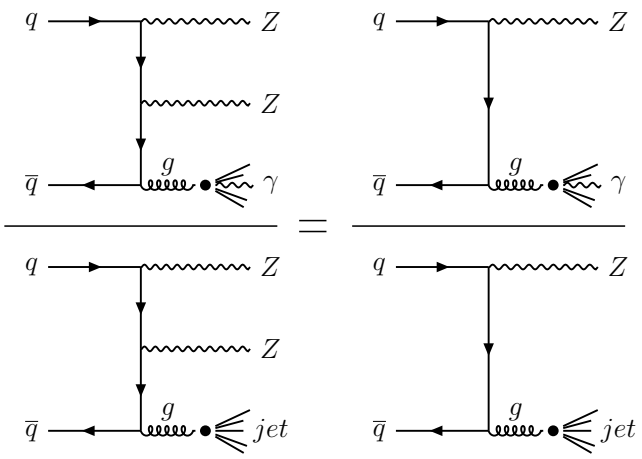


Figure 5.1: Conceptual representation of Eq. (5.1). For simplicity, only one set of diagrams is shown. All antiquarks radiating off a gluon can be exchanged with a gluon radiating off a quark.

jet must pass the same transverse-momentum requirement as the photon, $p_{\mathrm{T}} > 20\,\mathrm{GeV}$. Because jets have a broader structure, the pseudorapidity requirement is relaxed, accepting jets within $|\eta| < 2.6$ and imposing no rejection of jets in the transition region.

No FSR rejection is applied to the ZZ+jet and Z+jet events. The selection criteria of single-Z-boson events satisfy the same requirements as the leading Z boson in ZZ events.

With the ansatz in Eq. (5.1), we define the number of events with non-prompt photons in the SR as:

$$N_{ZZ\gamma}^{\gamma_{\text{fake}}} = N_{Z\gamma}^{\gamma_{\text{fake}}} \frac{N_{ZZ}^{\text{jets}}}{N_{Z}^{\text{jets}}}. \tag{5.2}$$

Thus, the number of events with a non-prompt photon in the SR is the product of the number of $Z\gamma$ events with a non-prompt photon and the ratio of ZZ and Z events with at least one jet.

In the following, we first derive the number of $Z\gamma$ events with a non-prompt photon using results from the ATLAS $Z\gamma$ analysis [113]. Afterwards, the jet ratio, $\frac{N_{ZZ}^{\text{jets}}}{N_{Z}^{\text{jets}}}$, is studied in data and with MC event-generator simula-

tions. The two results are combined to derive the number of events with non-prompt photons in the SR.

5.1.1 Non-prompt photons in the $Z\gamma$ control region

The number of $Z\gamma$ events with a non-prompt photon is estimated in a $Z\gamma$ CR. This CR requires the same object- and event-selection criteria as the $ZZ\gamma$ SR except for all the requirements on the sub-leading Z boson. This means, e. g., only two leptons (instead of four) are required and a single OSSF lepton pair is needed. A full overview of all the selection criteria of the $Z\gamma$ CR is presented in Table A.7.

The ATLAS $Z\gamma$ analysis [113] derived the number of events with non-prompt photons using a 2-D sideband method [135] in data. By relaxing one or both photon-identification and isolation requirements, three distinct regions are defined. The number of non-prompt photons that satisfy the photon requirements in each of these regions is estimated in data. After subtracting other backgrounds (e. g., $t\bar{t}\gamma$, WZ, and ZZ), the number of $Z\gamma$ events with a non-prompt photon in the SR of the $Z\gamma$ analysis is extrapolated from the regions with different photon identification and isolation criteria. With the estimation of the non-prompt photon contribution, the $Z\gamma$ analysis also derived the purity as function of photon transverse momentum. The purity, P, is defined as the fraction of prompt-photon $Z\gamma$ events, $N_{Z\gamma}^{\text{prompt}}$, relative to the total of prompt-photon and non-prompt-photon $Z\gamma$ events, $N_{Z\gamma}^{\text{fake}}$, in the SR of the $Z\gamma$ analysis,

$$P = \frac{N_{Z\gamma}^{\text{prompt}}}{N_{Z\gamma}^{\text{prompt}} + N_{Z\gamma}^{\text{fake}}}. \tag{5.3}$$

This analysis requires the same isolation and identification criteria on the photon as the $Z\gamma$ analysis. The leading-Z-boson requirements are also largely harmonized with the $Z\gamma$ analysis. However, the measurement of $Z\gamma$ production was only performed with a photon-transverse-momentum threshold of $p_{\text{T}}^{\gamma} > 30\,\text{GeV}$. Thus, the non-prompt photon estimate cannot be used directly. Instead, the purity estimate is used as function of the photon's transverse momentum that has been derived for photons with $p_{\text{T}}^{\gamma} > 15\,\text{GeV}$, see Fig. 5.2. Additionally, we benefit from the measured normalization

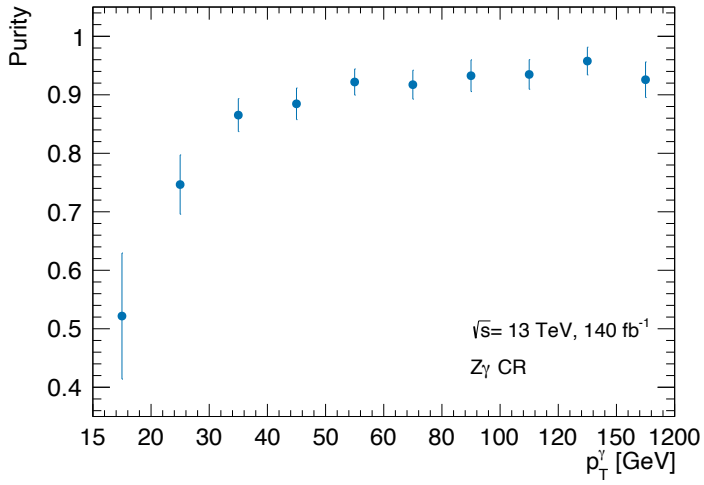


Figure 5.2: The purity P in bins of the photon transverse momentum as derived in the $Z\gamma$ analysis [113]. The purity is the ratio of prompt-photon $Z\gamma$ events and total non-prompt- and prompt-photon $Z\gamma$ events. The total uncertainties are shown; values are taken from the internal documentation of the $Z\gamma$ analysis [113].

factor on the SHERPA 2.2.4 $Z\gamma$ MC simulation sample, which normalizes the prediction to data. The kinematic distributions were found to be well-described by the $Z\gamma$ sample, provided a normalization factor of 1.23.

Purity method

The purity in Eq. (5.3) is derived for the SR of the $Z\gamma$ analysis. Since the $Z\gamma$ CR imposes the same requirements on the photon as the SR in the $Z\gamma$ analysis, no adjustments to the purity are made. An uncertainty is assigned to the non-prompt photon estimate to cover phase-space differences (e. g., trigger and lepton-selection effects).

The purity can also be expressed in terms of observed data events, N_{obs},

$$P = 1 - \frac{N_{Z\gamma}^{\text{fake}}}{N_{\text{obs}} - N_{\text{other bkg}}}, \tag{5.4}$$

where $N_{\text{other bkg}}$ denotes the number of events from all other backgrounds.

We can now select all data events passing the selection criteria of the $Z\gamma$ CR, subtract the number of events from other backgrounds, and multiply the yield by $(1 - P)$ to obtain $N_{Z\gamma}^{\text{fake}}$. Since the purity is highly dependent on the transverse momentum of the photon, the number of non-prompt-photon $Z\gamma$ events is derived differentially. The backgrounds subtracted from data are MC-estimated contributions from $t\bar{t}\gamma$, WZ, and ZZ events (see Table A.5 for details). Of the selected data events, 3.3% are identified background events, of which 2.9% arise from $t\bar{t}\gamma$, 0.3% from WZ, and 0.1% from ZZ. No pileup contribution is subtracted to account for non-prompt photons from jet production overlaid with a single-Z production.

Integrating over the transverse momentum of the photon, the nominal estimate of $Z\gamma$ events with a non-prompt photon is,

$$N_{Z\gamma}^{\gamma_{\text{fake}}} = 28370 \pm 80\ (\text{stat.})\ \pm 3860\ (\text{syst.}). \tag{5.5}$$

The statistical uncertainty is propagated from the number of observed data events. The systematic uncertainties are the propagated uncertainty in the purity (14%), the uncertainty due to phase-space differences to the $Z\gamma$ analysis (7%), and the luminosity uncertainty (1%). The relative systematic uncertainties on the MC-subtracted backgrounds are estimated to be 10–20%. However, their contribution to the non-prompt photon estimate is around 0.2% and thus, negligible.

The systematic uncertainty due to phase-space differences to the $Z\gamma$ analysis is derived with the Sherpa 2.2.4 $Z\gamma$ MC simulation sample. In Eq. (5.3), the purity is given in terms of prompt-photon $Z\gamma$ events. Deriving $N_{Z\gamma}^{\gamma_{\text{fake}}}$ via this definition should result in perfect closure if the purity has been derived in the same phase space. With the Sherpa 2.2.4 $Z\gamma$ MC simulation sample, $N_{Z\gamma}^{\text{prompt}}$ is estimated. We multiply this estimate with a factor of $(1 - P)/P$ to derive $N_{Z\gamma}^{\text{fake}}$. This results in $N_{Z\gamma}^{\gamma_{\text{fake}}} = 26500 \pm 30$ (stat.) ± 4770 (syst.). The statistical uncertainty is propagated from the MC simulation estimate of prompt-photon $Z\gamma$ events. The systematic uncertainties are from the purity (18%), the difference to the nominal estimate from data (7%), the systematic uncertainties in the MC simulation sample (2%), and the luminosity uncertainty (1%).

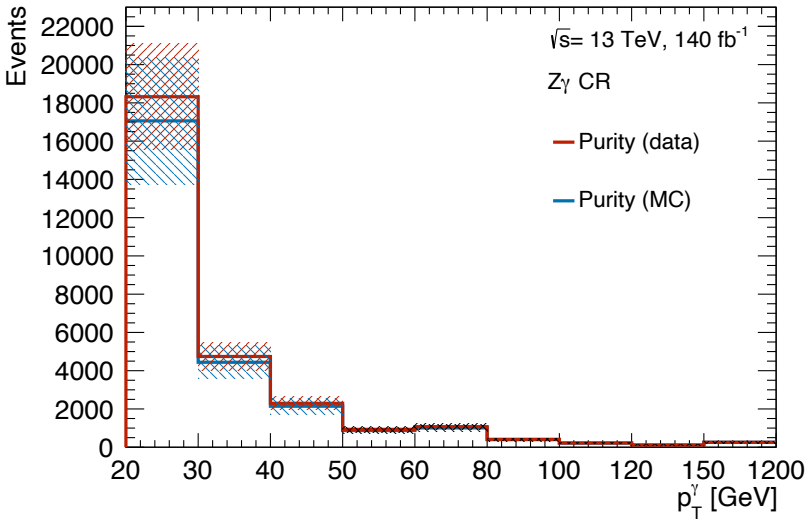


Figure 5.3: The number of $Z\gamma$ non-prompt-photon events in the $Z\gamma$ CR derived from the purity measurement in bins of the transverse momentum. The results for data as well as expected events with MC simulations are shown. The total uncertainties are indicated by the shaded regions.

The consistent results of the nominal estimate for $N_{Z\gamma}^{\text{fake}}$ and the MC-based estimate validate the use of the purity derived by the $Z\gamma$ analysis. A comparison of the two estimates as a function of photon transverse momentum is shown in Fig. 5.3. The data and MC-based estimates integrated over $p_{\text{T}}^{\gamma} > 30\,\text{GeV}$ are compared directly to the results of the $Z\gamma$ analysis. The estimates are consistent within their uncertainties. A detailed comparison is given in Appendix C.1.2.

Subtraction method

As validation of the number of $Z\gamma$ events with a non-prompt photon, another method, the *subtraction method*, is applied. This method is independent of the purity. Since we are not blinded in the $Z\gamma$ CR, we can select all data events and subtract the prompt-photon $Z\gamma$ contribution together with

pileup and the backgrounds from $t\bar{t}\gamma$, WZ, and ZZ. The remaining data events are non-prompt-photon events.

The prompt-photon $Z\gamma$ contribution is estimated with the SHERPA 2.2.4 $Z\gamma$ MC simulation sample. Since the same MC simulation has been used in the $Z\gamma$ analysis and good agreement with data has been observed when applying a normalization factor of 1.23, the estimation is reliable and a systematic uncertainty of 2.3% (taken from the $Z\gamma$ analysis) is applied.

Pileup arises from the simultaneous production of a Z boson and a photon in two different pp collisions. For the subtraction method, the pileup contribution of the $Z\gamma$ analysis is used. The contribution is extrapolated to $p_{\mathrm{T}}^{\gamma} > 20\,\mathrm{GeV}$ using the photon transverse-momentum distribution from simulated γ+jets events. The relative uncertainty in the pileup contribution is increased to 20% ($Z\gamma$ analysis: 15%) to account for the uncertainties in the extrapolation.

The contribution of $t\bar{t}\gamma$, WZ, and ZZ events is estimated with dedicated MC simulation samples. Flat systematic uncertainties of 10–20% are directly taken from the $Z\gamma$ analysis and applied accordingly.

In Fig. 5.4, the data and expected-event comparison is shown as a function of the photon's transverse momentum. The difference between data and expected events is assumed to be $N_{Z\gamma}^{\gamma\text{fake}}$. Subtracting the expected contributions (prompt-photon $Z\gamma$, pileup, $t\bar{t}\gamma$, WZ, and ZZ) from data, we derive $N_{Z\gamma}^{\gamma\text{fake}} = 28290 \pm 470\,(\text{stat.}) \pm 3590\,(\text{syst.})$.

The statistical uncertainty combines the data and simulation uncertainties. The systematic uncertainties include the propagated systematic uncertainties in the $Z\gamma$ simulation sample (11%), the pileup contribution (6%), the other simulation samples (2%), and the luminosity (1%).

The subtraction-method estimate of $N_{Z\gamma}^{\gamma\text{fake}}$ agrees with the nominal purity-based result (see Appendix C.1.1 for more details).

5.1.2 Ratio of ZZ+jet and Z+jet events

For the ratio of ZZ+jet and Z+jet events, we need to define two new CRs, the ZZ+jet CR and the Z+jet CR. In comparison with the SR, the ZZ+jet CR has no requirements on the photon. The selection criteria on the leptons are the same as in the SR. Additionally, jet requirements are imposed. As

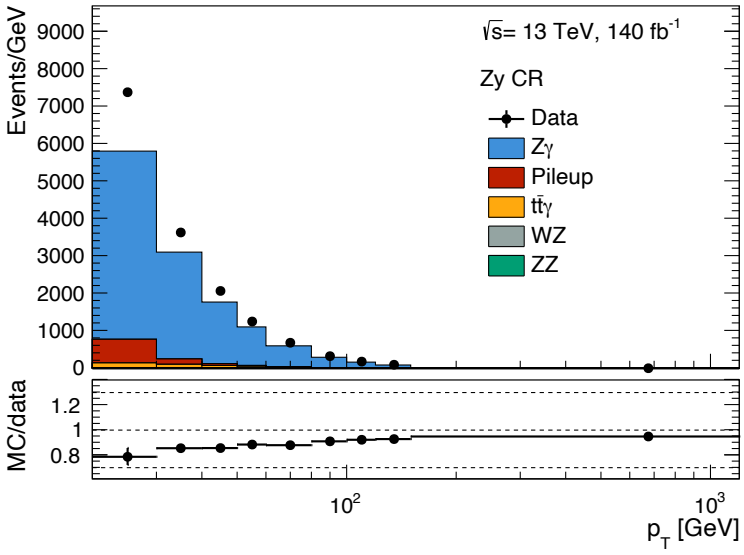


Figure 5.4: Data and expected contributions from prompt-photon $Z\gamma$, pileup, $t\bar{t}\gamma$, WZ, and ZZ events in the $Z\gamma$ CR as transverse-momentum distribution of the photon. The $Z\gamma$ events with a non-prompt photon are not shown. The ratio of expected contributions to data is shown at the bottom.

described earlier, the jet selection should be similar to the photon selection, thus, the leading jet candidate is selected, a transverse momentum of $p_{\mathrm{T}} > 20\,\mathrm{GeV}$ is required, and the jet must satisfy $|\eta| < 2.6$. The Z+jet CR also has no photon requirements, fulfills the leading-Z-boson criteria of the SR definition, and uses the same jet-selection criteria as the ZZ+jet CR. An overview of the selections defining the ZZ+jet CR and Z+jet CR is presented in Table A.8.

The ZZ+jet and Z+jet events in their dedicated CRs are selected directly from data. In the Z+jet CR the background from other processes is less than 2.5%; roughly half of this comes from top-quark decays and the other half from diboson production and misidentified leptons [136]. Because of the low contribution, no background subtraction is performed.

The background in the ZZ+jet CR is larger: in inclusive ZZ production the background is 6.5%, dominated by misidentified leptons [137]. By including the misidentified-lepton background in ZZ+jet events, the non-prompt photon estimate in the SR contains the contribution with a non-prompt photon and misidentified leptons. Thus, no background subtraction is applied to the ZZ+jet CR either.

The ratio of ZZ+jet and Z+jet events for different kinematic properties of the jet is shown in Figs. 5.5 and 5.6. In Fig. 5.5, a dependence of the ratio on the jet's transverse momentum is observed. Due to energy-momentum conservation, the additional jet in the ZZ+jet system must balance a larger momentum than the jet in the Z+jet system. Consequently, the jet's transverse-momentum spectrum in ZZ+jet events is shifted to higher values, producing an increase of the ratio at high jet p_{T}. In contrast, the ratio is approximately independent of the jet's pseudorapidity and azimuthal angle, see Fig. 5.6.

The data ratio is compared with predictions from simulation. For the predictions, two generators are used. The $pp \to \ell\ell$ process with up to three and two additional jets at NLO is modeled with the MadGraphPythia8 and the Sherpa 2.2.11 event generator, respectively. The $qq \to \ell\ell\ell\ell$ process with up to one additional jet at NLO is modeled with the MadGraphPythia8 and the Sherpa 2.2.2 event generator. Finally, the $gg \to \ell\ell\ell\ell$ process with one additional jet at LO is generated with Sherpa 2.2.2. More information on the samples is given in Appendix A.3.

The *MadGraph ratio* is defined as the number of events from the MadGraphPythia8 $qq \to \ell\ell\ell\ell$ simulation sample passing the ZZ+jet CR divided by the events from the MadGraphPythia8 $pp \to \ell\ell$ simulation sample passing the Z+jet CR. The *Sherpa ratio* is defined analogously.

The total uncertainty of the MadGraph and Sherpa ratio is the combination of the statistical uncertainty from the simulation samples (0.4%), the experimental uncertainties (6% and 9%), the theoretical uncertainties (6% and 7%), and an uncertainty in the jet characteristics (10%). The variations to derive the experimental and theoretical uncertainties are applied to the ratio and partially cancel. More details about their different contributions are given in Appendix C.2. The derivation of the uncertainty in the jet characteristics is described after the data and prediction comparison.

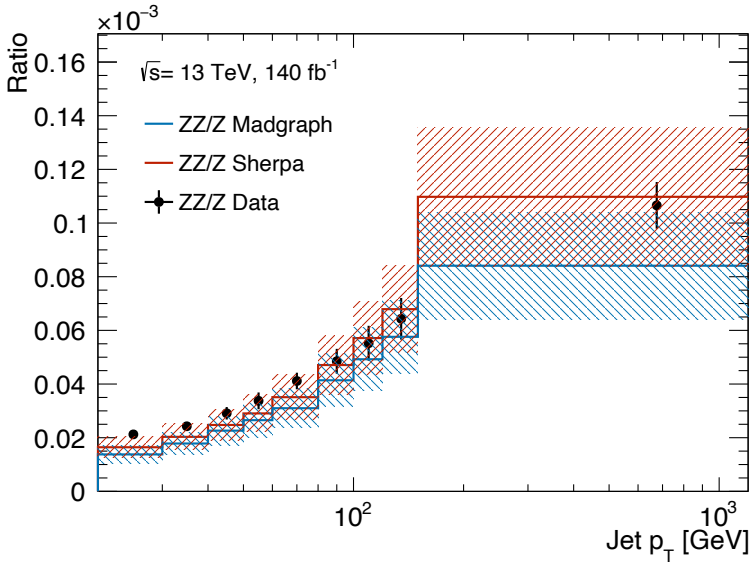
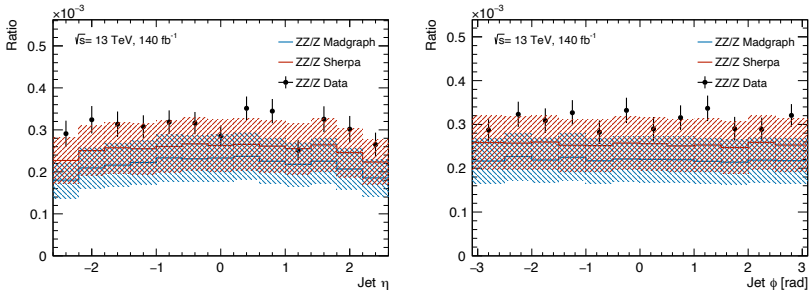


Figure 5.5: The transverse-momentum distribution of the jet for the ratio of ZZ+jet and Z+jet events. The shaded regions indicate the total uncertainties of the predicted ratios; the data uncertainty is statistical only.



(a) **(b)**

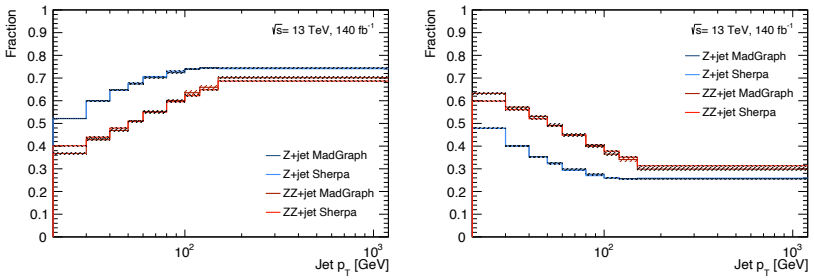
Figure 5.6: The pseudorapidity distribution of the jet for the ratio of ZZ+jet and Z+jet events (a), the azimuthal angle distribution of the jet for the ratio of ZZ+jet and Z+jet events (b). The shaded regions show the total uncertainty of the predicted ratios. The data uncertainty is only statistical.

In Fig. 5.6, the predictions underestimate the ratio. The difference between the Sherpa ratio and the MadGraph ratio is mainly due to the $gg \to \ell\ell\ell\ell$ process, which is not included in the MadGraph ratio. A naive explanation for the data-vs-prediction discrepancy would be a missing normalization factor. However, in Fig. 5.5, we also observe a slight shape difference. This shape discrepancy originates primarily from Z+jet events. The transverse-momentum distribution of the jet is not modeled well for these events due to the limited understanding of QCD. The model underestimates the number of events with low transverse momenta and slightly overestimates them at high transverse momenta [138, 139]. Missing NLO electroweak corrections lead to a 10–15% underestimation of the predicted ZZ+jet events. The data also includes contributions from background processes as described earlier. The data and prediction comparison for the individual CRs are shown in Appendix C.1.3.

For the extrapolation to the SR, the data-derived ratio is used. However, we need simulations to study the characteristics of the jets in the ZZ+jet and the Z+jet events. The parton producing the jet has the largest effect on the probability of a jet being misidentified as a non-prompt photon. Thus, the fraction of quark- and gluon-induced jets for ZZ+jet and Z+jet events is studied. These fractions can be obtained from the truth information in the simulation samples.

In Fig. 5.7, the fraction of quark- and gluon-induced jets as a function of the jet's transverse momentum for ZZ+jet and Z+jet events is shown. For Z+jet events approximately 50% of the jets are quark-induced at low transverse momentum. This fraction increases with p_{T} up to 75%. The overall fraction of quark-induced jets is lower for ZZ+jet events. Only 40% of the low-p_{T} jets and 70% of the high-p_{T} jets are quark-induced. The fractions of gluon-induced jets is around 50% for Z+jet events at low p_{T} and decreases with p_{T} to 25%. For ZZ+jet events the fraction of gluon-induced jets is around 60% at low p_{T} and decreases to 30% at high p_{T}. Both event generators give consistent results.

The effect of the different fractions in ZZ+jet and Z+jet events on the ratio is studied as a function of the jet-faking-photon probability of quark-



(a) Fraction of quark-induced jets

(b) Fraction of gluon-induced jets

Figure 5.7: The fraction of quark- and gluon-induced truth jets for Z+jet and ZZ+jet events passing the Z+jet and ZZ+jet CR, respectively. The fractions are shown as function of the transverse momentum of the jet and for events from the MADGRAPHPYTHIA8 and SHERPA samples. The quark-induced fraction is shown in (a), the gluon-induced fraction in (b). Only the statistical uncertainties are shown.

versus gluon-induced jets. For this, we can write the ratio as

$$\frac{N_{ZZ+j}}{N_{Z+j}} = \frac{f_q^{ZZ} + f_g^{ZZ}}{f_q^{Z} + f_g^{Z}} \cdot \frac{N_{ZZ+j}}{N_{Z+j}}, \tag{5.6}$$

where f_q and f_g are the fractions of quark- and gluon-induced jets in ZZ+jet and Z+jet. In case the probability of faking a photon differs by a factor x for gluon-induced jets, the ratio is affected as

$$\frac{N_{ZZ+j}}{N_{Z+j}} \Rightarrow \frac{f_q^{ZZ} + x \cdot f_g^{ZZ}}{f_q^{Z} + x \cdot f_g^{Z}} \cdot \frac{N_{ZZ+j}}{N_{Z+j}}. \tag{5.7}$$

Due to the different fractions of quark- and gluon-induced jets for ZZ+jet and Z+jet events, the ratio varies depending on x, see Fig. 5.8.

In the extreme case that only quark-induced jets produce non-prompt photons ($x = 0$), the extrapolation ratio would be overestimated by $\approx 17\%$. In the opposite extreme where only gluon-induced jets produce non-prompt photons ($x \to \infty$), the ratio would be underestimated by $\approx 34\%$. Although it is generally expected that gluon-induced jets have a higher photon-faking probability due to their larger particle multiplicity and broader jet shape,

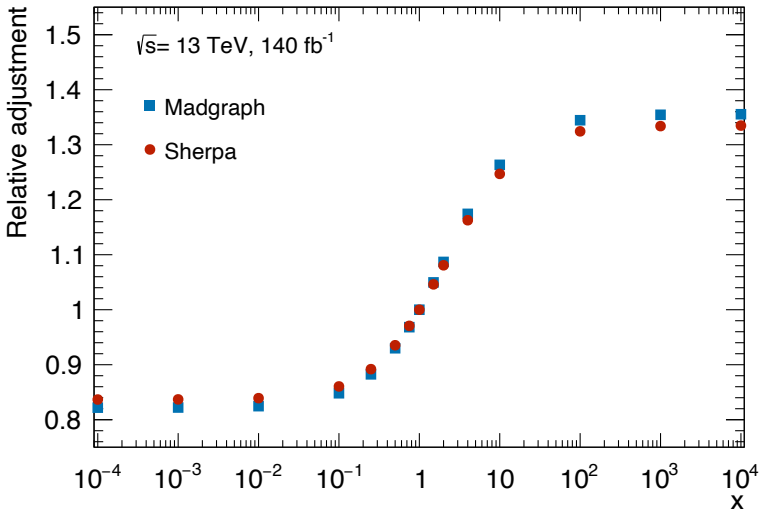


Figure 5.8: Effect of different quark- or gluon-induced jet-faking-probabilities. The relative adjustment on the fraction $\frac{f_q^{ZZ}+x\cdot f_g^{ZZ}}{f_q^{Z}+x\cdot f_g^{Z}} \cdot \frac{N_{ZZ+j}}{N_{Z+j}}$ for various values of x is shown for the MADGRAPHPYTHIA8 and SHERPA samples.

the exact factor is unknown. With the current knowledge, a 10% uncertainty is assigned to the ratio to cover the range of reasonable values of x.

5.1.3 Non-prompt photons in the signal region

The number of $Z\gamma$ events with a non-prompt photon and the ratio of ZZ+jet and Z+jet events can be combined to derive the number of events with non-prompt photons in the SR. The ratio, as well as $N_{Z\gamma}^{\gamma_{\text{fake}}}$, depends on the transverse momentum. Thus, the extrapolation to the SR is performed differentially. The number of non-prompt photons in the SR is

$$N_{ZZ\gamma}^{\gamma_{\text{fake}}} = 0.713 \pm 0.019\,(\text{stat.}) \pm 0.129\,(\text{syst.}). \tag{5.8}$$

The transverse-momentum distribution of $N_{ZZ\gamma}^{\gamma_{\text{fake}}}$ is presented in Fig. 5.9. In addition, the extrapolated distributions obtained with the simulation-based

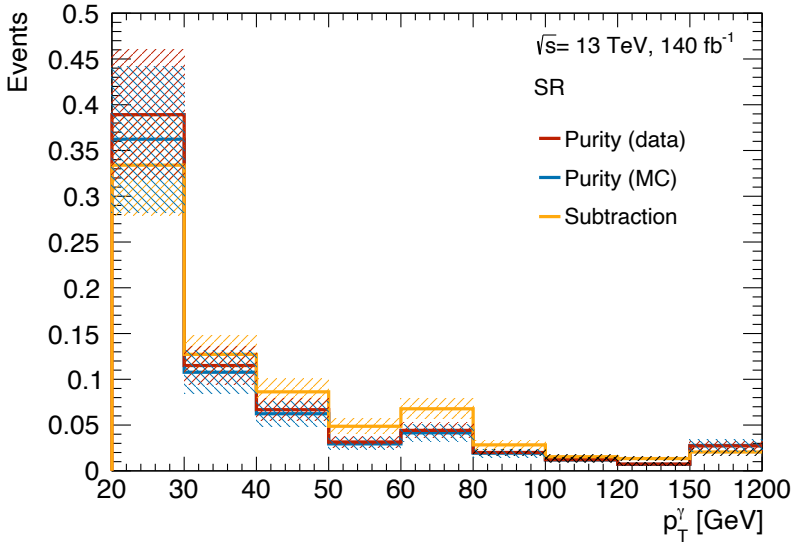


Figure 5.9: The transverse-momentum distribution of the non-prompt-photon events in the SR. Both the nominal estimate and the results with the simulation-based purity estimate and the subtraction method are displayed. The total systematic uncertainties are indicated by the shaded regions.

purity estimate and with the subtraction method for $N_{Z\gamma}^{\gamma\text{fake}}$ are shown.

The systematic uncertainty on $N_{ZZ\gamma}^{\gamma\text{fake}}$ is the combination of the uncertainty in the purity (14%), the jet-characteristic differences between ZZ+jet and Z+jet events (10%), the effect of the phase-space difference to the $Z\gamma$ analysis (7%), and the uncertainty in the luminosity (1%). A summary of the uncertainties is given in Table 5.1.

The number of non-prompt-photon events in the SR for the various Z-boson decay channels is given in Table 5.2. The distribution among the different channels is taken from the ZZ+jet events, and the same relative systematic uncertainty is applied to all channels.

Table 5.1: Summary of the uncertainty sources and their relative contribution to the final estimate of $N_{ZZ\gamma}^{\gamma\text{fake}}$.

Source	Relative uncertainty [%]
Statistics (tot.)	2.6
Purity measurement (tot.)	14
Phase-space uncertainty	7
Quark-gluon variations	10
Integrated luminosity	0.8
Total uncertainty	18

Table 5.2: Number of estimated non-prompt-photon events in the SR for the different lepton flavor channels.

Channel	Events
$4e$	0.135 ± 0.004 (stat.) ± 0.024 (syst.)
$2e2\mu$	0.343 ± 0.009 (stat.) ± 0.062 (syst.)
4μ	0.234 ± 0.006 (stat.) ± 0.043 (syst.)

5.1.4 Validation

The ratio method is validated in the $WZ\gamma$ CR. This CR is defined similarly to the SR, but instead of at least four leptons passing the Z-boson selection requirements, only at least three leptons are required, of which two must satisfy the leading-Z criteria (see Table A.9).

Using the same ansatz as for $ZZ\gamma$ events with a non-prompt photon (Eq. (5.1)), the following relation holds:

$$\frac{N_{WZ\gamma}^{\gamma\text{fake}}}{N_{WZ}^{\text{jets}}} = \frac{N_{Z\gamma}^{\gamma\text{fake}}}{N_{Z}^{\text{jets}}}. \tag{5.9}$$

Here, $N_{WZ\gamma}^{\gamma\text{fake}}$ is the number of $WZ\gamma$ events with a non-prompt photon in the $WZ\gamma$ CR and N_{WZ}^{jets} is the number of WZ+jet events passing the WZ+jet selection—the same requirements as in the Z+jet CR, but with an additional lepton. The right-hand side of the equation is identical to that of Eq. (5.1).

We can estimate $N_{WZ\gamma}^{\gamma_{\text{fake}}}$ from the previous derived results for $N_{Z\gamma}^{\gamma_{\text{fake}}}$ and N_Z^{jets}, together with the number of WZ+jet events passing the WZ+jet selection. This estimate can be compared with the number of $WZ\gamma$ events with a non-prompt photon obtained in the ATLAS $WZ\gamma$ analysis [33].

The number of WZ+jet events passing the WZ+jet selection is estimated with MC simulation samples. We do not use data due to the dominant background fraction (30–70%). Since there are no selection criteria on missing transverse energy or the transverse mass of the W boson, the background—especially misidentified leptons—is large. Therefore, we also use the Z+jet estimate from simulation.

Furthermore, the photon-p_{T} requirement in the $WZ\gamma$ analysis is $p_{\text{T}} > 15\,\text{GeV}$. For a fair comparison we derive $N_{Z\gamma}^{\gamma_{\text{fake}}}$, N_Z^{jets}, and N_{WZ}^{jets} using the same photon-p_{T} threshold.

Applying the same procedure as before, the number of $WZ\gamma$ events with a non-prompt photon is

$$N_{WZ\gamma}^{\gamma_{\text{fake}}}(p_{\text{T}} > 15\,\text{GeV}) = 14.7 \pm 0.1\,(\text{stat.}) \pm 3.7\,(\text{syst.}). \tag{5.10}$$

The systematic uncertainty assumes the same relative uncertainty as listed in Table 5.1. This uncertainty underestimates the true uncertainty: the purity estimate for $15\,\text{GeV} < p_{\text{T}} < 20\,\text{GeV}$ has a large uncertainty, and the ratio estimate from simulation also yields a larger uncertainty than the data. Nevertheless, the result agrees with the expected non-prompt-photon contribution from the $WZ\gamma$ analysis, $N_{WZ\gamma}^{\gamma_{\text{fake}}} = 14.6 \pm 3.4$ (stat.) ± 2.0 (syst.) [33].

5.2 Misidentified leptons

The second-largest background contribution comes from events with misidentified—also called fake—leptons, e. g., $WZ\gamma$ or $t\bar{t}\gamma$ events. While these processes have a prompt isolated photon, the leptonic decay results in only two or three prompt leptons. An event with one or two additional misidentified leptons can pass the selection criteria of the SR. Due to the significantly larger cross-sections of e. g., $WZ\gamma$ or $t\bar{t}\gamma$ processes, the contribution is non-negligible and needs to be estimated.

We use the matrix method [140] to derive the contribution of events with misidentified leptons in the SR. The matrix depends on the efficiencies of the prompt/real and misidentified/fake leptons to pass the SR selection relative to a looser selection. These efficiencies will be estimated in Section 5.2.2. Due to the low statistics of events with four loose leptons and one prompt photon, the misidentified lepton contribution is first determined for ZZ events and extrapolated to the SR, as described in Section 5.2.3.

5.2.1 Matrix method

Before we derive the matrix method for a four lepton final state, we will explain the concept for the one lepton case.

Matrix method for one lepton

The matrix method relates the number of real and fake leptons (N^r and N^f) to the number of leptons passing a tight selection (N^{T}) and leptons passing a loose but failing a tight selection (N^{LnT}),

$$\begin{pmatrix} N^{\mathrm{T}} \\ N^{\mathrm{LnT}} \end{pmatrix} = \begin{pmatrix} \epsilon_r & \epsilon_f \\ 1-\epsilon_r & 1-\epsilon_f \end{pmatrix} \begin{pmatrix} N^r \\ N^f \end{pmatrix}. \tag{5.11}$$

The matrix depends on the real and fake efficiencies (ϵ_r and ϵ_f). Using data, N^{T} and N^{LnT} are derived by selecting the events fulfilling the required selection criteria. The real and fake efficiencies can be determined with dedicated simulation samples or CRs in data. With these ingredients given, the unknown number of fake leptons passing the tight selection, $N^f_{\mathrm{T}} = \epsilon_f \cdot N^f$, can be derived. For this, we can invert the matrix,

$$\begin{pmatrix} N^r \\ N^f \end{pmatrix} = \begin{pmatrix} \epsilon_r & \epsilon_f \\ 1-\epsilon_r & 1-\epsilon_f \end{pmatrix}^{-1} \begin{pmatrix} N^{\mathrm{T}} \\ N^{\mathrm{LnT}} \end{pmatrix} = \begin{pmatrix} \frac{1-\epsilon_f}{\epsilon_r-\epsilon_f} & -\frac{\epsilon_f}{\epsilon_r-\epsilon_f} \\ -\frac{1-\epsilon_r}{\epsilon_r-\epsilon_f} & \frac{\epsilon_r}{\epsilon_r-\epsilon_f} \end{pmatrix} \begin{pmatrix} N^{\mathrm{T}} \\ N^{\mathrm{LnT}} \end{pmatrix} \tag{5.12}$$

to get N^f in dependence of the known efficiencies, N^{T}, and N^{LnT}. Thus, the number of fake leptons passing the tight selection is:

$$N^f_{\mathrm{T}} = \left[1 - \frac{\epsilon_r(1-\epsilon_f)}{\epsilon_r-\epsilon_f}\right] N^{\mathrm{T}} + \frac{\epsilon_r\epsilon_f}{\epsilon_r-\epsilon_f} N^{\mathrm{LnT}}. \tag{5.13}$$

Table 5.3: Overview of the 16 different scenarios for a four-leptons event with leptons that pass the tight selection (✓) and leptons that pass the loose but fail the tight selection (✗). When the order of the individual leptons is irrelevant, the 16 scenarios can be grouped into five categories (SR, CR1–4).

Region	ℓ_1	ℓ_2	ℓ_3	ℓ_4
SR	✓	✓	✓	✓
CR1	✓	✓	✓	✗
	✓	✓	✗	✓
	✓	✗	✓	✓
	✗	✓	✓	✓
CR2	✓	✓	✗	✗
	✓	✗	✗	✓
	✓	✗	✓	✗
	✗	✓	✓	✗
	✗	✓	✗	✓
	✗	✗	✓	✓
CR3	✓	✗	✗	✗
	✗	✓	✗	✗
	✗	✗	✓	✗
	✗	✗	✗	✓
CR4	✗	✗	✗	✗

Matrix method for four leptons

In the case of four leptons, we do not have just N^{T} and N^{LnT}. Each lepton in the event fulfills either the tight or loose-not-tight criteria, resulting in 16 (2^4) options, see Table 5.3.

Since the ordering of the leptons is not unique, and we do not care which exact lepton is fake, we can combine the 16 cases into five: SR, CR1, CR2, CR3, and CR4. The lepton order is defined by their transverse momenta and the efficiencies depend on the momenta as well. Thus, the number of misidentified leptons is derived differentially as a function of lepton transverse momentum. We will later prove that the efficiency of each lepton for a given transverse momentum is the same (see Section 5.2.2).

Similar to the one lepton case, a matrix relating the number of events with leptons passing the tight selection and leptons passing the loose and failing the tight selection to the number of events with real and fake leptons can be determined. This matrix depends on the real and fake efficiencies. By inverting the matrix and after some algebra (see Appendix D.1), the number of events passing the tight selection with at least one misidentified lepton, N_{fakes}, is

$$\begin{aligned} N_{\text{fakes}} = & \left[1 - \left(\prod_{i=1}^{4} \frac{\epsilon_{r,i}(1-\epsilon_{f,i})}{(\epsilon_{r,i}-\epsilon_{f,i})}\right)\right] N_{\text{SR}} \\ & + \left(\prod_{i=1}^{3} \frac{\epsilon_{r,i}(1-\epsilon_{f,i})}{(\epsilon_{r,i}-\epsilon_{f,i})}\right) \frac{\epsilon_{r,j}\epsilon_{f,j}}{(\epsilon_{r,j}-\epsilon_{f,j})} N_{\text{CR1}} \\ & - \left(\prod_{i=1}^{2} \frac{\epsilon_{r,i}(1-\epsilon_{f,i})}{(\epsilon_{r,i}-\epsilon_{f,i})}\right) \left(\prod_{j=1}^{2} \frac{\epsilon_{r,j}\epsilon_{f,j}}{(\epsilon_{r,j}-\epsilon_{f,j})}\right) N_{\text{CR2}} \\ & + \frac{\epsilon_{r,i}(1-\epsilon_{f,i})}{(\epsilon_{r,i}-\epsilon_{f,i})} \left(\prod_{j=1}^{3} \frac{\epsilon_{r,j}\epsilon_{f,j}}{(\epsilon_{r,j}-\epsilon_{f,j})}\right) N_{\text{CR3}} \\ & - \left(\prod_{j=1}^{4} \frac{\epsilon_{r,j}\epsilon_{f,j}}{(\epsilon_{r,j}-\epsilon_{f,j})}\right) N_{\text{CR4}}, \end{aligned} \tag{5.14}$$

where the index i denotes leptons passing the tight selection and the index j denotes leptons passing the loose but failing the tight selection. The number of events passing the lepton requirements of each of the regions is given by N_{SR} or N_{CR}. The SR represents the case where all leptons pass the tight requirements. Each CR (CR1–4) contains three to zero[1] leptons passing the tight selection and one to four leptons passing the loose but failing the tight selection, respectively.

5.2.2 Real and fake efficiencies

For the expression to derive the number of events with a misidentified lepton, the real and fake efficiencies are needed. As mentioned above, the real (fake) efficiency is the fraction of real (fake) leptons passing the tight selection relative to a looser selection.

[1]The loose identification requirements on the dilepton triggers prevent a trigger bias.

Table 5.4: Summary of the lepton requirements that differ in the loose and tight selection.

Lepton	Selection	Identification	Isolation	$d0$ significance
Electrons	loose	loose	—	< 5
	tight	medium	loose	< 5
Muons	loose	medium	—	< 10
	tight	medium	loose	< 3

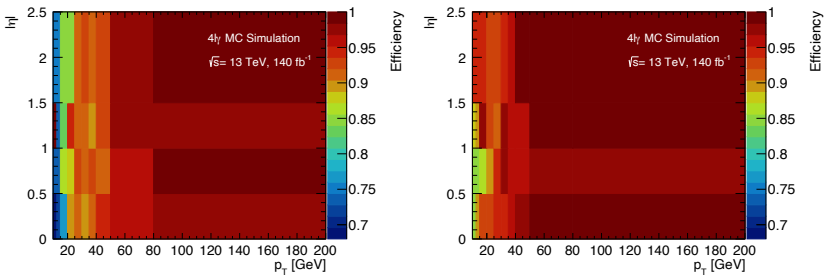
The tight selection is the signal selection. Regarding the leptons, this means electrons must pass the Medium identification WP and the Loose isolation WP, and muons must pass the PflowLoose isolation WP and their transverse impact parameter must fulfill $|d_0|/\sigma_{d_0} < 3$.

The looser selection has fewer constraints on the electrons and muons. Thus, the loose selection has the same requirements as the signal selection, but electrons must only pass the Loose identification WP and no isolation is required, and muons must fulfill the relaxed transverse-impact-parameter requirement of $|d_0|/\sigma_{d_0} < 10$ and no isolation is required. A summary of the lepton-requirement differences is listed in Table 5.4.

Real efficiency

The real efficiency is determined with MC simulation samples. All events passing the loose selection are selected from the $4\ell\gamma$ signal sample. To ensure that the selected lepton is real, it is matched to a truth lepton via the truth information in the simulation sample. Only matched leptons are considered for the real-efficiency determination. From all leptons passing the previously mentioned requirements, the fraction that also passes additionally the signal selection is obtained. This fraction represents the real efficiency.

This efficiency differs for electrons and muons, so it is derived separately for each lepton flavor. As mentioned before, the efficiency also depends on the transverse momentum of the lepton, thus it is derived differentially. Since the efficiency of the isolation and identification WPs depend on pseudorapidity, the efficiency is derived differentially in pseu-



(a) **(b)**

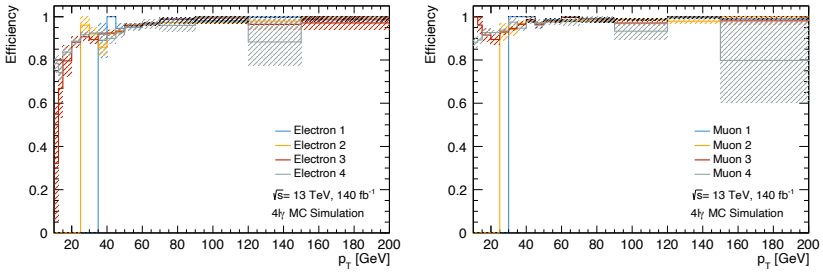
Figure 5.10: The efficiency to pass the tight selection relative to the loose selection for real electrons (a) and real muons (b) as function of p_{T} and $|\eta|$.

dorapidity as well. This results in two 2D real-efficiency distributions, one for electrons and one for muons, see Fig. 5.10. The binning has been optimized for the real and fake efficiencies combined such that each bin has enough statistics while preserving the shape of the transverse-momentum and pseudorapidity distributions.

As mentioned earlier, the efficiency does not depend on the specific lepton (leading versus sub-leading, etc.). The transverse-momentum distributions of the real efficiency for each individual lepton per event are shown for electrons and muons in Fig. 5.11. The efficiency distributions for all electrons (muons) agree within their uncertainties, excluding the extremely low-statistics bins (e. g., the first p_{T} bin or the first bins after the p_{T} threshold of the leading lepton).

Fake efficiency

The fake efficiency needs to be determined in data because of the limited understanding of jets being misidentified as leptons or non-prompt leptons from hadron decays and thus, a poor modeling of the kinematic properties. We define a $Z + 1\ell$ CR which contains a large fraction of fake leptons. This CR contains events with exactly three leptons, two of which fulfill the requirements of the leading Z boson in the SR and the third lepton needs to pass the loose-selection requirements, see Table 5.4. An overview of all



(a) **(b)**

Figure 5.11: The efficiency for each lepton in the event to pass the tight selection relative to the loose selection as function of p_{T} for real electrons (a) and real muons (b).

requirements on the $Z + 1\ell$ CR is presented in Table A.10.

The third lepton is, with high probability, a fake lepton. All events in data passing the $Z + 1\ell$ CR requirements are selected. Contributions with three real leptons (e. g., ZZ and WZ events) in the $Z + 1\ell$ CR are estimated with dedicated MC simulation samples and subtracted from the data yield. In the remaining events, the third lepton is assumed to be a fake lepton. For all these leptons, the fraction passing the tight-selection criteria is estimated and represents the fake efficiency. The 2D distributions for electrons and muons with the fake efficiency are shown in Fig. 5.12.

While the real efficiencies are fairly similar for electrons and muons, the fake efficiencies differ significantly. Overall, the muon fake efficiencies are lower due to the more effective reconstruction. Since prompt muons leave signatures in every sub-detector and can be clearly identified through the presence in the MS, the probability of a fake muon passing the muon reconstruction, isolation, and identification requirements is low.

5.2.3 Estimation of misidentified lepton events

For the estimation of the number of events with at least one fake lepton in the SR, we need the efficiencies as well as the data yields for the SR and the CR1–4. Since the number of events in CR1–4 combined is eight (two in

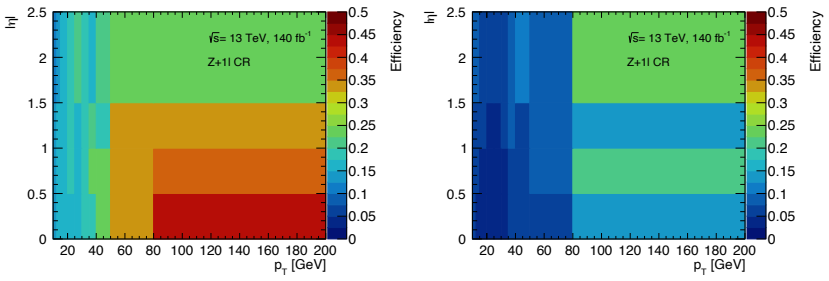


Figure 5.12: The efficiency to pass the tight selection relative to the loose selection for fake electrons (a) and fake muons (b) as function of p_{T} and $|\eta|$.

CR1, six in CR2, none in CR3 and CR4) and we are blinded in the SR, we estimate the number of fake lepton events in the ZZ CR and extrapolate the result to the SR.

The selection criteria of the ZZ CR (CR'1–4) are the same as for the SR (CR1–4), without all photon requirements (see Appendix A.4). Eq. (5.14) is taken but with $N_{ZZ\,\mathrm{CR}}$ instead of N_{SR} and $N_{\mathrm{CR'}}$ instead of N_{CR}. The number of events passing the CR'1–4 is nearly three orders of magnitude larger than for CR1–4.

With the number of events passing the different CRs and the real and fake efficiencies, we get the number of events with at least one fake lepton in the ZZ CR, $N_{ZZ}^{\mathrm{fake}\,\ell} = 50 \pm 9\,(\mathrm{stat.}) \pm 29\,(\mathrm{syst.})$. This number contains contributions from fake electrons and fake muons, see Table 5.5 for details.

The statistical uncertainty is from the data statistics, $\sqrt{N}$. The systematic uncertainties are the uncertainties in the MC simulation samples used for the subtraction of the prompt lepton contributions (56%), the uncertainty from the choice of binning (14%), and the uncertainties in the real and fake efficiencies (7%). The uncertainty in the luminosity is negligible.

The uncertainty in the MC simulation samples is the dominant uncertainty. The prompt lepton contributions estimated via MC simulations are varied +30% and -10%. The fake efficiencies are derived with the varied contribution subtracted. The difference to the nominal estimate with the varied fake efficiencies is taken as uncertainty. The choice of varying the

Table 5.5: Overview of the number of fake lepton events in the ZZ CR. The results are given for the $4e$, $2e2\mu$ and 4μ channels. The $4e$ channel has contributions only from fake electrons, the 4μ channel only from fake muons, and the $2e2\mu$ channel has mixed contributions, predominantly from fake electrons. In each case the fake estimate was derived as a function of transverse momentum and pseudorapidity. The statistical and systematic uncertainties are given.

Channel	Events
$4e$	17 ± 6 (stat.) ± 13 (syst.)
$2e2\mu$	29 ± 6 (stat.) ± 17 (syst.)
4μ	4.2 ± 1.5 (stat.) ± 1.9 (syst.)

MC simulation contributions by +30% and -10% is based on the results from the WZ [141, 142] and ZZ [137] analyses. The measured cross-sections have an uncertainty of 5–7% and 6%, respectively. In contrast to those analyses, no NLO-to-NNLO differential scale factors are applied. These scale factors result in corrections of +10% up to +20%. To take both effects into account, we vary the contributions asymmetrically.

The uncertainty in the binning is the difference to the nominal value from the estimate with flat real and fake efficiencies. The uncertainties in the efficiencies are the propagated Binomial uncertainties.

To derive the number of events with fake leptons in the SR, we need to extrapolate $N_{ZZ}^{\text{fake }\ell}$ from ZZ CR to the SR. Since the number of fake lepton events should be approximately independent of an additionally produced photon, the following relation should hold:

$$\frac{N_{ZZ\gamma}^{\text{fake }\ell}}{N_{ZZ\gamma}} = \frac{N_{ZZ}^{\text{fake }\ell}}{N_{ZZ}}, \tag{5.15}$$

with $N_{ZZ\gamma}^{\text{fake }\ell}$ the number of events with at least one fake lepton in the SR. The number of $ZZ\gamma$ events in the SR and ZZ events in the ZZ CR are $N_{ZZ\gamma}$ and N_{ZZ}, respectively.

We estimate $N_{ZZ\gamma}$ with the two signal MC simulations and N_{ZZ} with the SHERPA 2.2.2 $qq \to \ell\ell\ell\ell$ and $gg \to \ell\ell\ell\ell$ MC simulation samples (see Appendix A.3). This results in the number of events with at least one fake

Table 5.6: Number of expected events with a fake lepton in the SR for the different lepton-flavor channels. The $2e2\mu$ channel contains electron fakes, muon fakes, and mixed fakes.

Channel	Events
$4e$	0.041 ± 0.015 (stat.) ± 0.035 (syst.)
$2e2\mu$	0.071 ± 0.016 (stat.) ± 0.048 (syst.)
4μ	0.010 ± 0.004 (stat.) ± 0.005 (syst.)

lepton in the SR,

$$N_{ZZ\gamma}^{\text{fake}\,\ell} = 0.12 \pm 0.02\ (\text{stat.}) \pm 0.08\ (\text{syst.}). \tag{5.16}$$

The results for each decay channel are shown in Table 5.6 and in Fig. 5.13. The contribution of misidentified leptons in the $4e$ channel is significantly larger than in the 4μ channel. This is a direct result of the higher fake efficiencies for electrons.

The statistical uncertainty includes the propagated data statistics from $N_{ZZ}^{\text{fake}\,\ell}$ and the statistical uncertainties of the MC simulation samples. The systematic uncertainties are the propagated uncertainties of $N_{ZZ}^{\text{fake}\,\ell}$ (58%) and a modeling uncertainty to account for the difference in the transverse-momentum distribution of ZZ and $ZZ\gamma$ events (31%). A summary of the uncertainties is given in Table 5.7.

For the modeling uncertainties, the transverse-momentum distribution of the data events passing the various CRs for the estimation of $N_{ZZ}^{\text{fake}\,\ell}$ is reweighted. The ratio of the transverse-momentum distribution of $ZZ\gamma$ events and ZZ events estimated via SHERPA MC simulation samples is used for reweighting. The transverse-momentum distributions as well as their ratios are shown in Fig. 5.14. The number of events with fake leptons is estimated with the reweighted transverse-momentum distribution and the difference to the nominal estimate is taken as uncertainty.

The pseudorapidity distributions of the leptons in ZZ and $ZZ\gamma$ events have the same shape and agree within uncertainties. Thus, no pseudorapidity reweighting is performed.

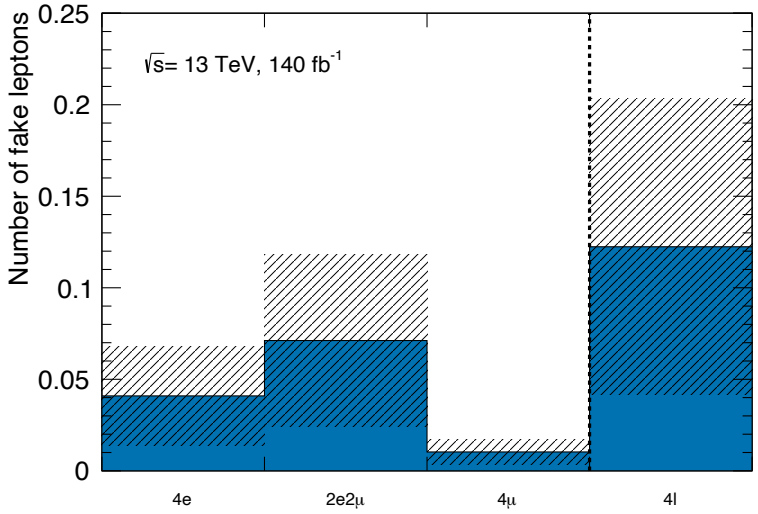


Figure 5.13: The number of misidentified lepton events in the $4e$, 4μ, $2e2\mu$, and 4ℓ channels. The 4ℓ channel is the sum of the other three channels. The shaded region shows the total uncertainty.

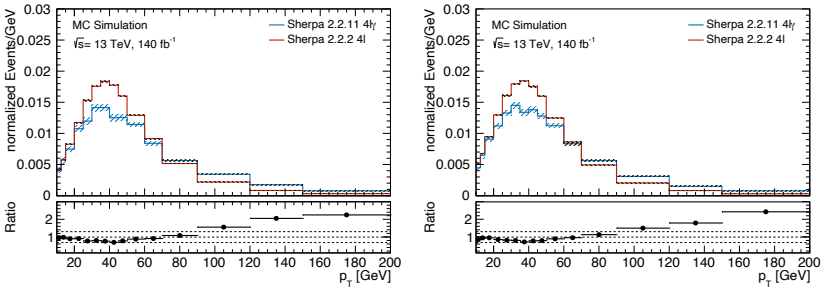


Figure 5.14: Transverse-momentum distribution of the electrons (a) and muons (b) from $ZZ\gamma$ events and ZZ events, as well as their ratios. The dotted lines in the ratio indicate an uncertainty band of ± 0.31.

Table 5.7: Summary of the uncertainty sources and their relative contribution to the number of events with a fake lepton in the SR, $N_{ZZ\gamma}^{\text{fake }\ell}$.

Source	Relative uncertainty [%]
Statistics	18
Efficiency ($N_{ZZ}^{\text{fake }\ell}$)	7
MC variations ($N_{ZZ}^{\text{fake }\ell}$)	56
Binning ($N_{ZZ}^{\text{fake }\ell}$)	14
Modeling	31
Total systematic uncertainty	64
Total uncertainty	66

5.2.4 Validation

The misidentified lepton estimate is validated in a same-sign validation region (VR). Since the fake leptons come from jets and hadron decays, the number of events with a fake lepton should be independent of the charge of the final-state particles from the hard interaction. Thus, changing the charge of one lepton in the final state should result in the same number of events with a fake lepton. The same-sign VR has the same requirements as the SR but, instead of two OSSF lepton pairs, one OSSF lepton pair and one same-sign same-flavor (SSSF) lepton pair is required. The same-sign VR yields zero events.

To validate the $N_{ZZ}^{\text{fake }\ell}$ estimate in the ZZ CR, the same validation is applied in the same-sign VR'. This VR is defined as the same-sign VR but without any photon requirements. The data yield in the same-sign VR' is 58 ± 8. Less than two events are from prompt lepton backgrounds ($t\bar{t}Z$: 1.7, WWZ : 0.2) and not considered in the comparison. The data yield in the same-sign VR' agrees within uncertainties with the $N_{ZZ}^{\text{fake }\ell}$ estimate. The distribution in the different decay channels is shown in Fig. 5.15.

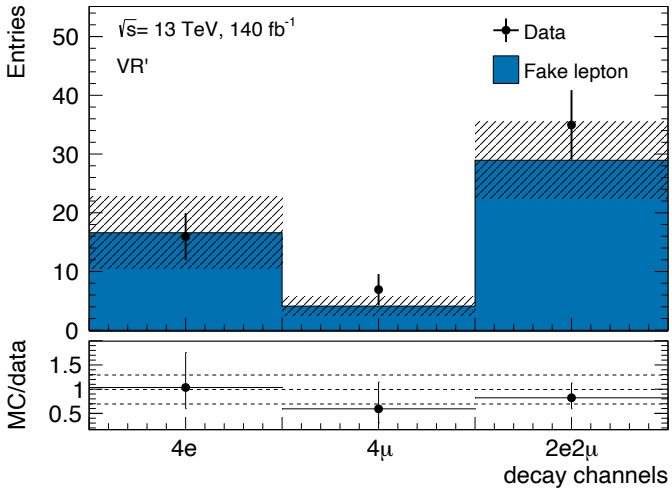


Figure 5.15: The data yield and the number of events with a fake lepton in the $4e$, 4μ and $2e2\mu$ channels. One of the lepton pairs is an OSSF pair and the other is a SSSF pair. The data points have statistical uncertainty only; the fake lepton estimate shows the total uncertainty of $N_{ZZ}^{\text{fake }\ell}$ (no modeling uncertainty included).

5.3 Pileup

Due to high instantaneous luminosity, more than one collision per bunch-crossing occurs at each IP. In Run 2 an average of $\langle\mu\rangle = 33.7$ [143] simultaneous pp interactions per bunch-crossing took place in the ATLAS detector. Approximately one hard-scatter physics process occurs per collision; all additional interactions are pileup. However, a combination of two or more coincidental pp collisions can result in the same final state as the signal process.

The $4\ell\gamma$ final state can be produced through a combination of e. g., a single-Z event and a $Z\gamma$ event or a ZZ event and a single-photon production from two different overlaid pp collisions. The transverse and longitudinal impact-parameter requirements on the leptons ensure that all four selected leptons originate from the same vertex. Thus, the combinatorial

background from a single-Z event and a $Z\gamma$ event can be neglected, leaving the pileup contribution of $ZZ + \gamma$ events.

Reconstructed photons are distinguished as converted or unconverted (see Section 3.3.2). Converted photons do not leave tracks in the innermost part of the Inner Detector, and unconverted photons are only reconstructed from the clusters in the EM calorimeter. Thus, the extrapolation to the beam line is less accurate, resulting in a poor reconstruction of the photon's point of origin. A potential pileup contribution of a ZZ event overlaid with single-photon production needs to be estimated.

Since the two productions are independent of each other, the number of pileup events should be proportional to the production probability P of a ZZ event multiplied with the production probability of a single photon, $N_{\text{PU}} \propto P(ZZ)P(\gamma)$. Furthermore, the number of pileup events is positively correlated with the number of simultaneous *pp* collisions. Combining these two conditions, the number of pileup events at particle level can be written as follows:

$$N_{\text{PU}}^{\text{fid}} = \epsilon_{ZZ+\gamma}^{\text{fid}} \langle \mu \rangle \frac{\sigma_{ZZ}\sigma_{\gamma}}{\sigma_{\text{inel}}} \mathcal{L}. \tag{5.17}$$

The cross-sections σ_{ZZ} and σ_{γ} reflect the probabilities of their respective productions and are normalized by the total inelastic cross-section σ_{inel}. The efficiency $\epsilon_{ZZ+\gamma}^{\text{fid}}$ gives the fraction of ZZ and single-photon events passing the selection criteria of the FR.

This efficiency is derived by randomly overlaying ZZ events with γ+jets events from two different MC simulations at particle level. The two randomly overlaid events are treated as one event and need to fulfill the FR selection criteria. The efficiency is then calculated via the ratio of events passing the FR to all randomly overlaid events. For the weighted MC simulations this results in

$$\epsilon^{\text{fid}} = \frac{\Sigma_{\text{fid}} w}{\Sigma_{\text{sel}} w}, \tag{5.18}$$

where $\Sigma_{\text{sel}} w$ is the sum of weights of the randomly selected events before any selection criteria are applied and Σ_{fid} the sum of weights of the events passing the FR selection requirements. The weight of each event is the product of the weight of the ZZ event and the γ+jets event.

Table 5.8: Overview of the results taken from other analyses or publications. The numbers are given with their uncertainties and references.

$\langle\mu\rangle$	33.7	[143]
σ_{ZZ}	(1.25 ± 0.08)pb	[144]
σ_{γ}	(460 ± 120) nb	[145]
σ_{inel}	(78.1 ± 2.9) mb	[146]
$\mathcal{L}$	(140.1 ± 1.2) fb^{-1}	[125]

The SHERPA 2.2.2 $qq \to \ell\ell\ell\ell$ MC event generator sample is used for the ZZ events and the SHERPA 2.2.2 $pp \to \gamma$+jets MC event generator sample for the γ+jets events, see Appendix A.3 for details. For the efficiency estimation at particle level no detector simulation is needed. One random event from each of the MC event generator samples is chosen, and the FR selection requirements are imposed. This process is repeated 1,000,000 times to reduce the statistical uncertainty of the efficiency.

Due to the selection of five final state particles, the efficiency is heavily reduced through the acceptance requirements on each particle. Additionally, the transverse-momentum distribution of the single photon is softer than for the signal process (see Fig. 5.16a) and thus also reduces the efficiency. The total efficiency is $\epsilon^{\text{fid}}_{ZZ+\gamma} = 0.78 \pm 0.02\,\%$.

The efficiencies differ for the decay channels due to the acceptance differences of electrons and muons in the fiducial region. These mainly arise through the larger probability of bremsstrahlung for the electron due to its lower mass. This effect is partially corrected for by summing the energy of photons within a cone of radius $\Delta R < 0.1$ to the lepton.

Besides the efficiency derived with the overlay of the MC simulations, results from previous measurements are used for the estimation of pileup events and stated in Table 5.8. Combining the results, we derive the expected number of pileup events at particle level,

$$N^{\text{fid}}_{\text{PU}} = 0.27 \pm 0.06. \tag{5.19}$$

For the estimation of the pileup background contribution in the SR, we need the number of pileup events at reconstruction level. To extrapolate the number of pileup events from particle level to reconstruction level, we can

Table 5.9: Number of pileup events expected for the different lepton flavor channels and the corresponding correction factor. The uncertainty of the correction factor is the combination of statistical and experimental uncertainties in the simulation samples.

Channel	Correction factor	Events
$4e$	0.239 ± 0.006	0.012 ± 0.001 (stat.) ± 0.003 (syst.)
$2e2\mu$	0.352 ± 0.009	0.043 ± 0.001 (stat.) ± 0.011 (syst.)
4μ	0.474 ± 0.012	0.033 ± 0.001 (stat.) ± 0.008 (syst.)

use the previously derived correction factor C. As described in Section 4.3.2, the correction factor is the ratio of simulated reconstructed events in the SR to simulated events at particle level passing the FR selection requirements. By multiplying the number of pileup events at particle level with the correction factor, we get the number of pileup events at reconstruction level.

As mentioned earlier, the correction factor is unique to each MC sample. However, the two individual correction factors for the SHERPA 2.2.2 $qq \to \ell\ell\ell\ell$ and the SHERPA 2.2.2 $pp \to \gamma$+jets MC event generator sample cannot take the selection criteria affecting both—leptons and photon—into account. Since the correction factor reflects the reconstruction inefficiencies and limited detector acceptance, the combined correction factors of the $4\ell\gamma$ and $ZH \to ZZ\gamma$ signal samples are used instead.

The correction factor differs significantly for the different decay channels, see Table 5.9. This is mainly due to the pseudorapidity acceptance and reconstruction efficiency differences for electrons and muons. Since the selection efficiency and the correction factor depend on the decay channel, the pileup contribution is estimated for each decay channel individually and summed afterwards, see Table 5.9. The combined pileup contribution is

$$N_{\text{PU}} = 0.089 \pm 0.002 \text{ (stat.)} \pm 0.022 \text{ (syst.)}. \tag{5.20}$$

The different uncertainty sources with their relative contribution are listed in Table 5.10. The statistical uncertainty on the pileup estimate comes from the MC overlay (2%). If necessary, this uncertainty could be further

Table 5.10: Overview of the uncertainty sources of the pileup estimate and their relative contributions.

Source	Relative uncertainty [%]
Efficiency	1.9
σ_γ	25
σ_{ZZ}	6
σ_{inel}	4
Correction factor	3
Total uncertainty	26

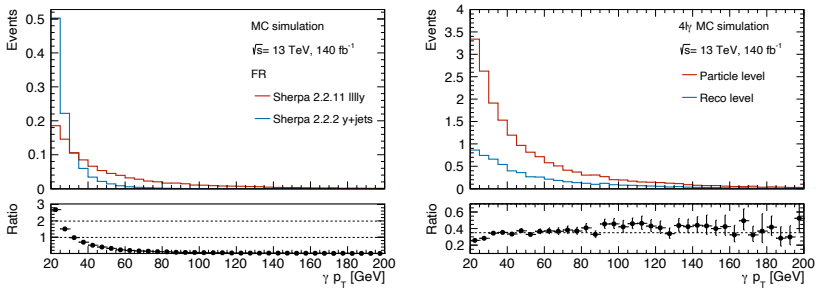
reduced by increasing the number of overlays. Compared to the other uncertainties, the statistical uncertainty is negligible.

Due to large scale variations (20–30% [145]), the single-photon cross-section has the dominant uncertainty. Other systematic uncertainties come from the ZZ and inelastic cross-sections measurements (6% and 4%). The uncertainty in the correction factor includes the statistical and experimental uncertainties (3%). The uncertainty in the integrated luminosity is negligible.

Additionally, the application of the $4\ell\gamma$ correction factor is studied. The largest difference between $ZZ\gamma$ events and the $ZZ + \gamma$ pileup events is the transverse-momentum distribution of the photon, see Fig. 5.16a. Even though the correction factor is not applied differentially, we can determine the correction factor as a function of the photon transverse momentum. In Fig. 5.16b, we can see the transverse-momentum distribution of the photon at reconstruction level and particle level. The lower part shows the ratio. Additionally, the value of the correction factor is shown.

The ratio of photon transverse momentum at reconstruction level and particle level is approximately constant over the range of the distribution. The ratio decreases at very low transverse momenta and increases slightly with higher momenta.

To quantify the effect of the difference in transverse momentum, the photon's transverse momentum of the $4\ell\gamma$ signal sample is reweighted to



(a) Photon p_{T} at particle level

(b) Photon p_{T} for the $4\ell\gamma$ sample

Figure 5.16: Comparison of the SHERPA 2.2.11 $\ell\ell\ell\ell\gamma$ sample and the SHERPA 2.2.2 γ+jets sample as a function of the transverse momentum of the photon (a). The transverse-momentum distribution of the SHERPA 2.2.11 $\ell\ell\ell\ell\gamma$ signal sample at reconstruction and particle level (b). The ratio represents the differential correction factor. The nominal correction factor is added as a dotted line.

the γ+jets photon distribution. The re-derived correction factor is multiplied with the pileup contribution at particle level and results in $N'_{\mathrm{PU}} = 0.084 \pm 0.021$. This result is consistent with the pileup contribution using the nominal correction factor of the $4\ell\gamma$ sample. Thus, no further corrections are applied.

5.4 Summary

The non-negligible background contributions in the SR of the $ZZ\gamma$ analysis are the non-prompt photon background estimated using a ratio method, the misidentified-lepton contribution derived using a matrix method, and the combinatorial pileup background predicted using a MC overlay. A summary of the background contributions, including the event yields for the various decay channels for each background estimate, is shown in Table 5.11.

Table 5.11: Event yields of the background contributions in the SR for the different decay channels. The 4ℓ channel is the combination of the $4e$, $2e2\mu$, and 4μ channels.

Channel	Background	Number of events
$4e$	Non-prompt Photons	0.135 ± 0.004 (stat.) ± 0.024 (syst.)
	Misidentified Leptons	0.041 ± 0.015 (stat.) ± 0.035 (syst.)
	Pile up	0.012 ± 0.001 (stat.) ± 0.003 (syst.)
	Background	0.193 ± 0.016 (stat.) ± 0.043 (syst.)
$2e2\mu$	Non-prompt Photons	0.343 ± 0.009 (stat.) ± 0.062 (syst.)
	Misidentified Leptons	0.071 ± 0.016 (stat.) ± 0.048 (syst.)
	Pile up	0.043 ± 0.001 (stat.) ± 0.011 (syst.)
	Background	0.471 ± 0.018 (stat.) ± 0.079 (syst.)
4μ	Non-prompt Photons	0.234 ± 0.006 (stat.) ± 0.043 (syst.)
	Misidentified Leptons	0.010 ± 0.004 (stat.) ± 0.005 (syst.)
	Pile up	0.033 ± 0.001 (stat.) ± 0.008 (syst.)
	Background	0.287 ± 0.007 (stat.) ± 0.044 (syst.)
4ℓ	Non-prompt Photons	0.713 ± 0.019 (stat.) ± 0.129 (syst.)
	Misidentified Leptons	0.122 ± 0.022 (stat.) ± 0.078 (syst.)
	Pile up	0.089 ± 0.002 (stat.) ± 0.022 (syst.)
	Background	0.924 ± 0.029 (stat.) ± 0.152 (syst.)

Chapter 6

Results

The cross-section of $ZZ\gamma$ production in the fully leptonic final state is measured. With the signal and background contributions estimated in the SR, the data are unblinded. The signal extraction will be described in Section 6.1, the results will be presented in Section 6.2, and their interpretation will follow in Section 6.3.

6.1 Signal extraction

The number of observed signal events is obtained by subtracting the expected background from the total number of observed events: $N_{\text{sig}} = N_{\text{obs}} - N_{\text{bkg}}$. In the SR, the cross-section at reconstruction level is defined as

$$\sigma^{\text{SR}}_{pp\to 4\ell\gamma} = \frac{N_{\text{sig}}}{\mathcal{L}}, \tag{6.1}$$

with the integrated luminosity $\mathcal{L} = 140.1 \pm 1.2\,\text{fb}^{-1}$. To obtain the result at particle level, independent of detector acceptance and reconstruction efficiencies, we correct the observed signal yield by the correction factor $C = 0.352 \pm 0.005\,(\text{stat.}) \pm 0.009\,(\text{syst.})$, which was determined in Section 4.3.2. The systematic uncertainty on the correction factor is from the experimental uncertainties on the signal MC simulation samples. The fiducial cross-section at particle level is then

$$\sigma^{\text{fid}}_{pp\to 4\ell\gamma} = \frac{N_{\text{sig}}}{C \cdot \mathcal{L}}. \tag{6.2}$$

The significance Z quantifies the probability of obtaining the observed number of events under the background-only hypothesis. In the low-event

count regime (with $N_{\text{obs}} \geq N_{\text{bkg}}$), the significance is calculated as [147]

$$Z = \sqrt{2\left(N_{\text{obs}} \ln\left[\frac{N_{\text{obs}}(N_{\text{bkg}}+\sigma_{\text{bkg}}^2)}{N_{\text{bkg}}^2+N_{\text{obs}}\sigma_{\text{bkg}}^2}\right] - \frac{N_{\text{bkg}}^2}{\sigma_{\text{bkg}}^2}\ln\left[1+\frac{\sigma_{\text{bkg}}^2(N_{\text{obs}}-N_{\text{bkg}})}{N_{\text{bkg}}(N_{\text{bkg}}+\sigma_{\text{bkg}}^2)}\right]\right)} \tag{6.3}$$

To observe the $ZZ\gamma$ final state, the background-only hypothesis needs to be rejected with $Z \geq 5\,\sigma$; to find evidence, $Z \geq 3\,\sigma$ is required.

6.2 Results

The data in the SR are unblinded, yielding eight observed events. This is compatible with the expected total yield of 7.96 ± 0.09 (stat.) $\pm$ 0.23 (syst.). A breakdown of the expected signal, background, and observed number of events is given in Table 6.1. In Fig. 6.1 data and predictions are compared in the different decay channels and for various differential distributions—photon transverse momentum, four-lepton-plus-photon invariant mass, and dilepton invariant mass. In all distributions the data agree well with the prediction.

With the estimated background contribution of $N_{\text{bkg}} = 0.92 \pm 0.15$,

Table 6.1: Overview of the expected number of signal and background events as well as the the observed number of events.

	Number of events
Sherpa 2.2.11 $4\ell\gamma$	6.28 ± 0.09 (stat.) $\pm$ 0.18 (syst.)
PowhegPythia8 $ZH \to ZZ\gamma$	0.76 ± 0.03 (stat.) $\pm$ 0.03 (syst.)
Signal	7.04 ± 0.09 (stat.) $\pm$ 0.18 (syst.)
Fake photons	0.71 ± 0.02 (stat.) $\pm$ 0.13 (syst.)
Fake leptons	0.12 ± 0.02 (stat.) $\pm$ 0.08 (syst.)
Pileup	0.09 ± 0.002 (stat.) $\pm$ 0.02 (syst.)
Total background	0.92 ± 0.03 (stat.) $\pm$ 0.15 (syst.)
N_{tot} prediction	7.96 ± 0.09 (stat.) $\pm$ 0.23 (syst.)
N_{tot} data	8

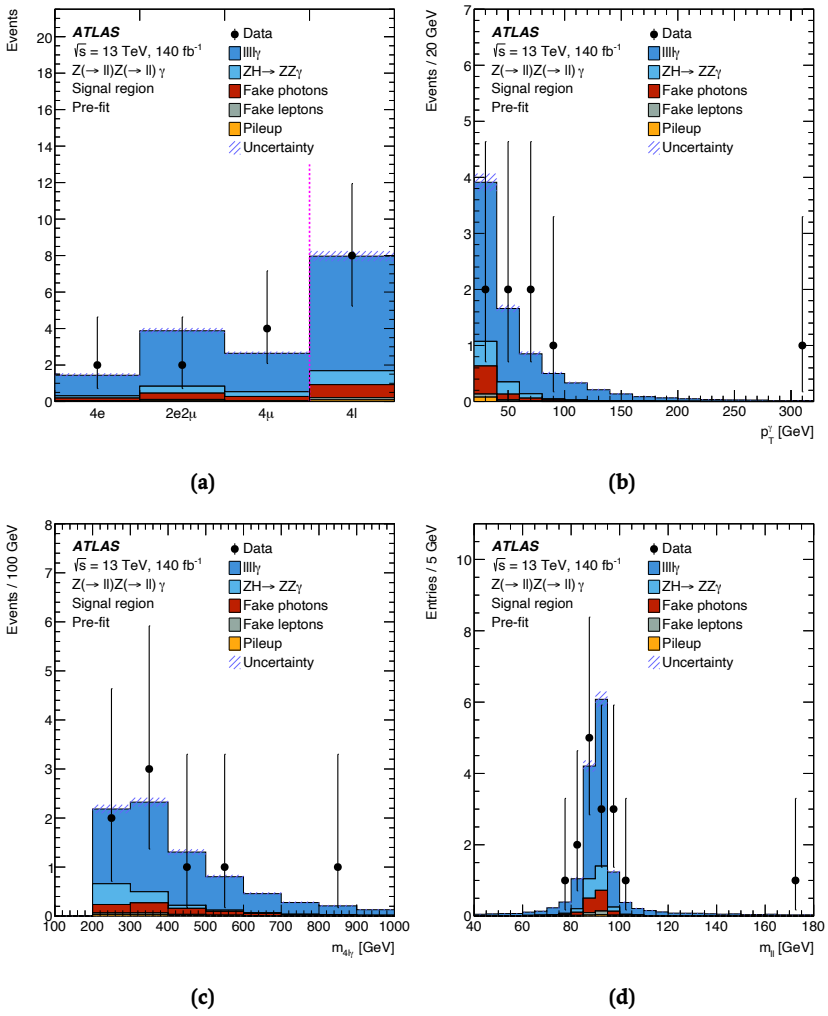


Figure 6.1: Data are compared with the signal and background expectations in the SR. In (a) the event yields are shown in the $4e$, 4μ, $2e2\mu$ and 4ℓ channel, where the 4ℓ channel is the sum of the other three channels, as distinguished by the dashed line. Distribution of (b) the photon transverse momentum p_{T}^{γ}, (c) the four-lepton-plus-photon invariant mass $m_{4\ell\gamma}$, and (d) the dilepton invariant mass $m_{\ell\ell}$, which includes entries from the leading and sub-leading Z boson, taken from [7].

the signal yield is $N_{\text{sig}} = 7.08^{+3.76}_{-2.59}$ (stat.) $\pm$ 0.15 (syst.). Using Eq. (6.3), the background-only hypothesis is rejected with a significance of 4.4σ (expected 4.4σ), resulting in strong evidence of the $ZZ\gamma$ final state. The measured cross-section at reconstruction level is

$$\sigma^{\text{SR}}_{pp\to 4\ell\gamma} = 0.051^{+0.026}_{-0.018}\,(\text{stat.}) \pm 0.001(\text{syst.})\,\text{fb}. \tag{6.4}$$

The statistical uncertainty is propagated from the asymmetric statistical uncertainty in N_{sig}. The systematic uncertainties are from the background estimate and the uncertainty in the luminosity.

Applying the correction factor C, the fiducial cross-section at particle level is[1]

$$\sigma^{\text{fid}}_{pp\to 4\ell\gamma} = 0.144^{+0.077}_{-0.053}\,(\text{stat.}) \pm 0.005\,(\text{syst.})\,\text{fb}. \tag{6.5}$$

This measurement is in agreement with the SM prediction, $\sigma^{\text{fid}}_{\text{SM}} = 0.143 \pm 0.001\,(\text{stat.}) \pm 0.005\,(\text{theo.})\,\text{fb}$, which is obtained from the two signal MC simulation samples ($4\ell\gamma$ and $ZH \to ZZ\gamma$). The total uncertainty is dominated by the statistical component (40%) due to the limited event count; systematic uncertainties (4%) arise mainly from experimental uncertainties and background modelling.

6.3 Interpretation and discussion

The measured fiducial cross-section is in good agreement with the SM electroweak prediction for triple-gauge-boson production. The result is statistics-limited and, with only eight observed events, one of the smallest cross-sections measured at the LHC.

For all distributions in Fig. 6.1 the data agree well with the SM expectations. Two isolated outliers are present: a single event with a high photon transverse momentum and one entry with a high dilepton invariant mass. However, the number of expected events for a photon with transverse momentum above 120 GeV is $N(p_{\text{T}}^{\gamma} > 120\,\text{GeV}) = 1.00$ and the number of expected entries for a dilepton invariant mass above 120 GeV is

[1] The statistical uncertainty on the fiducial cross-section differs from that reported in Ref. [7] due to different methods to determine the statistical uncertainty on N_{sig}. Here, we use the χ^2 inversion method to obtain the 68% confidence interval. In Ref. [7], a profile-likelihood-ratio test statistic in the asymptotic approximation [148] is performed.

$N(m_{\ell\ell} > 120\,\text{GeV}) = 1.39$. Given the total of eight observed events, these are compatible with statistical fluctuations.

The analysis provides strong evidence of the $ZZ\gamma$ production, with the limited event yield being the obstacle to observation. Assuming the same signal-to-background ratio and relative number of observed events, the current ATLAS Run 3 dataset (2022–2025) with an integrated luminosity of $300\,\text{fb}^{-1}$ [149] would yield: $N_{\text{obs}} \simeq 17$, $N_{\text{sig}} \simeq 15$, and $N_{\text{bkg}} \simeq 2.0$ with 16% relative uncertainty. With these numbers the background-only hypothesis would be rejected with a significance well above 6σ. Looking even further ahead, the HL-LHC era will enable differential cross-section measurements, testing the SM even further.

The $ZZ\gamma$ final state has future physics potential. In the SM, the tree-level $ZZ\gamma$ production does not contain any triple- or quartic-gauge vertices; fully neutral triple- or quartic-gauge couplings are forbidden. Consequently, this final state is an excellent probe of anomalous neutral gauge couplings, e. g., via dimension-8 operators in an effective field theory framework [150, 151]. At present, the $Z\gamma\gamma$ final state offers higher sensitivity because of its larger event yield. However, with increased statistics, the $ZZ\gamma$ final state will become competitive or even superior. Its advantages relative to the $Z\gamma\gamma$ final state are the sensitivity to the $ZZZ\gamma$ interaction (no sensitivity for $Z\gamma\gamma$) and the lower background fraction (this analysis: 12%, $Z\gamma\gamma$: 29% [34]).

A precise measurement of the $ZZ\gamma$ final state is also important for the Higgs boson program, especially for the Higgs to $Z\gamma$ decay. Current analyses are targeting the vector-boson fusion production of the Higgs boson to find evidence of $H \to Z\gamma$ [152]. With more data, the ZH associated-production channel with a fully leptonic final state will be a clean channel to measure the $H \to Z\gamma$ branching ratio. In this channel, the direct production of $ZZ\gamma$ will be the dominant background. Reducing the uncertainty on this background will directly increase the discovery potential for $H \to Z\gamma$.

Beyond the specific physics cases, this analysis demonstrates that backgrounds can be constrained in high-statistics CRs and reliably extrapolated to low-statistics SRs, yielding a low background uncertainty. Such a strategy is essential for any search that relies on a background-only hypothesis test.

In summary, the present result constitutes the first evidence of the $ZZ\gamma$

final state. It is a stepping stone for a future observation, for tests of neutral gauge-boson couplings, and for a measurement of the $H \to Z\gamma$ branching ratio. The methodology and the achieved background precision are also applicable to other analyses that are limited by low event yields.

Chapter 7

Conclusion

The simultaneous production of two Z bosons and a photon ($ZZ\gamma$) is an electroweak process that probes the non-abelian gauge-boson self-interactions. We have performed the first cross-section measurement of $ZZ\gamma$ production in the four-lepton-plus-photon final state using the ATLAS full Run 2 dataset ($\sqrt{s} = 13\,\text{TeV}$, $140\,\text{fb}^{-1}$). We selected two opposite-sign same-flavor lepton pairs and an isolated photon with a transverse momentum of $p_{\text{T}}^{\gamma} > 20\,\text{GeV}$. A dedicated veto against photon final-state radiation significantly suppressed its contribution.

The main background contributions were estimated with data-driven techniques. For the non-prompt photon background, we developed a new ratio method that extrapolates from the high-statistics $Z\gamma$ control region. With this method, the non-prompt photon background yield was estimated as 0.71 ± 0.13 events. We expanded the matrix method to a four-lepton final state, resulting in a misidentified lepton background yield of 0.12 ± 0.08 events.

After the selection, eight candidate events were observed with an expected background contribution of 0.92 ± 0.15 events. The background-only hypothesis is rejected with a significance of 4.4σ, providing the first experimental evidence of $ZZ\gamma$ production. The fiducial cross-section at particle level is measured as $\sigma_{ZZ\gamma}^{\text{fid}} = 0.144^{+0.077}_{-0.053}\,\text{fb}$, in excellent agreement with the Standard Model prediction of $0.143 \pm 0.005\,\text{fb}$. This test of the Standard Model confirms the non-abelian structure of the electroweak sector.

In conclusion, this analysis results in the first $ZZ\gamma$ cross-section measurement, demonstrates strong evidence of this process, and provides a foundation for future triple-gauge-boson measurements and searches for new physics.

References

[1] ATLAS Collaboration, "Observation of a new particle in the search for the Standard Model Higgs boson with the ATLAS detector at the LHC," *Physics Letters B*, vol. 716, no. 1, pp. 1–29, Sep. 2012. [Online]. Available: http://arxiv.org/abs/1207.7214 (visited on 2025-04-29).

[2] CMS Collaboration, "Observation of a new boson at a mass of 125 GeV with the CMS experiment at the LHC," *Physics Letters B*, vol. 716, no. 1, pp. 30–61, Sep. 2012. [Online]. Available: http://arxiv.org/abs/1207.7235 (visited on 2025-04-29).

[3] M. E. Peskin and D. V. Schroeder, *An Introduction to Quantum Field Theory*. Boca Raton: CRC Press, 2018.

[4] M. Thomson, *Modern Particle Physics*. Cambridge: Cambridge University Press, 2013.

[5] L. Evans and P. Bryant, "LHC Machine," *Journal of Instrumentation*, vol. 3, Aug. 2008. [Online]. Available: https://iopscience.iop.org/article/10.1088/1748-0221/3/08/S08001.

[6] ATLAS Collaboration, "The ATLAS Experiment at the CERN Large Hadron Collider," *Journal of Instrumentation*, vol. 3, no. 08, S08003, Aug. 2008. [Online]. Available: https://iopscience.iop.org/article/10.1088/1748-0221/3/08/S08003 (visited on 2025-04-25).

[7] ATLAS Collaboration. "Evidence of $ZZ\gamma$ production with the ATLAS detector." (Feb. 19, 2026), [Online]. Available: http://arxiv.org/abs/2602.17165 (visited on 2026-02-20), pre-published.

[8] G. 't Hooft, "Renormalizable Lagrangians for massive Yang-Mills fields," *Nuclear Physics B*, vol. 35, no. 1, pp. 167–188, Dec. 1971. [Online]. Available: https://linkinghub.elsevier.com/retrieve/pii/0550321371901398 (visited on 2025-04-29).

[9] J. I. Illana and A. J. Cano, "Quantum field theory and the structure of the Standard Model," *PoS*, vol. CORFU2021, 2022.

[10] A. Banfi *et al.*, "Lecture notes for the 2017 School for Experimental High Energy Physics Students," University of Lancaster, Technical Report RAL-TR-2017-009, 2017.

[11] A. V. Bednyakov, "Quantum field theory and the Electroweak Standard Model," *CERN Yellow Reports: School Proceedings*, vol. 6, pp. 1–41, 2019. [Online]. Available: https://e-publishing.cern.ch/index.php/CYRSP/article/view/934 (visited on 2025-04-29).

[12] P. Langacker, *The Standard Model and Beyond*, 2nd ed. CRC Press, 2017. [Online]. Available: https://doi.org/10.1201/b22175 (visited on 2025-04-29).

[13] "Standard Model – TikZ.net." (Sep. 26, 2023), [Online]. Available: https://tikz.net/sm_particles/ (visited on 2025-10-27).

[14] R. Jimenez *et al.*, "Neutrino masses and mass hierarchy: Evidence for the normal hierarchy," *Journal of Cosmology and Astroparticle Physics*, vol. 2022, no. 09, p. 006, Sep. 1, 2022. [Online]. Available: https://doi.org/10.1088/1475-7516/2022/09/006 (visited on 2025-04-29).

[15] A. Pich. "The Standard Model of Electroweak Interactions." (2007), [Online]. Available: http://arxiv.org/abs/0705.4264 (visited on 2025-04-29), pre-published.

[16] D. Denegri, "The discovery of the W and Z," *Physics Reports*, vol. 403–404, pp. 107–145, 2004. [Online]. Available: https://doi.org/10.1016/j.physrep.2004.09.006 (visited on 2025-04-29).

[17] P. W. Higgs, "Broken Symmetries and the Masses of Gauge Bosons," *Physical Review Letters*, vol. 13, no. 16, pp. 508–509, Oct. 19, 1964. [Online]. Available: https://link.aps.org/doi/10.1103/PhysRevLett.13.508 (visited on 2025-04-29).

[18] F. Englert and R. Brout, "Broken Symmetry and the Mass of Gauge Vector Mesons," *Physical Review Letters*, vol. 13, no. 9, pp. 321–323, Aug. 31, 1964. [Online]. Available: https://link.aps.org/doi/10.1103/PhysRevLett.13.321 (visited on 2025-04-29).

[19] S. Weinberg, "A Model of Leptons," *Physical Review Letters*, vol. 19, no. 21, pp. 1264–1266, Nov. 20, 1967. [Online]. Available: https://link.aps.org/doi/10.1103/PhysRevLett.19.1264 (visited on 2025-04-29).

[20] A. Salam and J. C. Ward, "Weak and electromagnetic interactions," *Il Nuovo Cimento (1955-1965)*, vol. 11, no. 4, pp. 568–577, Feb. 1, 1959. [Online]. Available: https://doi.org/10.1007/BF02726525.

[21] S. L. Glashow, "Partial-symmetries of weak interactions," *Nuclear Physics*, vol. 22, no. 4, pp. 579–588, Feb. 1, 1961. [Online]. Available: https://doi.org/10.1016/0029-5582(61)90469-2 (visited on 2025-04-29).

[22] J. Goldstone, A. Salam, and S. Weinberg, "Broken Symmetries," *Physical Review*, vol. 127, no. 3, pp. 965–970, Aug. 1, 1962. [Online]. Available: https://link.aps.org/doi/10.1103/PhysRev.127.965 (visited on 2025-04-29).

[23] N. Cabibbo, "Unitary Symmetry and Leptonic Decays," *Physical Review Letters*, vol. 10, no. 12, pp. 531–533, Jun. 15, 1963. [Online]. Available: https://doi.org/10.1103/PhysRevLett.10.531 (visited on 2025-04-29).

[24] M. Kobayashi and T. Maskawa, "CP-Violation in the Renormalizable Theory of Weak Interaction," *Progress of Theoretical Physics*, vol. 49, no. 2, pp. 652–657, Feb. 1, 1973. [Online]. Available: https://doi.org/10.1143/PTP.49.652 (visited on 2025-11-24).

[25] Y. Grossman. "Introduction to Flavour Physics." E. Gardi, N. Glover, and A. Robson, Eds. (2014), [Online]. Available: https://cds.cern.ch/record/1272886 (visited on 2025-09-03), pre-published.

[26] J. Ellis *et al.*, "Top, Higgs, Diboson and Electroweak Fit to the Standard Model Effective Field Theory," *Journal of High Energy Physics*, vol. 2021, no. 4, p. 279, Apr. 2021. [Online]. Available: http://arxiv.org/abs/2012.02779 (visited on 2025-04-29).

[27] R. Bellan *et al.*, "A sensitivity study of triboson production processes to dimension-6 EFT operators at the LHC," *Journal of High Energy Physics*, vol. 2023, no. 158, Aug. 2023. [Online]. Available: https://link.springer.com/10.1007/JHEP08(2023)158 (visited on 2026-01-06).

[28] B. W. Lee, C. Quigg, and H. B. Thacker, "Strength of Weak Interactions at Very High Energies and the Higgs Boson Mass," *Physical Review Letters*, vol. 38, no. 16, pp. 883–885, Apr. 1977. [Online]. Available: https://link.aps.org/doi/10.1103/PhysRevLett.38.883 (visited on 2026-01-06).

[29] B. W. Lee, C. Quigg, and H. B. Thacker, "Weak interactions at very high energies: The role of the Higgs-boson mass," *Physical Review D*, vol. 16, no. 5, pp. 1519–1531, Sep. 1977. [Online]. Available: https://link.aps.org/doi/10.1103/PhysRevD.16.1519 (visited on 2026-01-06).

[30] ATLAS Collaboration, "Observation of WWW Production in pp Collisions at $\sqrt{s} = 13$ TeV with the ATLAS Detector," *Physical Review Letters*, vol. 129, no. 6, p. 061 803, Aug. 4, 2022. [Online]. Available: https://link.aps.org/doi/10.1103/PhysRevLett.129.061803 (visited on 2025-04-29).

[31] ATLAS Collaboration, "Observation of VVZ production at $\sqrt{s} = 13$ TeV with the ATLAS detector," *Physics Letters B*, vol. 866, p. 139 527, Jul. 2025. [Online]. Available: https://doi.org/10.1016/j.physletb.2025.139527 (visited on 2025-11-13).

[32] ATLAS Collaboration, "Observation of $W\gamma\gamma$ triboson production in proton-proton collisions at $\sqrt{s} = 13$ TeV with the ATLAS detector," *Physics Letters B*, vol. 848, p. 138 400, Jan. 2024. [Online]. Available: https://doi.org/10.1016/j.physletb.2023.138400 (visited on 2025-11-13).

[33] ATLAS Collaboration, "Observation of $WZ\gamma$ Production in pp Collisions at $\sqrt{s} = 13$ TeV with the ATLAS Detector," *Physical Review Letters*, vol. 132, no. 2, p. 021 802, Jan. 12, 2024. [Online]. Available: https://link.aps.org/doi/10.1103/PhysRevLett.132.021802 (visited on 2025-11-13).

[34] ATLAS Collaboration, "Measurement of $Z\gamma\gamma$ Production in pp Collisions at $\sqrt{s} = 13$ TeV with the ATLAS detector," *The European Physical Journal C*, vol. 83, no. 6, p. 539, Jun. 27, 2023. [Online]. Available: https://doi.org/10.1140/epjc/s10052-023-11579-8 (visited on 2025-04-29).

[35] ATLAS Collaboration, "Standard Model Summary Plots June 2024," CERN, Geneva, ATL-PHYS-PUB-2024-011, 2024. [Online]. Available: https://cds.cern.ch/record/2903866.

[36] J. T. Boyd, "LHC Run-2 and Future Prospects," 2021. [Online]. Available: https://cds.cern.ch/record/2707815 (visited on 2025-05-09).

[37] S. Baird, "Accelerators for pedestrians," CERN, Geneva, CERN-AB-Note-2007-014, 2007. [Online]. Available: https://cds.cern.ch/record/1017689 (visited on 2025-04-25).

[38] ALICE Collaboration, "The ALICE experiment at the CERN LHC," *Journal of Instrumentation*, vol. 3, no. 08, S08002, Aug. 2008. [Online]. Available: https://dx.doi.org/10.1088/1748-0221/3/08/S08002 (visited on 2025-05-14).

[39] CMS Collaboration, "The CMS experiment at the CERN LHC," *Journal of Instrumentation*, vol. 3, no. 08, S08004, Aug. 2008. [Online]. Available: https://iopscience.iop.org/article/10.1088/1748-0221/3/08/S08004 (visited on 2025-05-14).

[40] LHCb Collaboration, "The LHCb Detector at the LHC," *Journal of Instrumentation*, vol. 3, no. 08, S08005, Aug. 2008. [Online]. Available: https://iopscience.iop.org/article/10.1088/1748-0221/3/08/S08005 (visited on 2025-05-14).

[41] O. S. Brüning *et al.*, *LHC Design Report* (CERN Yellow Reports: Monographs). Geneva: CERN, 2004. [Online]. Available: https://cds.cern.ch/record/782076 (visited on 2025-04-25).

[42] E. Lopienska, *The CERN accelerator complex, layout in 2022*, 2022. [Online]. Available: https://cds.cern.ch/record/2800984 (visited on 2025-09-03).

[43] M. Vretenar *et al.*, *Linac4 Design Report* (CERN Yellow Reports: Monographs). Geneva: CERN, 2020, vol. 6. [Online]. Available: https://cds.cern.ch/record/2736208 (visited on 2025-04-25).

[44] "Linear accelerator 2," CERN. (2025), [Online]. Available: https://home.cern/science/accelerators/linear-accelerator-2 (visited on 2025-05-13).

[45] E. Halkiadakis. "Proceedings for TASI 2009 Summer School on "Physics of the Large and the Small": Introduction to the LHC experiments." (2010), [Online]. Available: http://arxiv.org/abs/1004.5564 (visited on 2025-04-25), pre-published.

[46] O. Aberle *et al.*, *High-Luminosity Large Hadron Collider (HL-LHC): Technical Design Report* (CERN Yellow Reports: Monographs). Geneva: CERN, 2020. [Online]. Available: https://cds.cern.ch/record/2749422 (visited on 2025-04-25).

[47] "Project Schedule | HL-LHC Industry." (2025), [Online]. Available: https://project-hl-lhc-industry.web.cern.ch/content/project-schedule (visited on 2025-05-14).

[48] H. Bartosik *et al.*, "Injectors Beam Performance Evolution during Run 2," 2019. [Online]. Available: https://cds.cern.ch/record/2750276 (visited on 2025-04-25).

[49] P. Grafström and W. Kozanecki, "Luminosity determination at proton colliders," *Progress in Particle and Nuclear Physics*, vol. 81, pp. 97–148, 2015. [Online]. Available: https://doi.org/10.1016/j.ppnp.2014.11.002 (visited on 2025-04-30).

[50] W. Herr and B. Muratori, "Concept of luminosity," 2006. [Online]. Available: https://cds.cern.ch/record/941318 (visited on 2025-04-30).

[51] ATLAS Collaboration, *ATLAS Detector and Physics Performance* (Technical Design Report. ATLAS). Geneva: CERN, 1999. [Online]. Available: https://cds.cern.ch/record/391176 (visited on 2025-04-25).

[52] ATLAS Collaboration, "Operation of the ATLAS trigger system in Run 2," *Journal of Instrumentation*, vol. 15, no. 10, Oct. 2020. [Online]. Available: https://iopscience.iop.org/article/10.1088/1748-0221/15/10/P10004 (visited on 2025-04-25).

[53] G. Avoni *et al.*, "The new LUCID-2 detector for luminosity measurement and monitoring in ATLAS," *Journal of Instrumentation*, vol. 13, no. 07, Jul. 2018. [Online]. Available: https://iopscience.iop.org/article/10.1088/1748-0221/13/07/P07017 (visited on 2025-04-25).

[54] S. Abdel Khalek *et al.*, "The ALFA Roman Pot detectors of ATLAS," *Journal of Instrumentation*, vol. 11, no. 11, Nov. 2016. [Online]. Available: https://iopscience.iop.org/article/10.1088/1748-0221/11/11/P11013 (visited on 2025-04-25).

[55] R. M. Bianchi and ATLAS Collaboration, *Images from the paper: "The ATLAS Experiment at the CERN Large Hadron Collider: A Description of the Detector Configuration for Run 3*, 2024. [Online]. Available: https://cds.cern.ch/record/2900788 (visited on 2025-09-03).

[56] ATLAS Collaboration, *ATLAS Magnet System* (Technical Design Report. ATLAS). Geneva: CERN, 1997. [Online]. Available: https://cds.cern.ch/record/338080 (visited on 2025-04-30).

[57] A. Yamamoto *et al.*, "The ATLAS central solenoid," *Nuclear Instruments and Methods in Physics Research Section A: Accelerators, Spectrometers, Detectors and Associated Equipment*, vol. 584, no. 1, pp. 53–74, Jan. 2008. [Online]. Available: https://doi.org/10.1016/j.nima.2007.09.047 (visited on 2025-04-25).

[58] J. P. Badiou *et al.*, *ATLAS Barrel Toroid* (Technical Design Report. ATLAS). Geneva: CERN, 1997. [Online]. Available: https://cds.cern.ch/record/331065 (visited on 2025-04-30).

[59] S. Haywood *et al.*, *ATLAS Inner Detector* (Technical Design Report. ATLAS). Geneva: CERN, 1997. [Online]. Available: https://cds.cern.ch/record/331064 (visited on 2025-04-30).

[60] H. Pernegger, "The Pixel Detector of the ATLAS experiment for LHC Run-2," *Journal of Instrumentation*, vol. 10, no. 06, p. C06012, Jun. 2015. [Online]. Available: https://iopscience.iop.org/article/10.1088/1748-0221/10/06/C06012 (visited on 2025-04-25).

[61] ATLAS Collaboration, "Operation and performance of the ATLAS semiconductor tracker in LHC Run 2," *Journal of Instrumentation*, vol. 17, no. 01, P01013, Jan. 2022. [Online]. Available: http://dx.doi.org/10.1088/1748-0221/17/01/P01013 (visited on 2025-04-25).

[62] A. Vogel, "ATLAS Transition Radiation Tracker (TRT): Straw tube gaseous detectors at high rates," *Nuclear Instruments and Methods in Physics Research Section A: Accelerators, Spectrometers, Detectors and Associated Equipment*, vol. 732, pp. 277–280, Jul. 2013. [Online]. Available: https://doi.org/10.1016/j.nima.2013.07.020 (visited on 2025-04-25).

[63] ATLAS TRT Collaboration, "The ATLAS TRT Barrel Detector," *Journal of Instrumentation*, vol. 3, no. 02, P02014, Feb. 2008. [Online]. Available: https://iopscience.iop.org/article/10.1088/1748-0221/3/02/P02014 (visited on 2025-04-25).

[64] ATLAS TRT Collaboration, "The ATLAS TRT end-cap detectors," *Journal of Instrumentation*, vol. 3, no. 10, P10003, Oct. 2008. [Online]. Available: https://iopscience.iop.org/article/10.1088/1748-0221/3/10/P10003 (visited on 2025-04-25).

[65] F. Cavallari, "Performance of calorimeters at the LHC," *Journal of Physics: Conference Series*, vol. 293, p. 012 001, Apr. 2011. [Online]. Available: https://doi.org/10.1088/1742-6596/293/1/012001 (visited on 2025-04-25).

[66] ATLAS Collaboration, *ATLAS Liquid-Argon Calorimeter* (Technical Design Report. ATLAS). Geneva: CERN, 1996. [Online]. Available: https://cds.cern.ch/record/331061 (visited on 2025-04-30).

[67] ATLAS Collaboration, "Operation and performance of the ATLAS tile calorimeter in LHC Run 2," *The European Physical Journal C*, vol. 84, no. 12, p. 1313, Dec. 2024. [Online]. Available: https://doi.org/10.1140/epjc/s10052-024-13151-4 (visited on 2025-09-01).

[68] T. Barillari, "The ATLAS liquid argon hadronic end-cap calorimeter: Construction and selected beam test results," *Nuclear Physics B - Proceedings Supplements*, vol. 150, pp. 102–105, 2006. [Online]. Available: https://doi.org/10.1016/j.nuclphysbps.2004.10.087 (visited on 2025-04-25).

[69] ATLAS Collaboration, *ATLAS Muon Spectrometer* (Technical Design Report. ATLAS). Geneva: CERN, 1997. [Online]. Available: https://cds.cern.ch/record/331068 (visited on 2025-04-30).

[70] P. Jenni *et al.*, *ATLAS High-Level Trigger, Data-Acquisition and Controls* (Technical Design Report. ATLAS). Geneva: CERN, 2003. [Online]. Available: https://cds.cern.ch/record/616089 (visited on 2025-04-30).

[71] W. Buttinger, "The ATLAS Level-1 Trigger System," *Journal of Physics: Conference Series*, vol. 396, no. 1, p. 012 010, Dec. 2012. [Online]. Available: https://iopscience.iop.org/article/10.1088/1742-6596/396/1/012010 (visited on 2025-04-25).

[72] R. Frühwirth, "Application of Kalman filtering to track and vertex fitting," *Nuclear Instruments and Methods in Physics Research Section A: Accelerators, Spectrometers, Detectors and Associated Equipment*, vol. 262, no. 2, pp. 444–450, 1987. [Online]. Available: https://doi.org/10.1016/0168-9002(87)90887-4.

[73] ATLAS Collaboration, "Electron and photon efficiencies in LHC Run 2 with the ATLAS experiment," *Journal of High Energy Physics*, vol. 2024, no. 162, May 2024. [Online]. Available: http://arxiv.org/abs/2308.13362 (visited on 2025-11-24).

[74] ATLAS Collaboration, "Muon reconstruction and identification efficiency in ATLAS using the full Run 2 *pp* collision data set at $\sqrt{s} = 13$ TeV," *The European Physical Journal C*, vol. 81, no. 578, Jul. 2021. [Online]. Available: http://arxiv.org/abs/2012.00578 (visited on 2025-11-12).

[75] M. Cacciari, G. P. Salam, and G. Soyez, "The anti-k_t jet clustering algorithm," *Journal of High Energy Physics*, vol. 2008, no. 04, p. 063, Apr. 2008. [Online]. Available: https://iopscience.iop.org/article/10.1088/1126-6708/2008/04/063 (visited on 2025-11-24).

[76] M. Cacciari, G. P. Salam, and G. Soyez, "FastJet user manual," *The European Physical Journal C*, vol. 72, no. 1896, Mar. 2012. [Online]. Available: http://arxiv.org/abs/1111.6097 (visited on 2025-12-04).

[77] ATLAS Collaboration, "Jet energy scale and resolution measured in proton-proton collisions at $\sqrt{s} = 13$ TeV with the ATLAS detector," *The European Physical Journal C*, vol. 81, no. 689, Aug. 2021. [Online]. Available: http://arxiv.org/abs/2007.02645 (visited on 2025-04-25).

[78] R. Frühwirth and A. Strandlie, "Vertex Finding," in *Pattern Recognition, Tracking and Vertex Reconstruction in Particle Detectors*, Cham: Springer, 2021, pp. 131–141. [Online]. Available: https://doi.org/10.1007/978-3-030-65771-0_7 (visited on 2025-12-11).

[79] S. Boutle *et al.*, "Primary vertex reconstruction at the ATLAS experiment," *Journal of Physics: Conference Series*, vol. 898, p. 042 056, Oct. 2017. [Online]. Available: https://iopscience.iop.org/article/10.1088/1742-6596/898/4/042056 (visited on 2025-04-25).

[80] ATLAS Collaboration, "Vertex Reconstruction Performance of the ATLAS Detector at $\sqrt{s} = 13$ TeV," CERN, Geneva, ATL-PHYS-PUB-2015-026, 2015. [Online]. Available: https://cds.cern.ch/record/2037717 (visited on 2025-04-30).

[81] ATLAS Collaboration, "Performance of pile-up mitigation techniques for jets in *pp* collisions at $\sqrt{s} = 8$ TeV using the ATLAS detector," *The European Physical Journal C*, vol. 76, no. 581, Oct. 2016. [Online]. Available: http://arxiv.org/abs/1510.03823 (visited on 2025-11-24).

[82] ATLAS Collaboration, "Electron and photon performance measurements with the ATLAS detector using the 2015-2017 LHC proton-proton collision data," *Journal of Instrumentation*, vol. 14, no. 12, P12006, Dec. 2019. [Online]. Available: http://arxiv.org/abs/1908.00005 (visited on 2025-11-12).

[83] ATLAS Collaboration, "Electron and photon energy calibration with the ATLAS detector using LHC Run 2 data," *Journal of Instrumentation*, vol. 19, no. 02, P02009, Feb. 2024. [Online]. Available: http://arxiv.org/abs/2309.05471 (visited on 2025-11-12).

[84] ATLAS Collaboration, "Electron and photon energy calibration with the ATLAS detector using 2015-2016 LHC proton-proton collision data," *Journal of Instrumentation*, vol. 14, no. 03, P03017, Mar. 2019. [Online]. Available: http://arxiv.org/abs/1812.03848 (visited on 2025-11-12).

[85] ATLAS Collaboration, "Measurement of the photon identification efficiencies with the ATLAS detector using LHC Run 2 data collected in 2015 and 2016," *The European Physical Journal C*, vol. 79, no. 205, Mar. 2019. [Online]. Available: http://arxiv.org/abs/1810.05087 (visited on 2026-01-08).

[86] J. Illingworth and J. Kittler, "A Survey of the Hough Transform," *Computer Vision, Graphics, and Image Processing*, vol. 44, no. 1, pp. 87–116, 1988. [Online]. Available: https://doi.org/10.1016/S0734-189X(88)80033-1.

[87] ATLAS Collaboration, "Muon reconstruction performance of the ATLAS detector in proton–proton collision data at $\sqrt{s} = 13$ TeV," *The European Physical Journal C*, vol. 76, no. 292, May 2016. [Online]. Available: http://arxiv.org/abs/1603.05598 (visited on 2025-11-12).

[88] H. E. Herde, "Muon reconstruction performance in ATLAS at Run-II," in *Proceedings of The European Physical Society Conference on High Energy Physics — PoS(EPS-HEP2015)*, Vienna, Austria: Sissa Medialab, Mar. 16, 2016, p. 285. [Online]. Available: https://pos.sissa.it/234/285 (visited on 2025-04-25).

[89] F. Anselmo *et al.*, "Event generators for LHC," 1990. [Online]. Available: https://cds.cern.ch/record/220309.

[90] S. Höche. "Introduction to parton-shower event generators." (Jun. 2015), [Online]. Available: http://arxiv.org/abs/1411.4085 (visited on 2025-03-14), pre-published.

[91] D. E. Soper, "Parton distribution functions," *Nuclear Physics B - Proceedings Supplements*, vol. 53, no. 1, pp. 69–80, 1997. [Online]. Available: https://doi.org/10.1016/S0920-5632(96)00600-7.

[92] A. D. Martin *et al.*, "Parton distributions for the LHC," *The European Physical Journal C*, vol. 63, no. 2, pp. 189–285, Jul. 2009. [Online]. Available: http://arxiv.org/abs/0901.0002 (visited on 2025-04-29).

[93] NNPDF Collaboration, "Parton distributions from high-precision collider data," *The European Physical Journal C*, vol. 77, no. 10, p. 663, Oct. 2017. [Online]. Available: http://arxiv.org/abs/1706.00428 (visited on 2025-04-29).

[94] S. Höche, "Status of Monte-Carlo event generators," presented at the 19th International Workshop on Deep-Inelastic Scattering and Related Subjects, Newport News, VA, United States, Aug. 2011. [Online]. Available: https://www.slac.stanford.edu/pubs/slacpubs/14250/slac-pub-14498.pdf.

[95] E. Bothmann *et al.*, "Event Generation with Sherpa 2.2," *SciPost Physics*, vol. 7, no. 3, p. 034, Sep. 2019. [Online]. Available: http://arxiv.org/abs/1905.09127 (visited on 2025-03-14).

[96] T. Sjöstrand and M. van Zijl, "A multiple-interaction model for the event structure in hadron collisions," *Physical Review D*, vol. 36, no. 7, pp. 2019–2041, Oct. 1987. [Online]. Available: https://link.aps.org/doi/10.1103/PhysRevD.36.2019 (visited on 2025-12-23).

[97] B. Andersson *et al.*, "Parton fragmentation and string dynamics," *Physics Reports*, vol. 97, no. 2–3, pp. 31–145, Jul. 1983. [Online]. Available: https://linkinghub.elsevier.com/retrieve/pii/0370157383900807 (visited on 2025-12-19).

[98] B. Andersson, *The Lund Model*. Cambridge University Press, 1998, vol. 7. [Online]. Available: https://doi.org/10.1017/9781009401296.

[99] T. D. Gottschalk, "A realistic model for e+e– annihilation including parton bremsstrahlung effects," *Nuclear Physics B*, vol. 214, no. 2, pp. 201–222, Apr. 1983. [Online]. Available: https://doi.org/10.1016/0550-3213(83)90658-2 (visited on 2025-12-19).

[100] T. D. Gottschalk, "An improved description of hadronization in the QCD cluster model for e+e– annihilation," *Nuclear Physics B*, vol. 239, no. 2, pp. 349–381, Jul. 1984. [Online]. Available: https://doi.org/10.1016/0550-3213(84)90253-0 (visited on 2025-12-19).

[101] T. D. Gottschalk and D. A. Morris, "A new model for hadronization and e+e– annihilation," *Nuclear Physics B*, vol. 288, pp. 729–781, 1987. [Online]. Available: https://doi.org/10.1016/0550-3213(87)90236-7 (visited on 2025-12-19).

[102] J. M. Campbell *et al.* "Event Generators for High-Energy Physics Experiments." (Feb. 2025), [Online]. Available: http://arxiv.org/abs/2203.11110 (visited on 2025-12-12), pre-published.

[103] S. Agostinelli *et al.*, "Geant4—a simulation toolkit," *Nuclear Instruments and Methods in Physics Research Section A: Accelerators, Spectrometers, Detectors and Associated Equipment*, vol. 506, no. 3, pp. 250–303, Jul. 2003. [Online]. Available: https://doi.org/10.1016/S0168-9002(03)01368-8 (visited on 2025-11-24).

[104] ATLAS Collaboration, "The ATLAS Simulation Infrastructure," *The European Physical Journal C*, vol. 70, no. 3, pp. 823–874, Sep. 2010. [Online]. Available: http://arxiv.org/abs/1005.4568 (visited on 2025-04-25).

[105] C. Grojean, "Higgs Physics," *CERN Yellow Reports*, 143 Pages, Dec. 21, 2016. [Online]. Available: https://e-publishing.cern.ch/index.php/CYR/article/view/435 (visited on 2026-01-05).

[106] LHC Higgs Cross Section Working Group. "Handbook of LHC Higgs Cross Sections: 4. Deciphering the Nature of the Higgs Sector." (May 18, 2017), [Online]. Available: http://arxiv.org/abs/1610.07922 (visited on 2025-04-29), pre-published.

[107] ATLAS Collaboration, "ATLAS data quality operations and performance for 2015-2018 data-taking," *Journal of Instrumentation*, vol. 15, no. 04, P04003–P04003, Apr. 2020. [Online]. Available: http://arxiv.org/abs/1911.04632 (visited on 2025-11-12).

[108] ATLAS Collaboration, "Performance of electron and photon triggers in ATLAS during LHC Run 2," *The European Physical Journal C*, vol. 80, no. 47, Jan. 2020. [Online]. Available: http://arxiv.org/abs/1909.00761 (visited on 2025-11-12).

[109] ATLAS Collaboration, "Performance of the ATLAS muon triggers in Run 2," *Journal of Instrumentation*, vol. 15, no. 09, P09015–P09015, Sep. 2020. [Online]. Available: https://iopscience.iop.org/article/10.1088/1748-0221/15/09/P09015 (visited on 2025-04-25).

[110] ATLAS Collaboration, "Electron reconstruction and identification in the ATLAS experiment using the 2015 and 2016 LHC proton–proton collision data at $\sqrt{s} = 13$ TeV," *The European Physical Journal C*, vol. 79, no. 639, Aug. 2019. [Online]. Available: http://link.springer.com/10.1140/epjc/s10052-019-7140-6 (visited on 2026-02-11).

[111] ATLAS Collaboration, "Jet reconstruction and performance using particle flow with the ATLAS Detector," *The European Physical Journal C*, vol. 77, no. 466, Jul. 2017. [Online]. Available: http://arxiv.org/abs/1703.10485 (visited on 2026-02-03).

[112] Particle Data Group, "Review of Particle Physics," *Progress of Theoretical and Experimental Physics*, vol. 2020, no. 8, p. 083C01, Aug. 2020. [Online]. Available: https://academic.oup.com/ptep/article/doi/10.1093/ptep/ptaa104/5891211 (visited on 2026-01-19).

[113] ATLAS Collaboration, "Measurement of the $Z(\to \ell^+\ell^-)\gamma$ production cross-section in pp collisions at $\sqrt{s} = 13$ TeV with the ATLAS detector," *Journal of High Energy Physics*, vol. 2020, no. 54, Mar. 2020. [Online]. Available: https://link.springer.com/10.1007/JHEP03(2020)054 (visited on 2026-01-08).

[114] NNPDF collaboration, "Parton distributions for the LHC run II," *Journal of High Energy Physics*, vol. 2015, no. 4, p. 40, Apr. 2015. [Online]. Available: http://link.springer.com/10.1007/JHEP04(2015)040 (visited on 2025-04-29).

[115] S. Schumann and F. Krauss, "A parton shower algorithm based on Catani-Seymour dipole factorisation," *Journal of High Energy Physics*, vol. 2008, no. 03, pp. 038–038, Mar. 2008. [Online]. Available: http://arxiv.org/abs/0709.1027 (visited on 2026-01-14).

[116] S. Hoeche *et al.*, "QCD matrix elements and truncated showers," *Journal of High Energy Physics*, vol. 2009, no. 05, pp. 053–053, May 2009. [Online]. Available: http://arxiv.org/abs/0903.1219 (visited on 2026-01-14).

[117] S. Alioli *et al.*, "A general framework for implementing NLO calculations in shower Monte Carlo programs: The POWHEG BOX," *Journal of High Energy Physics*, vol. 2010, no. 43, Jun. 2010. [Online]. Available: http://arxiv.org/abs/1002.2581 (visited on 2026-01-14).

[118] S. Frixione, P. Nason, and C. Oleari, "Matching NLO QCD computations with Parton Shower simulations: The POWHEG method," *Journal of High Energy Physics*, vol. 2007, no. 11, pp. 070–070, Nov. 2007. [Online]. Available: http://arxiv.org/abs/0709.2092 (visited on 2026-01-14).

[119] P. Nason, "A New Method for Combining NLO QCD with Shower Monte Carlo Algorithms," *Journal of High Energy Physics*, vol. 2004, no. 11, pp. 040–040, Nov. 2004. [Online]. Available: http://arxiv.org/abs/hep-ph/0409146 (visited on 2026-01-14).

[120] J. Pumplin *et al.*, "New Generation of Parton Distributions with Uncertainties from Global QCD Analysis," *Journal of High Energy Physics*, vol. 2002, no. 07, pp. 012–012, Jul. 4, 2002. [Online]. Available: http://arxiv.org/abs/hep-ph/0201195 (visited on 2026-02-16).

[121] T. Sjöstrand *et al.*, "An Introduction to PYTHIA 8.2," *Computer Physics Communications*, vol. 191, pp. 159–177, Jun. 2015. [Online]. Available: http://arxiv.org/abs/1410.3012 (visited on 2026-01-14).

[122] ATLAS Collaboration, "Evidence of off-shell Higgs boson production from ZZ leptonic decay channels and constraints on its total width with the ATLAS detector," *Physics Letters B*, vol. 846, p. 138 223, Nov. 2023. [Online]. Available: http://arxiv.org/abs/2304.01532 (visited on 2026-01-14).

[123] G. Cowan, *Statistical Data Analysis* (Oxford Science Publications). Clarendon Press, 1998. [Online]. Available: https://books.google.de/books?id=ff8ZyW0nlJAC.

[124] C. Palmer and B. Kronheim, "Improving statistical precision in Monte Carlo samples with negative weights via reweighting and uncertainty quantification," *Physical Review D*, vol. 113, no. 1, p. 012 003, Jan. 2026. [Online]. Available: http://arxiv.org/abs/2510.16217 (visited on 2026-01-16).

[125] ATLAS Collaboration, "Luminosity determination in *pp* collisions at $\sqrt{s} =$ 13 TeV using the ATLAS detector at the LHC," *The European Physical Journal C*, vol. 83, no. 982, Oct. 31, 2023. [Online]. Available: http://arxiv.org/abs/2212.09379 (visited on 2025-03-14).

[126] ATLAS Collaboration, "Electron efficiency measurements with the ATLAS detector using 2012 LHC proton-proton collision data," *The European Physical Journal C*, vol. 77, no. 195, Mar. 2017. [Online]. Available: http://arxiv.org/abs/1612.01456 (visited on 2026-01-22).

[127] ATLAS Collaboration, "Measurement of the photon identification efficiencies with the ATLAS detector using LHC Run-1 data," *The European Physical Journal C*, vol. 76, no. 666, Dec. 2016. [Online]. Available: http://arxiv.org/abs/1606.01813 (visited on 2026-01-22).

[128] ATLAS Collaboration, "Studies of the muon momentum calibration and performance of the ATLAS detector with *pp* collisions at $\sqrt{s}$=13 TeV," *The European Physical Journal C*, vol. 83, no. 686, Aug. 2023. [Online]. Available: http://arxiv.org/abs/2212.07338 (visited on 2025-11-12).

[129] S. Dulat *et al.*, "New parton distribution functions from a global analysis of quantum chromodynamics," *Physical Review D*, vol. 93, no. 3, Feb. 2016. [Online]. Available: http://arxiv.org/abs/1506.07443 (visited on 2026-01-19).

[130] H1 and ZEUS Collaborations. "Combination of Measurements of Inclusive Deep Inelastic $e^{\pm}p$ Scattering Cross Sections and QCD Analysis of HERA Data." (Jun. 2015), [Online]. Available: http://arxiv.org/abs/1506.06042 (visited on 2026-01-19), pre-published.

[131] J. Butterworth *et al.*, "PDF4LHC recommendations for LHC Run II," *Journal of Physics G: Nuclear and Particle Physics*, vol. 43, no. 2, p. 023 001, Jan. 2016. [Online]. Available: http://arxiv.org/abs/1510.03865 (visited on 2025-11-12).

[132] "Scale Variations — yadism documentation." (2024), [Online]. Available: https://yadism.readthedocs.io/en/latest/theory/scale-variations.html (visited on 2026-01-19).

[133] J. Collins, "Choosing the renormalization/factorization scale (QCD)," *Journal of Physics G: Nuclear and Particle Physics*, vol. 17, no. 10, pp. 1547–1549, Oct. 1991. [Online]. Available: https://iopscience.iop.org/article/10.1088/0954-3899/17/10/009 (visited on 2026-01-19).

[134] E. Bagnaschi *et al.*, "An extensive survey of the estimation of uncertainties from missing higher orders in perturbative calculations," *Journal of High Energy Physics*, vol. 2015, no. 133, Feb. 2015. [Online]. Available: http://link.springer.com/10.1007/JHEP02(2015)133 (visited on 2026-02-16).

[135] ATLAS Collaboration, "Measurement of the inclusive isolated prompt photon cross section in *pp* collisions at $\sqrt{s} = 8$ TeV with the ATLAS detector," *Journal of High Energy Physics*, vol. 2016, no. 5, Aug. 2016. [Online]. Available: http://arxiv.org/abs/1605.03495 (visited on 2026-02-04).

[136] ATLAS Collaboration, "Measurement of the cross section for inclusive isolated-photon production in *pp* collisions at $\sqrt{s} = 13$ TeV using the ATLAS detector," *Physics Letters B*, vol. 770, Jul. 2017. [Online]. Available: http://arxiv.org/abs/1701.06882 (visited on 2026-01-22).

[137] ATLAS Collaboration, "Measurements of differential cross-sections in four-lepton events in 13 TeV proton-proton collisions with the ATLAS detector," *Journal of High Energy Physics*, vol. 2021, no. 5, Jul. 2021. [Online]. Available: http://arxiv.org/abs/2103.01918 (visited on 2026-01-22).

[138] ATLAS Collaboration, "Measurements of the production cross section of a Z boson in association with jets in pp collisions at $\sqrt{s} = 13$ TeV with the ATLAS detector," *The European Physical Journal C*, vol. 77, no. 361, May 2017. [Online]. Available: http://arxiv.org/abs/1702.05725 (visited on 2026-02-06).

[139] ATLAS Collaboration, "A simultaneous unbinned differential cross section measurement of twenty-four Z+jets kinematic observables with the ATLAS detector," *Physical Review Letters*, vol. 133, no. 26, Dec. 2024. [Online]. Available: http://arxiv.org/abs/2405.20041 (visited on 2026-02-06).

[140] ATLAS Collaboration, "Tools for estimating fake/non-prompt lepton backgrounds with the ATLAS detector at the LHC," *Journal of Instrumentation*, vol. 18, no. 11, T11004, Nov. 1, 2023. [Online]. Available: http://arxiv.org/abs/2211.16178 (visited on 2025-11-12).

[141] ATLAS Collaboration, "Measurement of $W^{\pm}Z$ production cross sections and gauge boson polarisation in pp collisions at $\sqrt{s} = 13$ TeV with the ATLAS detector," *The European Physical Journal C*, vol. 79, no. 535, Jun. 2019. [Online]. Available: http://arxiv.org/abs/1902.05759 (visited on 2026-02-11).

[142] ATLAS Collaboration, "Measurement of the $W^{\pm}Z$ boson pair-production cross section in pp collisions at $\sqrt{s} = 13$ TeV with the ATLAS detector," *Physics Letters B*, vol. 762, Nov. 2016. [Online]. Available: http://arxiv.org/abs/1606.04017 (visited on 2026-02-11).

[143] ATLAS Collaboration. "Public ATLAS Online Luminosity Plots for Run-2 of the LHC." (Jun. 2025), [Online]. Available: https://twiki.cern.ch/twiki/bin/view/AtlasPublic/LuminosityPublicResultsRun2 (visited on 2026-01-22).

[144] ATLAS Collaboration, "Measurement of the ZZ Production Cross Section in pp Collisions at $\sqrt{s} = 13$ TeV with the ATLAS Detector," *Physical Review Letters*, vol. 116, no. 10, Mar. 2016. [Online]. Available: http://arxiv.org/abs/1512.05314 (visited on 2022-04-24).

[145] ATLAS Collaboration, "Measurement of the inclusive isolated-photon cross section in pp collisions at $\sqrt{s} = 13$ TeV using 36 fb^{-1} of ATLAS data," *Journal of High Energy Physics*, vol. 2019, no. 203, Oct. 2019. [Online]. Available: http://arxiv.org/abs/1908.02746 (visited on 2026-01-31).

[146] ATLAS Collaboration, "Measurement of the Inelastic Proton-Proton Cross Section at s = 13 TeV with the ATLAS Detector at the LHC," *Physical Review Letters*, vol. 117, no. 18, p. 182 002, Oct. 26, 2016. [Online]. Available: https://link.aps.org/doi/10.1103/PhysRevLett.117.182002 (visited on 2025-04-29).

[147] ATLAS Collaboration, "Formulae for Estimating Significance," CERN, Geneva, ATL-PHYS-PUB-2020-025, 2020. [Online]. Available: https://cds.cern.ch/record/2736148 (visited on 2026-01-21).

[148] G. Cowan *et al.*, "Asymptotic formulae for likelihood-based tests of new physics," *The European Physical Journal C*, vol. 71, no. 1554, Feb. 2011. [Online]. Available: http://arxiv.org/abs/1007.1727 (visited on 2025-04-23).

[149] "Public ATLAS Online Luminosity Plots for Run-3 of the LHC." (Nov. 2025), [Online]. Available: https://twiki.cern.ch/twiki/bin/view/AtlasPublic/LuminosityPublicResultsRun3 (visited on 2026-02-19).

[150] O. J. P. Eboli and M. C. Gonzalez-Garcia, "Mapping the genuine bosonic quartic couplings," *Physical Review D*, vol. 93, no. 9, May 2016. [Online]. Available: http://arxiv.org/abs/1604.03555 (visited on 2026-02-20).

[151] C. Degrande *et al.* "Monte Carlo tools for studies of non-standard electroweak gauge boson interactions in multi-boson processes: A Snowmass White Paper." (Sep. 2013), [Online]. Available: http://arxiv.org/abs/1309.7890 (visited on 2025-04-29), pre-published.

[152] ATLAS Collaboration. "Search for the Higgs boson decay to a Z boson and a photon in pp collisions at $\sqrt{s} = 13$ TeV and 13.6 TeV with the ATLAS detector." (Jul. 2025), [Online]. Available: http://arxiv.org/abs/2507.12598 (visited on 2026-02-19), pre-published.

[153] ATLAS Collaboration, "Performance of the ATLAS trigger system in 2015," *The European Physical Journal C*, vol. 77, no. 317, May 2017. [Online]. Available: http://link.springer.com/10.1140/epjc/s10052-017-4852-3 (visited on 2025-04-25).

[154] J. Alwall *et al.*, "The automated computation of tree-level and next-to-leading order differential cross sections, and their matching to parton shower simulations," *Journal of High Energy Physics*, vol. 2014, no. 79, Jul. 2014. [Online]. Available: http://arxiv.org/abs/1405.0301 (visited on 2026-02-01).

[155] NNPDF Collaboration, "Parton distributions with QED corrections," *Nuclear Physics B*, vol. 877, no. 2, Dec. 2013. [Online]. Available: http://arxiv.org/abs/1308.0598 (visited on 2026-02-01).

Appendix A

Technical details

A.1 Trigger selection

The analysis uses the lowest unprescaled single- and dilepton triggers. A list of the used triggers is given in Table A.1.

The trigger names follow a strict naming convention. While `e` refers to electrons, `mu` refers to muons. Numbers in front of the particle abbreviation represent the multiplicity, e. g., `2e` for the di-electron triggers. The number after the particle abbreviation is the HLT transverse momentum threshold in GeV. A chain of particles plus threshold forms a logical *AND*, combining the different requirements on particles, e. g., `mu18_mu8` for the di-muon trigger in 2015 requires one muon with a transverse momentum of at least $p_{\mathrm{T}} \geq 18\,\mathrm{GeV}$ and a second muon with at least $p_{\mathrm{T}} \geq 8\,\mathrm{GeV}$.

All the di-muon triggers have different thresholds for the two required muons; these triggers are referred to as *asymmetric*. In contrast, triggers that have the same requirements on the particles of interest are referred to as *symmetric*, such as the di-electron triggers.

The trigger names also contain information about additional identification and isolation requirements if applied in the trigger. Here, `lh` is the abbreviation for likelihood and indicates that this part of the trigger name refers to the electron identification WP (e. g., loose, medium, or vloose for very loose). If the transverse impact parameter is not used in the identification, the trigger name additionally contains `nod0` (no d_0). The applied isolation WP is given after the prefix `i`.

The part of the trigger name starting with `L1` and in capitalized letters contains information about the L1 seed/Region-of-Interest. The structure is similar to the HLT part: multiplicity, region, threshold, identification,

Table A.1: Overview of the triggers used in the $ZZ\gamma$ event selection.

Trigger type	Year	Trigger name
Single electron trigger	2015	`e24_lhmedium_L1EM20VH`
		`e60_lhmedium`
		`e120_lhloose`
	2016–2018	`e26_lhtight_nod0_ivarloose`
		`e60_lhmedium_nod0`
		`e140_lhloose_nod0`
Single muon trigger	2015	`mu20_iloose_L1MU15`
	2016–2018	`mu26_ivarmedium`
	2015–2018	`mu50`
Di-electron trigger	2015	`2e12_lhloose_L12EM10VH`
	2016	`2e17_lhvloose_nod0`
	2017–2018	`2e24_lhvloose_nod0`
Di-muon trigger	2015	`mu18_mu8noL1`
	2016–2018	`mu22_mu8noL1`

and isolation requirements. The phrase `noL1` means that the particle under consideration does not need to have a seed given by the L1 trigger [108, 153].

A.2 Identification and isolation working points

Reconstructed electrons, muons, and photons have different identification and isolation WPs. The tighter the WPs, the more likely it is a prompt particle. The reconstruction of the final state particles and general definition of the different WPs are described in Section 3.3. More details to the WPs applied in the $ZZ\gamma$ analysis will be given in the following.

A.2.1 Identification working points

While the muon identification WPs are a combination of hit, acceptance, and ratio of charge and momentum requirements, the photon identification WPs have many requirements on the energy in different parts of the

calorimeters, shower width, and on the acceptance. The electron identification WP are likelihood-based and a combination of requirements on the energy in different parts of the calorimeters, shower width, track conditions and track-cluster matching. The $ZZ\gamma$ analysis uses the medium muon identification WP, the loose photon identification WP, and medium or loose electron identification WPs. These WPs are detailed in the following.

Muons used in this analysis are combined muons and to pass the medium identification WP ($|\eta| < 2.5$) the significance of the ratio of charge and momentum (see definition on p.8 in Ref. [74]) must be less than seven and the number of segments with at least three hits in the MDT or CSC detectors need to be larger than one. In case the latter requirement is not fulfilled, the muon still passes the medium identification WP if exactly one segments with at least three hits in the MDT or CSC detectors exists, less than two segments with less than three hits where three hits are expected from the trajectory, and an absolute pseudorapidity of $|\eta| < 0.1$ [74].

The loose identification WP of photons is based on rejection criteria on calorimeter variables. A list of variables is presented in Table A.2 [127].

The loose and medium electron identification WPs are based on a discriminant of the prompt-electron likelihood and the prompt-electron plus non-prompt-electron likelihood. The different quantities used in the likelihood are listed in Table A.3 [110].

A.2.2 Isolation working points

The electron, muon, and photon isolation WPs are a combination of requirements on calorimeter isolation and tracking isolation. The $ZZ\gamma$ analysis uses the Loose electron WP, the PflowLoose muon WP, and the Loose photon WP. The exact thresholds for these WPs are listed in Table A.4.

In Table A.4, $p_{\mathrm{T}}^{\mathrm{cone20}}$ refers to the sum of transverse momentum in a cone of size $\Delta R = 0.2$ around the transverse momentum track in the Inner Detector. The track isolation with a *varcone30* indicates that the cone size is variable, depending on the track momentum. The cone size is defined as [74]

$$\Delta R = \min\left(\frac{10\,\mathrm{GeV}}{p_{\mathrm{T}}\,[\mathrm{GeV}]}, 0.3\right). \tag{A.1}$$

Table A.2: Variables and their description used for the loose identification WP of the photon, taken and modified from [127].

Category	Description
Acceptance	$\lvert\eta\rvert < 2.37$, with $1.37 < \lvert\eta\rvert < 1.52$ excluded
Hadronic leakage	Ratio of E_{T} in the first sampling layer of the hadronic calorimeter to E_{T} of the EM cluster (used over the range $\lvert\eta\rvert < 0.8$ or $\lvert\eta\rvert > 1.37$)
	Ratio of E_{T} in the hadronic calorimeter to E_{T} of the EM cluster (used over the range $0.8 < \lvert\eta\rvert < 1.37$)
EM middle layer	Ratio of 3×7 $\eta \times \phi$ to 7×7 cell energy
	Lateral width of the shower
	Ratio of 3×3 $\eta \times \phi$ to 3×7 cell energy
EM strip layer	Shower width calculated from three strips around the strip with maximum energy deposit
	Total lateral shower width
	Energy outside the core of the three central strips but within seven strips divided by energy within the three central strips
	Difference between energy associated with the second maximum in the strip layer and the energy reconstructed in the strip with the minimum value found between the first and second maxima
	Ratio of the energy difference associated with the largest and second-largest energy deposits to the sum of energy

Table A.3: Quantities and their descriptions used for the definition of the electron identification WP, taken and modified from [110].

Type	Description
Hadronic leakage	Ratio of E_{T} in the first layer of the hadronic calorimeter to E_{T} of the EM cluster (used over the range $\lvert\eta\rvert < 0.8$ or $\lvert\eta\rvert > 1.37$)
	Ratio of E_{T} in the hadronic calorimeter to E_{T} of the EM cluster (used over the range $0.8 < \lvert\eta\rvert < 1.37$)
EM third layer	Ratio of the energy in the third layer to the total energy in the EM calorimeter
EM second layer	Lateral shower width
	Ratio of the energy in 3×3 $\eta \times \phi$ to 3×7 cells centered at the electron cluster position
	Ratio of the energy in 3×7 $\eta \times \phi$ to 7×7 cells centered at the electron cluster position
EM first layer	Shower width
	Ratio of the energy difference between the maximum energy deposit and the energy deposit in a secondary maximum in the cluster to the sum of energy
	Ratio of the energy in the first layer to the total energy in the EM calorimeter
Track conditions	Number of hits in the innermost pixel layer
	Number of hits in the pixel detector
	Number of hits in the pixel and SCT detectors
	Transverse impact parameter and its significance
	Relative momentum lost by the track between the perigee and the last measurement point
TRT	Likelihood probability based on transition radiation
Track cluster matching	$\Delta\eta$ between the cluster position in the first layer and the extrapolated track
	$\Delta\phi$ between the cluster position in the second layer and the momentum-rescaled track times the charge
	Ratio of cluster energy to track momentum

Table A.4: Loose isolation WP thresholds for the electrons, muons, and photons [73, 74].

	Track isolation	Calorimeter isolation
Electron	$\frac{p_{\mathrm{T}}^{\mathrm{varcone30}}}{p_{\mathrm{T}}} < 0.15$	$\frac{E_{\mathrm{T,topo}}^{\mathrm{cone20}}}{p_{\mathrm{T}}} < 0.2$
Photon	$\frac{p_{\mathrm{T}}^{\mathrm{cone20}}}{p_{\mathrm{T}}} < 0.05$	$\frac{E_{\mathrm{T,topo}}^{\mathrm{cone20}}}{p_{\mathrm{T}}} < 0.065$
Muon	$\frac{p_{\mathrm{T}}^{\mathrm{varcone30}}+0.4E_{\mathrm{T}}^{\mathrm{neflow20}}}{p_{\mathrm{T}}} < 0.16$ ($p_{\mathrm{T}} < 50\,\mathrm{GeV}$)	
	$\frac{p_{\mathrm{T}}^{\mathrm{cone20}}+0.4E_{\mathrm{T}}^{\mathrm{neflow20}}}{p_{\mathrm{T}}} < 0.16$ ($p_{\mathrm{T}} > 50\,\mathrm{GeV}$)	

For the calorimeter isolation, the electron and photon isolation WPs dependent on $E_{\mathrm{T,topo}}^{\mathrm{cone20}}$. This variable is the transverse energy sum of topological clusters with their barycenter in a cone of size $\Delta R = 0.2$ around the electron or photon EM topological cluster [85, 110]. Muon calorimeter isolation thresholds are determined via $E_{\mathrm{T}}^{\mathrm{neflow20}}$, the transverse energy sum of neutral particle-flow objects in a cone of size $\Delta R = 0.2$ around the muon energy cluster [74].

A.3 Monte Carlo simulation samples

To understand the underlying behavior of data, compare data to expectation, and extrapolate from CRs to the SR, MC simulations are used. The MC samples simulating the signal process as well as simulations of different background processes (e. g., $pp \to WZ\gamma$, $pp \to ZZ$, $pp \to t\bar{t}\gamma$) are needed in this analysis. A list of all MC simulation samples applied in the signal and background estimation is presented in Table A.5. The samples are grouped into the different simulated processes.

The MC simulation samples for the signal estimation are the $4\ell\gamma$ samples, the SHERPA 2.2.11 $pp \to \ell\ell\ell\ell\gamma$ sample for the direct production and the POWHEGPYTHIA8 $pp \to ZH \to ZZ\gamma$ sample for the Higgs contribution. They are described in detail in Section 4.3.

For the non-prompt photon background, the SHERPA 2.2.4 $pp \to \ell\ell\gamma$

Table A.5: Overview of MC simulation samples used in the analysis. The samples are grouped into the different areas they are primarily used for. The process describes the matrix element calculation without the simultaneous produced additional partons. The precision of the matrix element depends on the number of additional partons (jets) produced with the hard scatter event. The used PDF sets are given. Depending on the used event generator, matrix element and parton shower are either simulated by the same generator or two different ones are used.

	Process	Precision	PDF set	Generator
$4\ell\gamma$	$pp \to \ell\ell\ell\ell\gamma$	0j@NLO+1, 2j@LO	NNPDF 3.0 NNLO	Sherpa 2.2.11
	$pp \to ZH \to ZZ\gamma$	NLO	AZNLO CTEQ6L1	PowhegPythia8
Z	$pp \to \ell\ell\gamma$	0–3j@LO	NNPDF 3.0 NNLO	Sherpa 2.2.4
	$pp \to \ell\ell$	0–3j@NLO	NNPDF 3.1 NNLO	MadGraphPythia8
		0–2j@NLO+3–5@LO	NNPDF 3.0 NNLO	Sherpa 2.2.11
ZZ	$qq \to \ell\ell\ell\ell$	0, 1j@NLO	NNPDF 2.3 LO	MadGraphPythia8
		0, 1j@NLO+2, 3j@LO	NNPDF 3.0 NNLO	Sherpa 2.2.2
	$gg \to \ell\ell\ell\ell$	0, 1j@LO	NNPDF 3.0 NNLO	Sherpa 2.2.2
WZ	$pp \to \ell\ell\ell\nu$	0, 1j@NLO+2, 3j@LO	NNPDF 3.0 NNLO	Sherpa 2.2.2
	$pp \to \ell\ell\ell\nu\gamma$	0j@NLO+1, 2j@LO	NNPDF 3.0 NNLO	Sherpa 2.2.11
	$pp \to WWZ$	0j@NLO+1, 2j@LO	NNPDF 3.0 NNLO	Sherpa 2.2.2
$t\bar{t}$	$pp \to t\bar{t} \to \ell\nu\ell\nu\gamma, \ell\nu qq\gamma$	LO	NNPDF 2.3 LO	MadGraphPythia8
	$pp \to t\bar{t} \to \ell\nu\ell\nu, \ell\nu qq$	NLO	NNPDF 3.0 NLO	PowhegPythia8
	$pp \to t\bar{t}\ell\ell$	0j@NLO+1–3j@LO	NNPDF 3.0 NNLO	Sherpa 2.2.11
γ	$pp \to \gamma$	1, 2j@NLO + 3, 4j@LO	NNPDF 3.0 NNLO	Sherpa 2.2.2

with up to three partons at LO is used for the non-prompt photon estimation in the $Z\gamma$ CR. This sample uses the NNPDF3.0 PDF sets [114] and the Sherpa parton-shower algorithm [115].

To validate the extrapolation from the $Z\gamma$ CR to the SR via the ZZ+jet and Z+jet ratio, the MadGraphPythia8 and Sherpa 2.2.11 $pp \to \ell\ell$ samples, the MadGraphPythia8 and Sherpa 2.2.2 $qq \to \ell\ell\ell\ell$ samples, as well as the Sherpa 2.2.2 $gg \to \ell\ell\ell\ell$ are used. All Sherpa samples use the NNPDF3.0 PDF sets [114] and the Sherpa parton-shower algorithm [115], while the MadGraphPythia8 samples use MadGraph [154] for the matrix calculation, the NNPDF3.1 PDF sets [93] (NNPDF2.3 PDF sets [155]) for the $pp \to \ell\ell$ ($qq \to \ell\ell\ell\ell$) samples, and are interfaced with the Pythia8 parton-shower algorithm [121].

For the subtraction of backgrounds in the $Z\gamma$ CR, the Sherpa 2.2.2 $pp \to \ell\ell\ell\nu$ MC sample as well as the MadGraphPythia8 $pp \to t\bar{t} \to$

$\ell\nu\ell\nu\gamma, \ell\nu qq\gamma$ MC sample are used. The SHERPA 2.2.2 sample uses the same setup as described earlier, and the MADGRAPHPYTHIA8 uses the NNPDF2.3 PDF sets [155] and is interfaced with the PYTHIA8 parton-shower algorithm [121].

The estimation of the fake efficiency and the study of the fake-enriched CR involve the SHERPA 2.2.2 $pp \to \ell\ell\ell\nu$ MC sample and the POWHEG-PYTHIA8 $pp \to t\bar{t} \to \ell\nu\ell\nu, \ell\nu qq$ MC samples. Both use NNPDF3.0 PDF sets [114]. The SHERPA 2.2.2 sample is interfaced with the SHERPA parton-shower algorithm [115] and the POWHEGPYTHIA8 with the PYTHIA8 parton-shower algorithm [121].

For the validation of the misidentified lepton background, the SHERPA 2.2.2 $pp \to WWZ$ and SHERPA 2.2.11 $pp \to t\bar{t}\ell\ell$ MC samples are used. Both samples have the NNPDF3.0 PDF sets [114] and are interfaced with the SHERPA parton-shower algorithm [115].

The MC overlay in the pileup estimation uses the same SHERPA 2.2.2 $qq \to \ell\ell\ell\ell$ MC samples as for the non-prompt photon estimation and the SHERPA 2.2.2 $pp \to \gamma$ MC samples with the same PDF sets and parton-shower algorithm.

A.4 Baseline and control region selection criteria

The baseline selection contains all selection criteria applied to the SR as well as to all CRs. It mainly contains object selection criteria but also general event selection criteria. A detailed description is given in Section 4.2.1. A summary table is shown in Table A.6.

Detailed tables of the event selection criteria of the CRs defined in the background estimation are given in the subsequent section.

A.4.1 Control regions for the non-prompt photon estimation

For the non-prompt photon estimation, four different CRs are defined. The $Z\gamma$ CR is needed to estimate $Z\gamma$ events with a non-prompt photon. The selection criteria are listed in Table A.7. The estimate of $Z\gamma$ events with a non-prompt photon is extrapolated to the SR using the ratio of ZZ+jet to Z+jet events. These events are estimated in the ZZ+jet CR and Z+jet

Table A.6: Overview of the baseline selection.

Event	Good Run List, vertex, trigger matching, overlap removal		
	p_{T}	η	Identification and isolation
Electrons	$p_{\mathrm{T}} > 10\,\mathrm{GeV}$	$\lvert\eta\rvert < 2.47$, excluded $1.37 < \lvert\eta\rvert < 1.52$	Loose ID, no iso, $\lvert d_0\rvert/\sigma_{d_0} < 5$, $\lvert z_0 \sin(\theta)\rvert < 0.5\,\mathrm{mm}$
Muons	$p_{\mathrm{T}} > 10\,\mathrm{GeV}$	$\lvert\eta\rvert < 2.5$	Medium ID, no iso, $\lvert d_0\rvert/\sigma_{d_0} < 10$, $\lvert z_0 \sin(\theta)\rvert < 0.5\,\mathrm{mm}$
Photons	$p_{\mathrm{T}} > 15\,\mathrm{GeV}$	$\lvert\eta\rvert < 2.37$, excluded $1.37 < \lvert\eta\rvert < 1.52$	Loose ID, no iso
Jets	$p_{\mathrm{T}} > 20\,\mathrm{GeV}$	$\lvert y\rvert < 4.4$	Pflow, jet vertex tagger < 0.59

Table A.7: Summary of the event selection criteria in the $Z\gamma$ CR.

	Electrons	Muons	Photon
Kinematics	$p_{\mathrm{T}} > 30, 25\,\mathrm{GeV}$		$p_{\mathrm{T}} > 20\,\mathrm{GeV}$
	$\lvert\eta\rvert < 2.47$	$\lvert\eta\rvert < 2.5$	$\lvert\eta\rvert < 2.37$
excluded	$1.37 < \lvert\eta\rvert < 1.52$		$1.37 < \lvert\eta\rvert < 1.52$
Isolation	Loose	Loose	Loose
	$\Delta R(\mu, e) > 0.2$		$\Delta R(\ell, \gamma) > 0.4$
Identification	Medium	Medium	Tight
Multiplicity	≥ 1 OSSF pair		≥ 1 photon
Invariant mass	$m_{\ell\ell} > 40$ GeV, $(m_{\ell\ell\gamma} + m_{\ell\ell}) > 2 \cdot m_Z$		

CR, respectively. The selection criteria of the two CRs are combined and summarized in Table A.8. For the validation of the method, a $WZ\gamma$ CR is defined. The selection criteria are presented in Table A.9.

A.4.2 Control regions for the misidentified lepton estimation

For the misidentified lepton estimate, a variety of CRs are defined. For the fake efficiency, the fake-enriched $Z + 1\ell$ CR is needed. The selection criteria are listed in Table A.10. For the fake lepton estimation with the matrix method, four additional CRs with a different number of leptons passing the tight selection and passing the loose but failing the tight selection are

Table A.8: Summary of the event selection criteria in the $Z(Z)$+jet CR.

	Electrons	Muons	Jet
Kinematics	$p_{\mathrm{T}} > 30, 25, (10, 10)$ GeV		$p_{\mathrm{T}} > 20$ GeV
	$\lvert\eta\rvert < 2.47$	$\lvert\eta\rvert < 2.5$	$\lvert\eta\rvert < 2.6$
excluded	$1.37 < \lvert\eta\rvert < 1.52$		
Isolation	Loose	Loose	
	$\Delta R(\mu, e) > 0.2$		$\Delta R(\ell, \text{jet}) > 0.4$
Identification	Medium	Medium	PFlow
Multiplicity	$\geq 1(2)$ OSSF pairs		≥ 1 jet
Invariant mass	$m_{\ell\ell} > 40$ GeV		

Table A.9: Summary of the event selection criteria in the $WZ\gamma$ CR.

	Electrons	Muons	Photon
Kinematics	$p_{\mathrm{T}} > 30, 25$ GeV		$p_{\mathrm{T}} > 20$ GeV
	$\lvert\eta\rvert < 2.47$	$\lvert\eta\rvert < 2.5$	$\lvert\eta\rvert < 2.37$
excluded	$1.37 < \lvert\eta\rvert < 1.52$		$1.37 < \lvert\eta\rvert < 1.52$
Isolation	Loose	Loose	Loose
	$\Delta R(\mu, e) > 0.2$		$\Delta R(\ell, \gamma) > 0.4$
Identification	Medium	Medium	Tight
Multiplicity	≥ 3 leptons, ≥ 1 OSSF pair		≥ 1 photon
Invariant mass	$m_{\ell\ell} > 40$ GeV, $(m_{\ell\ell\gamma} + m_{\ell\ell}) > 2 \cdot m_Z$		

Table A.10: Overview of the event selection in the $Z + 1\ell$ CR.

	Electrons	Muons
Kinematics	$p_{\mathrm{T}} > 30, 25, 10\,\mathrm{GeV}$	
	$\lvert\eta\rvert < 2.47$	$\lvert\eta\rvert < 2.5$
excluded	$1.37 < \lvert\eta\rvert < 1.52$	
Isolation	Z lepton: Loose Lepton 3: —	Z lepton:Loose Lepton 3: —
	$\Delta R(\mu, e) > 0.2$	
Identification	Z lepton: Medium Lepton 3: Loose	Medium
$d0$ significance	< 5	Z lepton: < 3 Lepton 3: < 10
Multiplicity	$= 3\ell$, 1 OSSF pair	
Invariant mass	$\min(\mid m_{\ell\ell,1} - m_Z \mid)$, $m_{\ell\ell} > 40\,\mathrm{GeV}$	

needed. The common selection criteria of CR1–4 are shown in Table A.11 and the individual differences are shown in Table A.12. Due to the limited statistics in CR1–4, the number of fake leptons are estimated in the ZZ CR, see Table A.13 for the selection criteria of the CR, and CR'1–4 are defined. Their selection criteria are given in Table A.14 and the individual differences are the same as for CRs1–4, see Table A.12. The validation of the misidentified lepton estimate is done in the same-sign VR for the estimate in the SR and in the same-sign VR' for the estimate in the ZZ CR. The selection criteria of the two regions are presented in Table A.15 and in Table A.16, respectively.

Table A.11: Overview of the common event selection in CR1–4.

	Electrons	Muons	Photon
Kinematics	$p_{\mathrm{T}} > 30, 25, 10, 10\,\mathrm{GeV}$		$p_{\mathrm{T}} > 20\,\mathrm{GeV}$
	$\lvert\eta\rvert < 2.47$	$\lvert\eta\rvert < 2.5$	$\lvert\eta\rvert < 2.37$
excluded	$1.37 < \lvert\eta\rvert < 1.52$		$1.37 < \lvert\eta\rvert < 1.52$
Isolation	—	—	Loose
	$\Delta R(\mu, e) > 0.2$		$\Delta R(\ell, \gamma) > 0.4$
Identification	Loose	Medium	Tight
$d0$ significance	< 5	< 10	
Multiplicity	≥ 2 OSSF pairs		≥ 1 photon
Invariant mass	$\min(\mid m_{\ell\ell,1} - m_Z \mid + \mid m_{\ell\ell,2} - m_Z \mid)$, $m_{\ell\ell} > 40\,\mathrm{GeV}$, $(m_{\ell\ell\gamma} + m_{\ell\ell}) > 2 \cdot m_Z$		

Table A.12: Overview of the differences in the event selection of CR1–4 (CR′1–4).

CR	Criteria	Flavor	Lepton 1	Lepton 2	Lepton 3	Lepton 4
CR1	Isolation	Electron	Loose	Loose	Loose	—
		Muon	Loose	Loose	Loose	—
	Identification	Electron	Medium	Medium	Medium	Loose
		Muon	Medium	Medium	Medium	Medium
	$d0$ significance	Electron	< 5	< 5	< 5	< 5
		Muon	< 3	< 3	< 3	< 10
CR2	Isolation	Electron	Loose	Loose	—	—
		Muon	Loose	Loose	—	—
	Identification	Electron	Medium	Medium	Loose	Loose
		Muon	Medium	Medium	Medium	Medium
	$d0$ significance	Electron	< 5	< 5	< 5	< 5
		Muon	< 3	< 3	< 10	< 10
CR3	Isolation	Electron	Loose	—	—	—
		Muon	Loose	—	—	—
	Identification	Electron	Medium	Loose	Loose	Loose
		Muon	Medium	Medium	Medium	Medium
	$d0$ significance	Electron	< 5	< 5	< 5	< 5
		Muon	< 3	< 10	< 10	< 10
CR4	Isolation	Electron	—	—	—	—
		Muon	—	—	—	—
	Identification	Electron	Loose	Loose	Loose	Loose
		Muon	Medium	Medium	Medium	Medium
	$d0$ significance	Electron	< 5	< 5	< 5	< 5
		Muon	< 10	< 10	< 10	< 10

Table A.13: Overview of the event selection in the ZZ CR.

	Electrons	Muons
Kinematics	$p_{\mathrm{T}} > 30, 25, 10, 10\,\mathrm{GeV}$	
	$\lvert\eta\rvert < 2.47$	$\lvert\eta\rvert < 2.5$
excluded	$1.37 < \lvert\eta\rvert < 1.52$	
Isolation	Loose	Loose
	$\Delta R(\mu, e) > 0.2$	
Identification	Medium	Medium
$d0$ significance	< 5	< 3
Multiplicity	≥ 2 OSSF pairs	
Invariant mass	$\min(\mid m_{\ell\ell,1} - m_Z \mid + \mid m_{\ell\ell,2} - m_Z \mid), m_{\ell\ell} > 40\,\mathrm{GeV}$	

Table A.14: Overview of the common event selection in CR'1–4.

	Electrons	Muons
Kinematics	$p_{\mathrm{T}} > 30, 25, 10, 10\,\mathrm{GeV}$	
	$\lvert\eta\rvert < 2.47$	$\lvert\eta\rvert < 2.5$
excluded	$1.37 < \lvert\eta\rvert < 1.52$	
Isolation	$\Delta R(\mu, e) > 0.2$	
Identification	Loose	Medium
$d0$ significance	< 5	< 10
Multiplicity	≥ 2 OSSF pairs	
Invariant mass	$\min(\mid m_{\ell\ell,1} - m_Z \mid + \mid m_{\ell\ell,2} - m_Z \mid), m_{\ell\ell} > 40\,\mathrm{GeV}$	

Table A.15: Overview of the event selection in the same-sign VR.

	Electrons	Muons	Photon
Kinematics	$p_{\mathrm{T}} > 30, 25, 10, 10\,\mathrm{GeV}$		$p_{\mathrm{T}} > 20\,\mathrm{GeV}$
	$\lvert\eta\rvert < 2.47$	$\lvert\eta\rvert < 2.5$	$\lvert\eta\rvert < 2.37$
excluded	$1.37 < \lvert\eta\rvert < 1.52$		$1.37 < \lvert\eta\rvert < 1.52$
Isolation	Loose	Loose	Loose
	$\Delta R(\mu, e) > 0.2$		$\Delta R(\ell, \gamma) > 0.4$
Identification	Medium	Medium	Tight
$d0$ significance	< 5	< 3	
Multiplicity	≥ 1 OSSF pair, ≥ 1 SSSF pair		≥ 1 photon
Invariant mass	$\min(\mid m_{\ell\ell,1} - m_Z \mid + \mid m_{\ell\ell,2} - m_Z \mid)$, $m_{\ell\ell} > 40\,\mathrm{GeV}$, $(m_{\ell\ell\gamma} + m_{\ell\ell}) > 2 \cdot m_Z$		
Trigger	Single and dilepton trigger		

Table A.16: Overview of the event selection in the same-sign VR′.

	Electrons	Muons
Kinematics	$p_{\mathrm{T}} > 30, 25, 10, 10\,\mathrm{GeV}$	
	$\lvert\eta\rvert < 2.47$	$\lvert\eta\rvert < 2.5$
excluded	$1.37 < \lvert\eta\rvert < 1.52$	
Isolation	Loose	Loose
	$\Delta R(\mu, e) > 0.2$	
Identification	Medium	Medium
$d0$ significance	< 5	< 3
Multiplicity	≥ 1 OSSF pair, ≥ 1 SSSF pair	
Invariant mass	$\min(\mid m_{\ell\ell,1} - m_Z \mid + \mid m_{\ell\ell,2} - m_Z \mid)$, $m_{\ell\ell} > 40\,\mathrm{GeV}$	

Appendix B

Event selection studies

B.1 Signal significance optimization

The signal selection is optimized to maximize the signal contribution while minimizing the background in the SR. Thus, the signal significance Z is maximized, with [147],

$$Z = \sqrt{2\left(N \ln\left[\frac{N(N_{\text{bkg}} + \sigma_{\text{bkg}}^2)}{N_{\text{bkg}}^2 + N\sigma_{\text{bkg}}^2}\right] - \frac{N_{\text{bkg}}^2}{\sigma_{\text{bkg}}^2} \ln\left[1 + \frac{\sigma_{\text{bkg}}^2(N - N_{\text{bkg}})}{N_{\text{bkg}}(N_{\text{bkg}} + \sigma_{\text{bkg}}^2)}\right]\right)}, \tag{B.1}$$

with N the total number of signal and background events, N_{bkg} the number of background events, and σ_{bkg} the uncertainty in the background.

First, a minimum event selection is defined that contains all selection criteria that cannot be loosened or neglected. With this minimum event selection applied, we optimize the signal selection by maximizing the signal significance.

The minimum event selection fulfills the baseline selection criteria (see Section 4.2.1) and requires the final state particles: two OSSF lepton pairs and a photon. The two OSSF lepton pairs are selected with the optimized selection algorithm. To suppress misidentified leptons and non-prompt leptons, the leptons (electron and muons) must pass the medium identification WPs and the loose isolation WP [73, 74]. To ensure that the triggers are fully efficient, the leading and sub-leading leptons must pass the transverse momentum thresholds of $p_{\text{T}} > 30\,\text{GeV}$ and $p_{\text{T}} > 25\,\text{GeV}$, respectively. The photon must pass additionally the transverse-momentum threshold of $p_{\text{T}}^{\gamma} > 15\,\text{GeV}$, the loose isolation WP, and the tight identification WP [73]. These photon requirements are needed to take advantage of

the results of the ATLAS $Z\gamma$ analysis [113] for the non-prompt photon background estimation. To suppress events with photon FSR, the FSR rejection must be applied as well.

The signal significance is derived for each selection criterion and only the requirements improving the significance are considered further. Only the total signal and background yields are used; no distributions are analyzed. The number of signal events is the total yield of the $4\ell\gamma$ sample and the $ZH \to ZZ\gamma$ sample (see Section 4.3).

For the number of background, only the non-prompt photon and misidentified lepton background are considered; the pileup contribution is neglected. The non-prompt photon estimates for the different selection criteria are derived with the MC-based $Z\gamma$ estimates; the jet ratio is from data. All estimates of the misidentified lepton background use the real and fake efficiencies derived in Section 5.2.2. The data events passing CR'1–4 and the ratio of $N_{ZZ\gamma}$ and N_{ZZ} events are derived for each selection criterion to estimate the number of misidentified leptons. The same relative uncertainty (see Table 6.1) is applied to each background estimate.

We individually apply selection criteria which might increase the signal significance. The signal significance after the minimum event selection is $Z = 3.99\sigma$ and taken as baseline. Each selection criterion increasing this significance is considered further, all others are discarded. The signal and background yields including the significance for each of the selection criteria is shown in Fig. B.1.

First, we optimize the trigger selection. The selection criterion after the baseline selection are tighter requirements on the leading lepton. In case only single lepton trigger are used, the leading lepton must pass the tight identification WP if it is an electron or the tight isolation WP if it is a muon to prevent a bias. Since no significance increase is present for this selection criterion, we use the combination of single and dilepton triggers.

The thresholds and selection criteria on the dilepton invariant mass are also optimized. Various upper and lower thresholds are applied as well as two different window cuts. The dilepton invariant mass thresholds of $m_{\ell\ell} > 20\,\text{GeV}$ and $m_{\ell\ell} > 40\,\text{GeV}$ result in an increase of the significance. All other criteria effect a decrease in the significance. Since all background contributions contain at least one Z boson, the non-prompt photon and

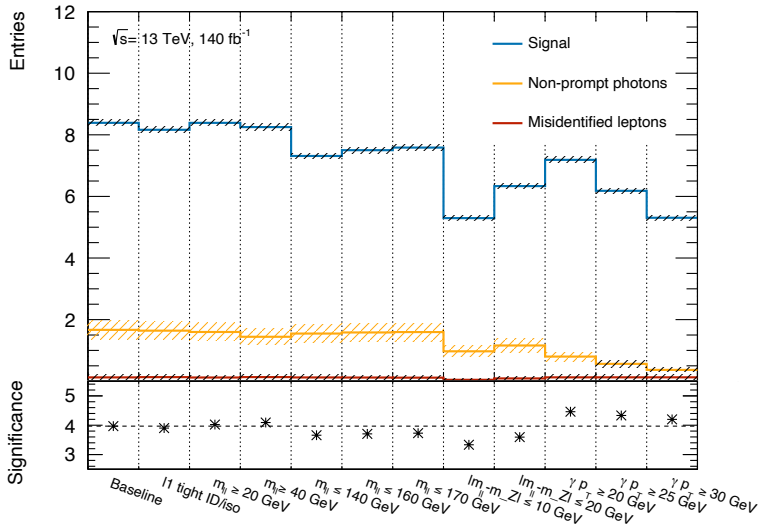


Figure B.1: Overview of the number of signal and background events for each selection criteria. All selection criteria are applied individually. The lower panel shows the signal significance and the dotted line represents the baseline significance.

pileup even two, tighter selection criteria on the invariant mass of the Z boson reduce the signal contribution to a larger degree than the background contributions. Nonetheless, the dilepton invariant mass thresholds of $m_{\ell\ell} > 40\,\text{GeV}$ is applied to the signal selection since it has a positive effect on the significance.

Lastly, the photon transverse-momentum threshold is optimized. The baseline selection has a threshold of $p_{\text{T}}^{\gamma} > 15\,\text{GeV}$. Additionally, photon transverse-momentum thresholds of $p_{\text{T}}^{\gamma} > 20\,\text{GeV}$, $p_{\text{T}}^{\gamma} > 25\,\text{GeV}$, and $p_{\text{T}}^{\gamma} > 30\,\text{GeV}$ are imposed. All thresholds increase the signal significance. The dominant non-prompt photon background is a falling function of the photon transverse momentum. The distribution is falling steeper than the photon transverse momentum distribution of the signal. Thus, the higher the transverse momentum threshold, the lower the non-prompt photon

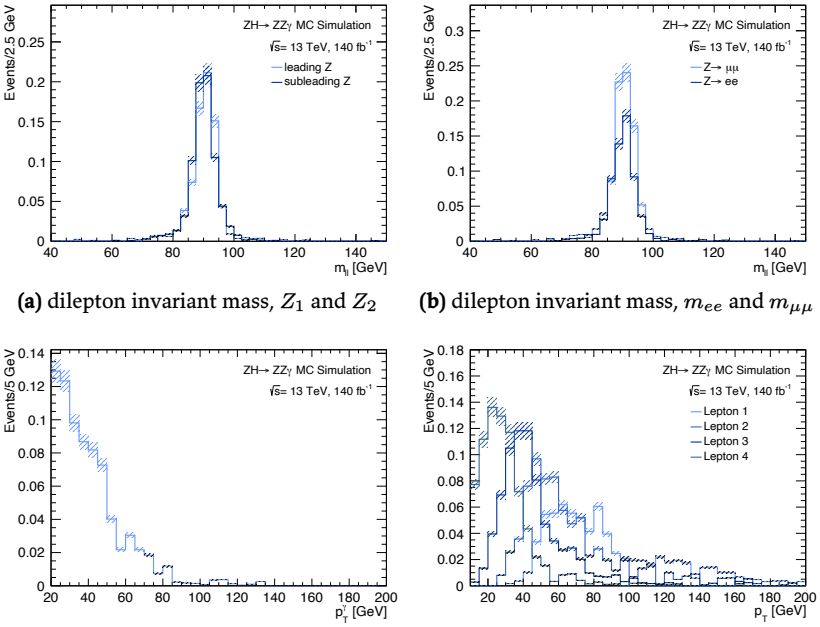
background. Due to the non-linear signal and background relation in the calculation of the significance, a photon transverse-momentum threshold of $p_{\mathrm{T}}^{\gamma} > 20\,\mathrm{GeV}$ results in the highest significance. This threshold is applied in the signal selection.

B.2 Kinematic distributions

The distributions of different kinematic properties, such as the dilepton invariant mass or the transverse momentum of final state particles, is shown in Fig. B.2 for the $ZH \to ZZ\gamma$ sample.

The dilepton invariant mass distributions (Figs. B.2a and B.2b) are very similar to the $4\ell\gamma$ distributions (see Section 4.3). All Z bosons are on-shell. The lepton transverse-momentum distributions (Fig. B.2d) show the behavior as the $4\ell\gamma$ distributions. However, all momentum distributions have a lower mean in the $ZH \to ZZ\gamma$ sample compared to the $4\ell\gamma$ sample.

The largest difference between the two signal sample distributions is present in the photon transverse momentum distribution (Fig. B.2c). The on-shell Higgs decay into a Z boson and a photon limit the available momenta. The photon distribution contains a contribution from the falling photon spectrum (similar to the $4\ell\gamma$ sample) as well as a distribution peaking around 45 GeV, roughly the difference between the Higgs boson and Z boson mass.



(a) dilepton invariant mass, Z_1 and Z_2

(b) dilepton invariant mass, m_{ee} and $m_{\mu\mu}$

(c) photon transverse momentum

(d) lepton transverse momentum

Figure B.2: The invariant mass distributions of the two leptons of the leading and sub-leading Z boson (top, left) and the dilepton invariant mass of the electrons and muons (top, right). The kinematic distributions of the transverse momentum of the photon (bottom, left) and the transverse momentum distribution of the leading, sub-leading, third leading and fourth leading lepton (bottom, right). All distributions show events simulated with the $ZH(\rightarrow Z\gamma)$ signal sample and passing the SR selection criteria. Total uncertainties are shown, and the events are scaled to the Run 2 luminosity.

Appendix C

Non-prompt photons

C.1 Comparison of the non-prompt photon estimates

More detailed comparisons of the $N_{Z\gamma}^{\gamma_{\text{fake}}}$ estimates as well as their consistency with the results from the $Z\gamma$ analysis [113] are presented in Appendices C.1.1 and C.1.2. Additional comparisons regarding the CRs of the jet ratio are detailed in Appendix C.1.3.

C.1.1 Comparison of the different methods

The different methods give consistent results, as shown in Table C.1. While the shape differs slightly, see Fig. C.1, the overall agreement is good. A detailed list of the different uncertainties is displayed in Table C.2.

C.1.2 Comparison to the $Z\gamma$ analysis

The results of the two different purity estimates are compared to the estimate of the $Z\gamma$ analysis in Table C.3. A detailed comparison of the number of data and MC simulation estimates in the $Z\gamma$ CR is given in Table C.4. The

Table C.1: Comparison of the results with the purity methods and the subtraction method. The total uncertainties are presented.

	$N_{Z\gamma}^{\gamma_{\text{fake}}}$
Purity+data	$28\,368 \pm 4\,295$ (tot.)
Purity+MC	$26\,503 \pm 5\,146$ (tot.)
Subtraction	$28\,288 \pm 3\,620$ (tot.)

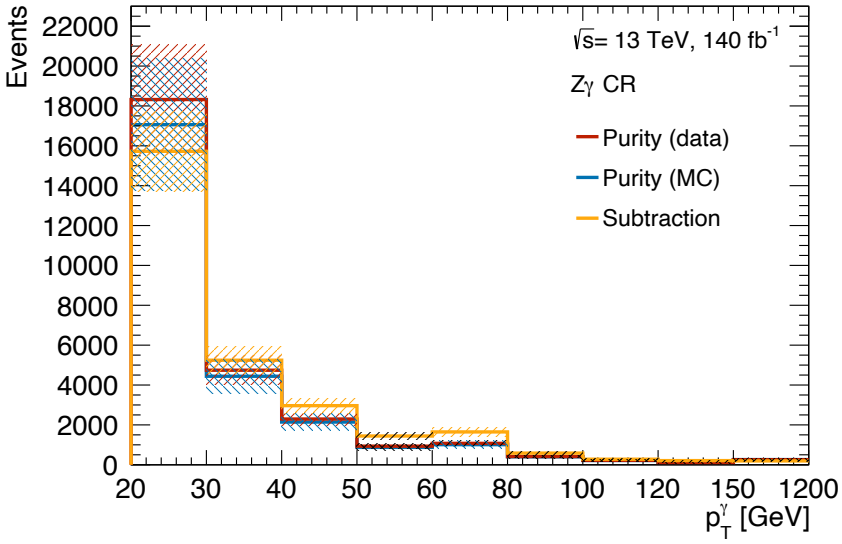


Figure C.1: The transverse momentum distribution of the photon for events with a non-prompt photon in the $Z\gamma$ CR. The figure shows the distributions from the purity measurement with data and MC samples as well as the distribution from the subtraction method. The total systematic uncertainties are shown.

Table C.2: Summary of the uncertainty sources and their relative contributions to the different estimates of the number of non-prompt photon events in the $Z\gamma$ CR.

Source	Subtraction	Purity+data	Purity+MC
Statistics	1.67%	0.27%	0.11%
Integrated luminosity	0.83%	0.83%	0.83%
MC systematic	12.67%	—	2.32%
Purity measurement (tot.)	—	13.61%	17.93%
Modelling uncertainty	—	6.57%	7.04%
Total uncertainty	12.81%	15.14%	19.42%

Table C.3: Number of prompt photon $Z\gamma$ events and number of non-prompt photon $Z\gamma$ events for photon transverse momentum thresholds of $p_{\mathrm{T}} > 20\,\mathrm{GeV}$ and 30 GeV in the $Z\gamma$ CR derived with the purity methods. Additionally, the results are given from the $Z\gamma$ analysis [113] with $p_{\mathrm{T}} > 30\,\mathrm{GeV}$ for the photon in the last row for comparison. The statistical uncertainties are the propagated data and MC statistics. The contributions of the systematic uncertainty are shown in Table C.2.

	$N_{Z\gamma}^{\gamma_{\text{fake}}}$ (data)	$N_{Z\gamma}^{\gamma_{\text{fake}}}$ (MC)
$\gamma_{p_{\mathrm{T}}} > 20\,\mathrm{GeV}$	28368 ± 76 (stat.) ± 3862 (syst.)	26503 ± 30 (stat.) ± 4770 (syst.)
$\gamma_{p_{\mathrm{T}}} > 30\,\mathrm{GeV}$	10047 ± 34 (stat.) ± 1244 (syst.)	9445 ± 9 (stat.) ± 1313 (syst.)
$Z\gamma$ analysis	9592 ± 256 (stat.) ± 683 (syst.)	

Table C.4: Number of data and expected events in the $Z\gamma$ CR. The first column shows the results for a transverse momentum threshold of the photon of 20 GeV, the second for a threshold of 30 GeV and the last column are the results from the $Z\gamma$ analysis[113]. The number of $N_{Z\gamma}^{\gamma_{\text{fake}}}$ is estimated via the subtraction method.

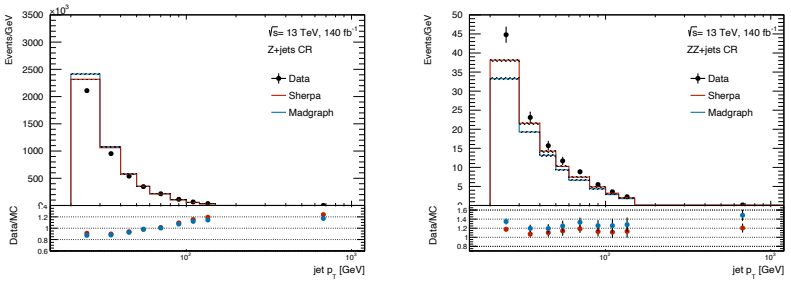
Source	$Z\gamma$ CR ($p_T > 20\,\mathrm{GeV}$)	$Z\gamma$ CR ($p_T > 30\,\mathrm{GeV}$)	$Z\gamma$ analysis [113]
N^{obs}	173 708 ± 417 (stat.)	99 971 ± 316 (stat.)	95 756 ± 309 (stat.)
$N_{Z\gamma}$	130 984 ± 222 (stat.) ± 3091 (syst.)	80 734 ± 173 (stat.) ± 1905 (syst.)	79 485 ± 91 (stat.) ± 2196 (syst.)
$N_{Z\gamma}^{\gamma_{\text{fake}}}$	28 288 ± 473 (stat.) ± 3589 (syst.)	12 565 ± 361 (stat.) ± 2006 (syst.)	9592 ± 256 (stat.) ± 683 (syst.)
$N_{tt\gamma}$	4953 ± 16 (stat.) ± 527 (syst.)	3674 ± 14 (stat.) ± 391 (syst.)	3635 ± 13 (stat.) ± 387 (syst.)
N_{PU}	8707 ± 1741 (tot.)	2394 ± 479 (tot.)	2394 ± 342 (tot.)
N_{WZ}	548 ± 5 (stat.) ± 117 (syst.)	425 ± 5 (stat.) ± 91 (syst.)	453 ± 4 (stat.) ± 97 (syst.)
N_{ZZ}	227 ± 7 (stat.) ± 49 (syst.)	179 ± 6 (stat.) ± 39 (syst.)	166 ± 1 (stat.) ± 36 (syst.)

table includes the results for a photon transverse momentum threshold of $p_{\mathrm{T}} > 30\,\mathrm{GeV}$ and the results of the $Z\gamma$ analysis [113] for a direct comparison.

C.1.3 Comparison of data and prediction in the jet ratio

To understand the underlying reason for the difference between data and prediction in the jet ratio, a direct comparison of data and prediction in each of the two CRs is shown in Fig. C.2.

In Fig. C.2 we can see that the data-prediction agreement differs for the Z+jet and ZZ+jet CR. In the case of the Z+jet CR, a shape difference—an



(a) **(b)**

Figure C.2: Transverse momentum distribution of the jet for selected Z+jet events in the Z+jet CR (a). Transverse momentum distribution of the jet for selected ZZ+jet events in the ZZ+jet CR (b). The shaded regions show the statistical uncertainty. The bottom panels show the ratio of data and prediction.

overestimation in the prediction for low transverse momenta and an underestimation for high transverse momenta—is present. This shape difference has already been observed in previous analyses [138, 139] and is due to the limited understanding of QCD. In the ZZ+jet CR, a roughly 20% offset between data and the MADGRAPH prediction is observed, while the difference between data and the SHERPA prediction is around 15%. The difference in offset between the predictions originates from the not-included $gg \to \ell\ell\ell\ell$ contribution for the MADGRAPH prediction. The remaining 10–15% difference most likely originates from not-included NLO electroweak corrections of the $qq \to ZZ$ samples and other background processes. These effects overlap in the ratio and result in the data versus prediction difference seen in Fig. 5.6.

C.2 Jet ratio uncertainties

An overview of the experimental uncertainties for the SHERPA and MADGRAPHPYTHIA8 samples is shown in Table C.5, and the theory uncertainties are shown in Table C.6. The luminosity uncertainty fully cancels.

Table C.5: Relative contribution of the different experimental uncertainties for the ratio of ZZ+jet and Z+jet events.

Uncertainty source	Relative uncertainty [%] SHERPA	MADGRAPH
Jet energy resolution	5.92	1.50
Jet energy scale	5.11	2.52
Total jet uncertainty	7.82	2.93
Electron-photon energy resolution and scale	0.39	0.34
Electron identification efficiency	1.65	0.23
Electron reconstruction efficiency	0.21	0.29
Total electron uncertainty	1.71	0.50
Muon isolation efficiency	1.53	1.30
Muon reconstruction efficiency	0.42	0.39
Muon momentum resolution and scale	0.13	0.21
Total muon uncertainty	1.59	1.37
Pileup reweighting	3.87	5.58
Total systematic uncertainty	9.03	6.47

Table C.6: Overview of the theoretical uncertainty sources for the ratio of N_{ZZ}^{jets} and N_{Z}^{jets}.

Source	Relative uncertainty [%] SHERPA	MADGRAPH
Scale variations	$^{+3.6}_{-8.8}\%$	$^{+6.5}_{-3.4}\%$
PDF variations	2.5%	3.4%
Total theory uncertainty	$^{+4.4}_{-9.2}\%$	$^{+7.4}_{-4.8}\%$

Appendix D

Misidentified leptons

D.1 Derivation of the misidentified lepton estimate for a four-lepton final state

The derivation of the misidentified lepton estimate for a four-lepton final state relies on induction. We derive the results for the one-lepton, two-lepton, and three-lepton final state and infer from the pattern the result for the four-lepton final state.

For each final state, the same procedure is applied. First, the number of events with the various possibilities of tight and loose-not-tight leptons are related to the numbers of real and fake leptons with a matrix. Afterwards the matrix is inverted and the number of fake leptons passing the tight selection is derived.

D.1.1 One-lepton final state

The one-lepton final state case has been presented in the estimation of the misidentified lepton background, see Section 5.2, and is in the following summarized for completeness. For better readability we use from now on N^{L} instead of N^{LnT}, and r and f for the real and fake efficiencies, respectively. The relation of the tight, N^{T}, and loose-not-tight leptons, N^{L}, to the real leptons, N^{r}, and fake leptons, N^{f}, is

$$\begin{pmatrix} N^{\mathrm{T}} \\ N^{\mathrm{L}} \end{pmatrix} = \begin{pmatrix} r & f \\ 1-r & 1-f \end{pmatrix} \begin{pmatrix} N^{r} \\ N^{f} \end{pmatrix}. \tag{D.1}$$

The number of fake leptons passing the tight selection, N^{fakes}, is given by

$$N^{\mathrm{fakes}} = f \cdot N^{f}. \tag{D.2}$$

With the inverted matrix we can express N^{fakes} in terms of the known quantities N^{T}, N^{L}, r, and f,

$$N^{\text{fakes}} = \left[1 - \frac{r(1-f)}{r-f}\right] N^{\text{T}} + \frac{rf}{r-f} N^{\text{L}}. \tag{D.3}$$

D.1.2 Two-lepton final state

The same steps can be applied to two-lepton final states. Since we have two leptons, we label the leading and sub-leading lepton with the indices $i = 1, 2$, respectively. We start by relating the loose-not-tight and tight leptons to the real and fake leptons,

$$\begin{pmatrix} N^{\text{TT}} \\ N^{\text{TL}} \\ N^{\text{LT}} \\ N^{\text{LL}} \end{pmatrix} = \begin{pmatrix} r_1 r_2 & r_1 f_2 & f_1 r_2 & f_1 f_2 \\ r_1(1-r_2) & r_1(1-f_2) & f_1(1-r_2) & f_1(1-f_2) \\ (1-r_1) r_2 & (1-r_1) f_2 & (1-f_1) r_2 & (1-f_1) f_2 \\ (1-r_1)(1-r_2) & (1-r_1)(1-f_2) & (1-f_1)(1-r_2) & (1-f_1)(1-f_2) \end{pmatrix} \begin{pmatrix} N^{rr} \\ N^{rf} \\ N^{fr} \\ N^{ff} \end{pmatrix}. \tag{D.4}$$

In the case of two leptons, the number of events with at least one fake lepton that passes the tight selection is

$$N^{\text{fakes}} = r_1 f_2 \cdot N^{rf} + f_1 r_2 \cdot N^{fr} + f_1 f_2 \cdot N^{ff}. \tag{D.5}$$

Now we need N^{rf}, N^{fr} and N^{ff} in terms of N^{TT}, N^{TL}, N^{LT} and N^{LL}. Thus, we invert the matrix in Equation (D.4):

$$\begin{pmatrix} N^{rr} \\ N^{rf} \\ N^{fr} \\ N^{ff} \end{pmatrix} = \begin{pmatrix} r_1 r_2 & r_1 f_2 & f_1 r_2 & f_1 f_2 \\ r_1(1-r_2) & r_1(1-f_2) & f_1(1-r_2) & f_1(1-f_2) \\ (1-r_1) r_2 & (1-r_1) f_2 & (1-f_1) r_2 & (1-f_1) f_2 \\ (1-r_1)(1-r_2) & (1-r_1)(1-f_2) & (1-f_1)(1-r_2) & (1-f_1)(1-f_2) \end{pmatrix}^{-1} \begin{pmatrix} N^{\text{TT}} \\ N^{\text{TL}} \\ N^{\text{LT}} \\ N^{\text{LL}} \end{pmatrix}. \tag{D.6}$$

With the inverse of the 4x4 matrix, we get

$$\begin{pmatrix} N^{rr} \\ N^{rf} \\ N^{fr} \\ N^{ff} \end{pmatrix} = \frac{1}{(r_1-f_1)(r_2-f_2)} \begin{pmatrix} (1-f_1)(1-f_2) & -(1-f_1) f_2 & -f_1(1-f_2) & f_1 f_2 \\ -(1-f_1)(1-r_2) & (1-f_1) r_2 & f_1(1-r_2) & -f_1 r_2 \\ -(1-r_1)(1-f_2) & (1-r_1) f_2 & r_1(1-f_2) & -r_1 f_2 \\ (1-r_1)(1-r_2) & -(1-r_1) r_2 & -r_1(1-r_2) & r_1 r_2 \end{pmatrix} \begin{pmatrix} N^{\text{TT}} \\ N^{\text{TL}} \\ N^{\text{LT}} \\ N^{\text{LL}} \end{pmatrix}. \tag{D.7}$$

Consequently, we have

$$
\begin{aligned}
N^{rr} &= \frac{1}{(r_1 - f_1)(r_2 - f_2)} \left[(1-f_1)(1-f_2)N^{\mathrm{TT}} - (1-f_1)f_2 N^{\mathrm{TL}} - f_1(1-f_2)N^{\mathrm{LT}} + f_1 f_2 N^{\mathrm{LL}}\right] \\
N^{rf} &= \frac{1}{(r_1 - f_1)(r_2 - f_2)} \left[-(1-f_1)(1-r_2)N^{\mathrm{TT}} + (1-f_1)r_2 N^{\mathrm{TL}} + f_1(1-r_2)N^{\mathrm{LT}} - f_1 r_2 N^{\mathrm{LL}}\right] \\
N^{fr} &= \frac{1}{(r_1 - f_1)(r_2 - f_2)} \left[-(1-r_1)(1-f_2)N^{\mathrm{TT}} + (1-r_1)f_2 N^{\mathrm{TL}} + r_1(1-f_2)N^{\mathrm{LT}} - r_1 f_2 N^{\mathrm{LL}}\right] \\
N^{ff} &= \frac{1}{(r_1 - f_1)(r_2 - f_2)} \left[(1-r_1)(1-r_2)N^{\mathrm{TT}} - (1-r_1)r_2 N^{\mathrm{TL}} - r_1(1-r_2)N^{\mathrm{LT}} + r_1 r_2 N^{\mathrm{LL}}\right].
\end{aligned}
\tag{D.8}
$$

With the number of events with real and fake leptons expressed in terms of the number of events passing the tight and loose-not-tight selection, we can calculate the number of fake leptons for the two-lepton final state given in Equation (D.5):

$$
\begin{aligned}
N^{\text{fakes}} &= r_1 f_2 \cdot N^{rf} + f_1 r_2 \cdot N^{fr} + f_1 f_2 \cdot N^{ff} \\
&= \frac{r_1 f_2}{(r_1 - f_1)(r_2 - f_2)} \left[-(1-f_1)(1-r_2)N^{\mathrm{TT}} + (1-f_1)r_2 N^{\mathrm{TL}} + f_1(1-r_2)N^{\mathrm{LT}} - f_1 r_2 N^{\mathrm{LL}}\right] \\
&+ \frac{f_1 r_2}{(r_1 - f_1)(r_2 - f_2)} \left[-(1-r_1)(1-f_2)N^{\mathrm{TT}} + (1-r_1)f_2 N^{\mathrm{TL}} + r_1(1-f_2)N^{\mathrm{LT}} - r_1 f_2 N^{\mathrm{LL}}\right] \\
&+ \frac{f_1 f_2}{(r_1 - f_1)(r_2 - f_2)} \left[(1-r_1)(1-r_2)N^{\mathrm{TT}} - (1-r_1)r_2 N^{\mathrm{TL}} - r_1(1-r_2)N^{\mathrm{LT}} + r_1 r_2 N^{\mathrm{LL}}\right].
\end{aligned}
\tag{D.9}
$$

This results in

$$
\begin{aligned}
N_{\text{fakes}} = &\left[1 - \frac{r_1(1-f_1)}{(r_1 - f_1)}\frac{r_2(1-f_2)}{(r_2 - f_2)}\right] N_{\mathrm{TT}} + \frac{r_1(1-f_1)}{(r_1 - f_1)}\frac{r_2 f_2}{(r_2 - f_2)} N_{\mathrm{TF}} \\
&+ \frac{r_1 f_1}{(r_1 - f_1)}\frac{r_2(1-f_2)}{(r_2 - f_2)} N_{\mathrm{FT}} - \frac{r_1 f_1}{(r_1 - f_1)}\frac{r_2 f_2}{(r_2 - f_2)} N_{\mathrm{FF}}.
\end{aligned}
\tag{D.10}
$$

As mentioned in Section 5.2, the efficiencies are dependent on the transverse momentum but not on the specific lepton. Since it is irrelevant which of the two leptons is fake, we can combine N_{TF} and N_{FT}. For consistency, we define the sum of N_{TF} and N_{FT} as N_{CR1}, N_{FF} as N_{CR2}, and N_{TT} as N_{SR}. Thus, we can rewrite Equation (D.10),

$$
\begin{aligned}
N_{\text{fakes}} = &\left[1 - \prod_{i=1}^{2} \frac{r_i(1-f_i)}{(r_i - f_i)}\right] N_{\mathrm{SR}} + \frac{r_i(1-f_i)}{(r_i - f_i)}\frac{r_j f_j}{(r_j - f_j)} N_{\mathrm{CR1}} \\
&- \left(\prod_{j=1}^{2} \frac{r_j f_j}{(r_j - f_j)}\right) N_{\mathrm{CR2}},
\end{aligned}
\tag{D.11}
$$

where the index i always refers to the tight lepton and the index j always refers to the loose-not-tight lepton.

D.1.3 Three-lepton final state

Similar to before, we define the matrix relation for the three-lepton final state,

$$\begin{pmatrix} N^{\text{TTT}} \\ N^{\text{TTL}} \\ N^{\text{TLT}} \\ N^{\text{LTT}} \\ N^{\text{TLL}} \\ N^{\text{LTL}} \\ N^{\text{LLT}} \\ N^{\text{LLL}} \end{pmatrix} = \begin{pmatrix} r_1 r_2 r_3 & r_1 r_2 f_3 & r_1 f_2 r_3 & f_1 r_2 r_3 \\ r_1 r_2 (1-r_3) & r_1 r_2 (1-f_3) & r_1 f_2 (1-r_3) & f_1 r_2 (1-r_3) \\ r_1 (1-r_2) r_3 & r_1 (1-r_2) f_3 & r_1 (1-f_2) r_3 & f_1 (1-r_2) r_3 \\ (1-r_1) r_2 r_3 & (1-r_1) r_2 f_3 & (1-r_1) f_2 r_3 & (1-f_1) r_2 r_3 \\ r_1 (1-r_2)(1-r_3) & r_1 (1-r_2)(1-f_3) & r_1 (1-f_2)(1-r_3) & f_1 (1-r_2)(1-r_3) \\ (1-r_1) r_2 (1-r_3) & (1-r_1) r_2 (1-f_3) & (1-r_1) f_2 (1-r_3) & (1-f_1) r_2 (1-r_3) \\ (1-r_1)(1-r_2) r_3 & (1-r_1)(1-r_2) f_3 & (1-r_1)(1-f_2) r_3 & (1-f_1)(1-r_2) r_3 \\ (1-r_1)(1-r_2)(1-r_3) & (1-r_1)(1-r_2)(1-f_3) & (1-r_1)(1-f_2)(1-r_3) & (1-f_1)(1-r_2)(1-r_3) \end{pmatrix}$$

$$\begin{pmatrix} r_1 f_2 f_3 & f_1 r_2 f_3 & f_1 f_2 r_3 & f_1 f_2 f_3 \\ r_1 f_2 (1-f_3) & f_1 r_2 (1-f_3) & f_1 f_2 (1-r_3) & f_1 f_2 (1-f_3) \\ r_1 (1-f_2) f_3 & f_1 (1-r_2) f_3 & f_1 (1-f_2) r_3 & f_1 (1-f_2) f_3 \\ (1-r_1) f_2 f_3 & (1-f_1) r_2 f_3 & (1-f_1) f_2 r_3 & (1-f_1) f_2 f_3 \\ r_1 (1-f_2)(1-f_3) & f_1 (1-r_2)(1-f_3) & f_1 (1-f_2)(1-r_3) & f_1 (1-f_2)(1-f_3) \\ (1-r_1) f_2 (1-f_3) & (1-f_1) r_2 (1-f_3) & (1-f_1) f_2 (1-r_3) & (1-f_1) f_2 (1-f_3) \\ (1-r_1)(1-f_2) f_3 & (1-f_1)(1-r_2) f_3 & (1-f_1)(1-f_2) r_3 & (1-f_1)(1-f_2) f_3 \\ (1-r_1)(1-f_2)(1-f_3) & (1-f_1)(1-r_2)(1-f_3) & (1-f_1)(1-f_2)(1-r_3) & (1-f_1)(1-f_2)(1-f_3) \end{pmatrix} \begin{pmatrix} N^{rrr} \\ N^{rrf} \\ N^{rfr} \\ N^{frr} \\ N^{rff} \\ N^{frf} \\ N^{ffr} \\ N^{fff} \end{pmatrix} \tag{D.12}$$

In the case of three leptons, the number of events with at least one fake lepton is given by

$$\begin{aligned} N^{\text{fakes}} =& r_1 r_2 f_3 \cdot N^{rrf} + r_1 f_2 r_3 \cdot N^{rfr} + f_1 r_2 r_3 \cdot N^{frr} \\ &+ r_1 f_2 f_3 \cdot N^{rff} + f_1 r_2 f_3 \cdot N^{frf} + f_1 f_2 r_3 \cdot N^{ffr} + f_1 f_2 f_3 \cdot N^{fff}. \end{aligned} \tag{D.13}$$

Now we need N^{rrf}, N^{rfr}, N^{frr}, N^{rff}, N^{frf}, N^{ffr} and N^{fff} in terms of N^{TTT}, N^{TTL}, N^{TLT}, N^{LTT}, N^{TLL}, N^{LTL}, N^{LLT} and N^{LLL}. Following the same approach as before, we get

$$
\begin{aligned}
N^{rrr} = & \frac{1}{(f_1 - r_1)(f_2 - r_2)(f_3 - r_3)} \\
& \big[(-1 + f_1 + f_2 + f_3 - f_2 f_3 - f_1 f_3 - f_1 f_2 + f_1 f_2 f_3) N^{\mathrm{TTT}} \\
& + (f_3 - f_2 f_3 - f_1 f_3 + f_1 f_2 f_3) N^{\mathrm{TTF}} \\
& + (f_2 - f_2 f_3 - f_1 f_2 + f_1 f_2 f_3) N^{\mathrm{TFT}} \\
& + (f_1 - f_1 f_2 - f_1 f_3 + f_1 f_2 f_3) N^{\mathrm{FTT}} + (-f_2 f_3 + f_1 f_2 f_3) N^{\mathrm{TFF}} \\
& + (-f_1 f_3 + f_1 f_2 f_3) N^{\mathrm{FTF}} + (-f_1 f_2 + f_1 f_2 f_3) N^{\mathrm{FFT}} + (f_1 f_2 f_3) N^{\mathrm{FFF}}\big]
\end{aligned}
$$

$$
\begin{aligned}
N^{rrf} = & \frac{1}{(f_1 - r_1)(f_2 - r_2)(f_3 - r_3)} \\
& \big[(1 - f_1 - f_2 - r_3 + f_2 r_3 + f_1 r_3 + f_1 f_2 - f_1 f_2 r_3) N^{\mathrm{TTT}} \\
& + (-r_3 + f_2 r_3 + f_1 r_3 - f_1 f_2 r_3) N^{\mathrm{TTF}} \\
& + (-f_2 + f_2 r_3 + f_1 f_2 - f_1 f_2 r_3) N^{\mathrm{TFT}} \\
& + (-f_1 + f_1 r_3 + f_1 f_2 - f_1 f_2 r_3) N^{\mathrm{FTT}} + (f_2 r_3 - f_1 f_2 r_3) N^{\mathrm{TFF}} \\
& + (f_1 r_3 - f_1 f_2 r_3) N^{\mathrm{FTF}} + (f_1 f_2 - f_1 f_2 r_3) N^{\mathrm{FFT}} + (f_1 f_2 r_3) N^{\mathrm{FFF}}\big]
\end{aligned}
$$

$$
\begin{aligned}
N^{rfr} = & \frac{1}{(f_1 - r_1)(f_2 - r_2)(f_3 - r_3)} \\
& \big[(1 - f_1 - r_2 - f_3 + f_3 r_2 + f_1 r_2 + f_1 f_3 - f_1 f_3 r_2) N^{\mathrm{TTT}} \\
& + (-f_3 + r_2 f_3 + f_1 f_3 - f_1 f_3 r_2) N^{\mathrm{TTF}} \\
& + (-r_2 + r_2 f_3 + f_1 r_2 - f_1 f_3 r_2) N^{\mathrm{TFT}} \\
& + (-f_1 + f_1 r_2 + f_1 f_3 - f_1 f_3 r_2) N^{\mathrm{FTT}} + (r_2 f_3 - f_1 r_2 f_3) N^{\mathrm{TFF}} \\
& + (f_1 f_3 - f_1 r_2 f_3) N^{\mathrm{FTF}} - (f_1 r_2 + f_1 r_2 f_3) N^{\mathrm{FFT}} - (f_1 r_2 f_3) N^{\mathrm{FFF}}\big]
\end{aligned}
$$

$$
\begin{aligned}
N^{frr} = & \frac{1}{(f_1 - r_1)(f_2 - r_2)(f_3 - r_3)} \\
& \big[(1 - r_1 - f_2 - f_3 + r_1 f_3 + r_1 f_2 + f_2 f_3 - r_1 f_2 f_3) N^{\mathrm{TTT}} \\
& + (-f_3 + r_1 f_3 + f_2 f_3 - r_1 f_2 f_3) N^{\mathrm{TTF}} \\
& + (-f_2 + r_1 f_2 + f_2 f_3 - r_1 f_2 f_3) N^{\mathrm{TFT}} \\
& + (-r_1 + r_1 f_3 + r_1 f_2 - r_1 f_2 f_3) N^{\mathrm{FTT}} + (f_2 f_3 - r_1 f_2 f_3) N^{\mathrm{TFF}} \\
& + (r_1 f_3 - r_1 f_2 f_3) N^{\mathrm{FTF}} + (r_1 f_2 - r_1 f_2 f_3) N^{\mathrm{FFT}} - (r_1 f_2 f_3) N^{\mathrm{FFF}}\big]
\end{aligned}
$$

$$
\begin{aligned}
N^{rff} =& \frac{1}{(f_1 - r_1)(f_2 - r_2)(f_3 - r_3)} \\
& \big[(-1 + f_1 + r_2 + r_3 - r_2 r_3 - f_1 r_2 - f_1 r_3 + f_1 r_2 r_3) N^{\mathrm{TTT}} \\
& + (r_3 - r_2 r_3 - f_1 r_3 + f_1 r_2 r_3) N^{\mathrm{TTF}} \\
& + (r_2 - r_2 r_3 - f_1 r_2 + f_1 r_2 r_3) N^{\mathrm{TFT}} \\
& + (-f_1 - f_1 r_3 - f_1 r_2 + f_1 r_2 r_3) N^{\mathrm{FTT}} + (-r_2 r_3 + f_1 r_2 r_3) N^{\mathrm{TFF}} \\
& + (-f_1 r_3 + f_1 r_2 r_3) N^{\mathrm{FTF}} + (-f_1 r_2 + f_1 r_2 r_3) N^{\mathrm{FFT}} + (f_1 r_2 r_3) N^{\mathrm{FFF}} \big] \\
N^{frf} =& \frac{1}{(f_1 - r_1)(f_2 - r_2)(f_3 - r_3)} \\
& \big[(-1 + r_1 + f_2 + r_3 - r_1 r_3 - r_1 f_2 - f_2 r_3 + r_1 f_2 r_3) N^{\mathrm{TTT}} \\
& + (r_3 - r_1 r_3 - f_2 r_3 + r_1 f_2 r_3) N^{\mathrm{TTF}} \\
& + (f_2 - r_1 f_2 - f_2 r_3 + r_1 f_2 r_3) N^{\mathrm{TFT}} \\
& + (r_1 - r_1 r_3 - r_1 f_2 + r_1 f_2 r_3) N^{\mathrm{FTT}} + (-f_2 r_3 + r_1 f_2 r_3) N^{\mathrm{TFF}} \\
& + (-r_1 r_3 + r_1 f_2 r_3) N^{\mathrm{FTF}} + (-r_1 f_2 + r_1 f_2 r_3) N^{\mathrm{FFT}} + (r_1 f_2 r_3) N^{\mathrm{FFF}} \big] \\
N^{ffr} =& \frac{1}{(f_1 - r_1)(f_2 - r_2)(f_3 - r_3)} \\
& \big[(-1 + r_1 + r_2 + f_3 - r_1 r_2 - r_1 f_3 - r_2 f_3 + r_1 r_2 f_3) N^{\mathrm{TTT}} \\
& + (f_3 - r_1 f_3 - r_2 f_3 + r_1 r_2 f_3) N^{\mathrm{TTF}} \\
& + (r_2 - r_1 r_2 - r_2 f_3 + r_1 r_2 f_3) N^{\mathrm{TFT}} \\
& + (r_1 - r_1 r_2 - r_1 f_3 + r_1 r_2 f_3) N^{\mathrm{FTT}} + (-r_2 f_3 + r_1 r_2 f_3) N^{\mathrm{TFF}} \\
& + (-r_1 f_3 + r_1 r_2 f_3) N^{\mathrm{FTF}} + (-r_1 r_2 + r_1 r_2 f_3) N^{\mathrm{FFT}} + (r_1 r_2 f_3) N^{\mathrm{FFF}} \big] \\
N^{fff} =& \frac{1}{(f_1 - r_1)(f_2 - r_2)(f_3 - r_3)} \\
& \big[(1 - r_1 - r_2 - r_3 + r_1 r_2 + r_1 r_3 + r_2 r_3 - r_1 r_2 r_3) N^{\mathrm{TTT}} \\
& + (-r_3 + r_1 r_3 + r_2 r_3 - r_1 r_2 r_3) N^{\mathrm{TTF}} \\
& + (-r_2 + r_1 r_2 + r_2 r_3 - r_1 r_2 r_3) N^{\mathrm{TFT}} \\
& + (-r_1 + r_1 r_2 + r_1 r_3 - r_1 r_2 r_3) N^{\mathrm{FTT}} + (r_2 r_3 - r_1 r_2 r_3) N^{\mathrm{TFF}} \\
& + (r_1 r_3 - r_1 r_2 r_3) N^{\mathrm{FTF}} + (r_1 r_2 - r_1 r_2 r_3) N^{\mathrm{FFT}} - (r_1 r_2 r_3) N^{\mathrm{FFF}} \big] .
\end{aligned}
\tag{D.14}
$$

Now, we can calculate the number of events with at least one fake lepton for the three-lepton case by combining Equation (D.13) and Equation (D.14).

After some simplifications we get

$$
\begin{aligned}
N^{\text{fakes}} = & \frac{1}{(r_1 - f_1)(r_2 - f_2)(r_3 - f_3)} \\
& [((r_1 - f_1)(r_2 - f_2)(r_3 - f_3) \\
& \quad - r_1(1 - f_1)r_2(1 - f_2)r_3(1 - f_3))\, N^{\text{TTT}} \\
& + (r_1(1 - f_1)r_2(1 - f_2)r_3 f_3) N^{\text{TTF}} \\
& + (r_1(1 - f_1)r_2 f_2 r_3(1 - f_3)) N^{\text{TFT}} \\
& + (r_1 f_1 r_2(1 - f_2)r_3(1 - f_3)) N^{\text{FTT}} \\
& - (r_1(1 - f_1)r_2 f_2 r_3 f_3) N^{\text{TFF}} - (r_1 f_1 r_2(1 - f_2)r_3 f_3) N^{\text{FTF}} \\
& - (r_1 f_1 r_2 f_2 r_3(1 - f_3)) N^{\text{FFT}} + (r_1 f_1 r_2 f_2 r_3 f_3) N^{\text{FFF}}] \,.
\end{aligned}
\tag{D.15}
$$

We can combine the events with two tight and one loose-not-tight lepton into N_{CR_1}, as well as the events with one tight and two loose-not-tight leptons into N_{CR_2}. The events with three loose-not-tight leptons are N_{CR_3} and with three tight leptons are N_{SR}. Rewriting Equation (D.15), we get

$$
\begin{aligned}
N_{\text{fakes}} = & \left[1 - \prod_{i=1}^{3} \frac{r_i(1 - f_i)}{(r_i - f_i)}\right] N_{\text{SR}} \\
& + \left(\prod_{i=1}^{2} \frac{r_i(1 - f_i)}{(r_i - f_i)}\right) \frac{r_j f_j}{(r_j - f_j)} N_{\text{CR}_1} \\
& - \left(\prod_{i=1}^{1} \frac{r_i(1 - f_i)}{(r_i - f_i)}\right) \left(\prod_{j=1}^{2} \frac{r_j f_j}{(r_j - f_j)}\right) N_{\text{CR}_2} \\
& + \left(\prod_{j=1}^{3} \frac{r_j f_j}{(r_j - f_j)}\right) N_{\text{CR}_3}.
\end{aligned}
\tag{D.16}
$$

D.1.4 Four-lepton final state

We can see a pattern on how each additional lepton contributes. Thus, we can extrapolate to the four-lepton case without the need to invert a 16x16

matrix. Thus, for the four-lepton case the following equation holds:

$$
\begin{aligned}
N_{\text{fakes}} = & \left[1 - \left(\prod_{i=1}^{4} \frac{r_i(1-f_i)}{(r_i - f_i)}\right)\right] N_{\text{SR}} + \left(\prod_{i=1}^{3} \frac{r_i(1-f_i)}{(r_i - f_i)}\right) \frac{r_j f_j}{(r_j - f_j)} N_{\text{CR1}} \\
& - \left(\prod_{i=1}^{2} \frac{r_i(1-f_i)}{(r_i - f_i)}\right) \left(\prod_{j=1}^{2} \frac{r_j f_j}{(r_j - f_j)}\right) N_{\text{CR2}} \\
& + \frac{r_i(1-f_i)}{(r_i - f_i)} \left(\prod_{j=1}^{3} \frac{r_j f_j}{(r_j - f_j)}\right) N_{\text{CR3}} - \left(\prod_{j=1}^{4} \frac{r_j f_j}{(r_j - f_j)}\right) N_{\text{CR4}}.
\end{aligned}
\tag{D.17}
$$

Overview and declaration of AI use

I utilized AI tools provided by the University of Heidelberg (YoKI) for the writing of this thesis. The tools used and the purpose of use is as follows:

- Llama: Proofreading (spelling, grammar, and punctuation) of Chapters 3 to 5
- GPT-OSS:
  - Proofreading (spelling, grammar, and punctuation) most of the thesis
  - Creation of an outline for the abstract, introduction, and conclusion
  - Feedback on the abstract, introduction, and conclusion
  - Translation of English abstract into German

I hereby declare that I take full responsibility for the quality and content of this thesis and I confirm that the thesis was written in compliance with the principles of good academic practice.

Heidelberg, Germany, March 2, 2026

Anke Ackermann

Acknowledgments

I would like to thank everyone who has guided me and been part of this journey for the last three-and-a-half years.

I am especially grateful to Hans-Christian Schultz-Coulon for welcoming me into the ATLAS group, for his confidence in my abilities, for his expert guidance, and for always having an open door.

My primary supervisor, Rainer Stamen, was constantly available, trusted me, and helped me focus on what mattered most. I am very thankful for his excellent guidance and for the invaluable feedback he has provided over the years and on my entire thesis.

I would like to thank Ulrich Uwer for kindly acting as my second examiner and for taking the time and effort to read my thesis.

Many colleagues have contributed to my scientific development: Monica Dunford, Pavel Starovoitov, and Martin Wessels have patiently answered all my questions and helped me develop. A special thanks to Monica for pep talks when they were needed most and for reviewing parts of this work.

To Petra, the heart of the ATLAS group, thank you for always being available and ensuring every Dienstreiseantrag is submitted on time.

I am incredibly happy to be part of the F8 and F11 groups. Over the years, many colleagues became friends, making daily work enjoyable. Thank you for the fun group activities—from movie nights and board-game evenings to Radler Fridays and Weißwurstfrühstück. I would especially like to thank Isa, Mathias, Thomas, Falk, Maximilian, and Tobias for reading parts of the thesis and providing valuable feedback.

My family and friends kept me grounded and ensured I had a life beyond physics; I am very thankful for their constant encouragement.

Finally, my deepest gratitude goes to Elias—my rock and constant source of love and encouragement. He supported me every step of the way, and I could not have done this without him.